The Dissertation Committee for Luciana Meli Certifies that this is the approved version of the following dissertation:

MICROSTRUCTURE DESIGN AND FORMATION OF ORGANIC/INORGANIC THIN FILM NANOCOMPOSITES

Committee:

Keith P. Johnston, Supervisor

Peter F. Green, Co-Supervisor

Roger T. Bonnecaze

Venkat Ganesan

Arumugam Manthiram

MICROSTRUCTURE DESIGN AND FORMATION OF ORGANIC/INORGANIC THIN FILM NANOCOMPOSITES

by

Luciana Meli, B.S.

Dissertation

Presented to the Faculty of the Graduate School of
The University of Texas at Austin
in Partial Fulfillment
of the Requirements
for the Degree of

Doctor of Philosophy

The University of Texas at Austin
May, 2007

Dedication

This thesis is dedicated to my parents, Guillermina and Roberto, and my husband Abraham.

Acknowledgements

This thesis is the result of five and a half years of work, in the course of which I have been fortunate to be surrounded by people who have motivated and helped me in numerous ways. It is a pleasure to finally get an opportunity to express my gratitude to some of them.

First and foremost I would like to thank my advisor, Professor Peter F. Green, for his support, his patience, and his guidance. I am grateful to have worked with such a knowledgeable and dedicated individual, whose commitment to excellence will leave a long-lasting impression upon me.

I would also like to thank my co-advisor, Prof. Keith P. Johnston, for sharing with me his scientific insight and his endless enthusiasm. I greatly appreciate his encouragement and his willingness to help me.

Many past and present members of Prof. Green's research group contributed substantially to the development of this work. In particular, I am indebted to Joseph Q. Pham, Brian M. Besancon, Yuan Li, Jamie M. Kropka and of course, Abraham Arceo, for the many discussions and for their words of advice in moments of uncertainty. In the same way, credit goes to Alejandra Camacho Bragado and Domingo García Gutiérrez, for their advice and their technical help with the capricious TEM. I would further like to thank Prof. Roger T. Bonnecaze, Prof. Venkat Ganesan, and Prof. Arumugam Manthiram, for graciously serving as members of my dissertation committee.

On a personal note, I would like to express my profound gratitude to my parents, Guillermina and Roberto, and my brother and sister, Fabrizio and Daniela, for their love and unconditional support. It is through my parents' example that my accomplishments have gained shape and meaning.

It is difficult to convey how much love, help, scientific knowledge, and fortitude I have received during these challenging years from my husband, Abraham. I feel fortunate to be able to share so many aspects of my life with such a wonderful person.

Finally, I would like to thank all my friends, both in Austin and in Ann Arbor, who have made this experience far more enjoyable and fulfilling by 'forcing' me to step out of the lab, at least for a while.

MICROSTRUCTURE DESIGN AND FORMATION OF ORGANIC/INORGANIC THIN FILM NANOCOMPOSITES

Publication No._____________

Luciana Meli, PhD
The University of Texas at Austin, 2007

Supervisors: Keith P. Johnston and Peter F. Green

There is significant interest in understanding and exploiting the extraordinary property enhancements of polymers, enabled by adding small concentrations of nanoparticles to polymer hosts to create polymer nanocomposites (PNCs). Thin film PNCs hold potential for novel technological applications in areas such as optoelectronics or photovoltaic devices. One of the key challenges that limits the potential of PNC-based technologies is the control of nanofiller dispersion throughout the matrix. This requires a fundamental understanding of the energetic interactions that affect dispersion. Thin film PNCs pose a greater challenge than bulk PNCs, largely because interfacial interactions become increasingly important as the material is confined.

It is equally important to find effective processing schemes that promote nanofiller dispersion in a manner that can be readily scalable for industrial operations. Accordingly, the last few years have seen an upsurge in processing schemes involving

supercritical solvents, due in part to their tunable solvent strength. To this end, our research is aimed at gaining control of nanoparticle dispersion within thin film hosts using supercritical CO_2 ($scCO_2$) as a processing aid. This research examined a series of related problems.

For the first project, we investigated the effects of $scCO_2$ sorption on the structural stability and kinetics of destabilization of homopolymer films. We showed that the films are metastable under these conditions, and the barrier to nucleation is larger than that encountered in air/vaccum.

We also examined the issue of nanofiller dispersion within homopolymer thin films. In a model athermal mixture, polystyrene-coated gold nanoparticles in polystyrene hosts, interfacial segregation was generally observed, and was shown to be a function of the wetting characteristics of the brush-matrix interface and the ratio of the size of the particles to the unperturbed dimensions of the host chains. In a separate system, we show how $scCO_2$ can serve to prevent coarsening, which is ubiquitous in air/vacuum environments at elevated temperatures, for these nanofillers.

Finally, we made nanocomposite micellar structures from block copolymers, with a fluorinated block. Gold nanoparticles were sequestered within the discontinuous domain. We then showed how $scCO_2$ could be used to invert the structure, placing the nanoparticles in the continuous phase.

Table of Contents

List of Tables

List of Figures

CHAPTER 1. Introduction

1.1 MOTIVATION AND RESEARCH OBJECTIVES.

Macroscopic composites formed by introducing fillers and additives into polymer matrices have been used in commercial polymeric products for decades now, as a means to bolster the performance of the products, as well as to reduce their overall cost. More recently, the fabrication of composite materials containing nanoscopic fillers, so-called polymer nanocomposites (PNCs), has become of particular interest since these materials exhibit significant property enhancements at much lower additive concentrations than conventional microscopic-sized filler composites. Some of the property changes observed in these nanocomposites are based solely on the unique, size-dependent properties of nanoscopic matter, e.g., on the luminescence of semiconductor nanoparticles. Other property changes can be the result of cooperative interactions between the nanoparticle and the polymeric chain[1, 2], impacting both static and dynamic properties of the system. The characteristic features that distinguish these nanocomposites from traditional filler composites, and that determine to a large extent their microstructure and properties, are[2]: large surface to volume ratio, low percolation thresholds, large particle-number densities, extremely small interparticle separations, and comparable length scales between the particle size and the average chain dimension, R_g.

As a better understanding of the basic principles that determine the performance of the nanocomposite materials emerges, a number of key challenges regarding the fabrication of polymer nanocomposites have been revealed. First, there is a necessity to find cost-effective methods to control nanoparticle *dispersion*, since *aggregation* and *coarsening* of these entities is commonplace, and precludes any advantage of using nanometer-sized particles as filler material. To overcome this obstacle, it is essential to gain insight into the *fundamental energetic interactions that control dispersion of nanoparticles* in polymer melt matrices. Equally important it is to find effective *processing techniques that foster and maintain dispersion* of the nanoscale inclusions, yet are still applicable to industrial processes.

In thin films, a related issue is the need to control *nanoparticle aggregation near interfaces*. This topic has important repercussions for the growing number of applications of polymer/nanoparticle composites in various thin film technologies, such as sensors[3], photovoltaic devices[4] or organic memory devices[5].

A final challenge is the development of *structure-property relationships* that can help us to tailor the properties of the nanocomposite, and which can be obtained from a basic *understanding of the collective intermolecular interactions and processes* that lead to the extraordinary behavior of these materials. In this endeavor the *precise control of microstructure* within the composite material is of paramount importance to isolate the parameters that enhance the performance of the nanocomposite.

In this context, our research was aimed at understanding microstructure formation and processing of polymer thin film nanocomposites, examining four major topics:

1. spatial organization of sterically stabilized nanoparticles embedded in homopolymer thin films*;*
2. the effects of processing on the coarsening of sterically stabilized nanoparticles in homopolymer thin films*;*
3. sequestration of nanoparticles in block copolymer domains*;*

4. use of compressed CO_2 for the low temperature processing of pure homopolymer thin films, and its influence on their structure and properties*;*

The remaining sections in this chapter are intended to provide a background for the work described in the body of the dissertation. *Each chapter in this thesis is dedicated to each of the foregoing topics.*

1.2 MORPHOLOGY OF HOMOPOLYMER/NANOPARTICLE MIXTURES

1.2.1 Hard-Sphere Fillers in a Homopolymer Melt

Various theoretical and computational approaches[6-12] have been employed to study fundamental aspects of dense hard-sphere particle/polymer mixtures including particle dispersion and spatial organization, phase separation, chain conformation and packing near the polymer-particle interface, and the effect of these contributions on the nanocomposite properties. Generally, it has been found that for entropically dominated athermal mixtures (polymer and particle are non-interacting) there exists a depletion attraction between spheres that leads to particle aggregation and phase separation[7]. This depletion attraction results from the fact that the monomer density profile near a wall or particle has an oscillatory dependence on distance from the particle[11]. For athermal mixtures, the density profile presents a depletion layer near the wall and approaches bulk density away from it (Figure 1.1b), giving rise to the entropic, monomer depletion-induced attraction between particles. Hence, the studies indicate that attractive interactions between polymer and particle are a prerequisite to achieve some degree of miscibility in these mixtures[6]. In this case, the monomer density decreases away from the particle, generating an effective repulsion between particles (Figure 1.1a).

Schweizer and coworkers[7] employed a microscopic theory, based on the polymer reference interaction site model (PRISM), to study phase behavior of nanocomposites with an adsorbing polymer melt (attractive polymer-particle interactions). The relevant system variables are the particle volume fraction, ϕ, the ratio of particle diameter to monomer diameter, D/d, the strength and range of the polymer-particle interactions, ε_{PC} and α, and particle-particle interactions, ε_{CC}. Two distinct phase behaviors, separated by a miscibility window, are predicted (Figure 1.1C). At low monomer-particle attraction strengths, there is contact aggregation and phase separation due to an *entropic* depletion-induced attraction, as in the case of athermal mixtures. As ε_{PC} increases ($\varepsilon_{PC} \approx 1k_BT$), a demixing curve is encountered, where the formation of a loosely bound layer of polymer around the filler leads to a sterically stabilized miscible fluid. In this case, the loss in conformational entropy of the chain incurred by adsorbing to the particle surface is offset by the gain in enthalpy created by the favorable particle-polymer contacts.

The second demixing curve appears at relatively high ε_{PC} where *enthalpic* effects dominate the free energy of mixing. The polymer chains strongly adsorb to the particles forming tightly bound layers with well-defined interparticle separations. Consequently a network phase where particles are locally bridged is realized. The authors suggest that the phase boundary at low ε_{PC} may be analogous to an entropy-driven lower critical solution temperature (LCST) typical of polymer-polymer blends, while the phase boundary at high ε_{PC} is analogous to an enthalpy driven upper critical solution temperature (UCST).

The miscibility window narrows with increasing particle size, D/d, having particular impact on the demixing curve at high ε_{PC}. This is attributed to enhanced polymer-bridging interactions associated with larger particle sizes. The miscibility window is also predicted to narrow with increasing polymer chain length, even though the effect is relatively weak in comparison to that of particle size. The decrease in miscibility follows from the loss of translational entropy of the chains as they get larger, offering less resistance toward particle bridging. Finally, if the nanoparticle-nanoparticle attraction strength ε_{CC} is increased, the region of miscibility narrows and can eventually disappear. However, the study does predict the existence of a miscibility window at small or moderate direct van der Waals interactions.

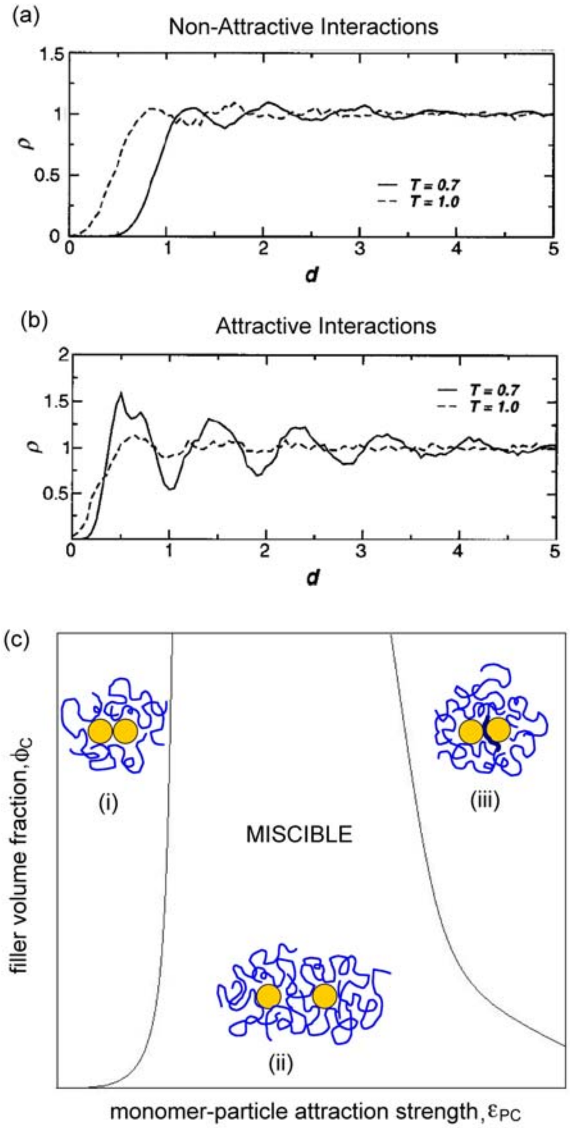

Figure 1.1: (a,b) Monomer density profile ρ(d) as a function of the distance from the nanoparticle surface for (a) an athermal mixture (b) a mixture where the interaction between particle and polymer are attractive. The monomer density profiles are taken from Starr11 et al. (c) Schematic diagram of the phase behavior of a hard-sphere filler/polymer mixture showing two distinct phase transitions separated by a miscibility window. The panel illustrates the type of organization expected in each region: (i) contact aggregation, (ii) steric stabilization and (iii) bridging.

1.2.2 Brush-Coated Fillers in a Homopolymer Melt

Filler dispersion in a homopolymer melt is considerably modified by the presence of ligands or polymer chains grafted to the particle surface. The brush layer can prevent particles from reaching interparticle distances where attractive van der Waals interactions are strong enough to cause aggregation. In this case, dispersion will depend heavily on the interface between the grafted layer and the bulk melt, a problem which has been the subject of scrutiny for nearly three decades now[13-19]. Specifically, interpenetration between grafted and matrix chains is a vital component of colloidal stability. Complete penetration of free chains into the brush forces the grafted chains to extend into the melt and results in a wet brush (Figure 1.2a). On the other hand, a dry brush is formed when only partial penetration of the matrix chains is achieved (Figure 1.2b). The large size of the free polymer chains limits their ability to penetrate the grafted chains because of their reduced entropy, making the likelihood of dry-brush formation high with respect to smaller molecules. A consequence of dry-brush formation in high molecular weight solvents is the existence of entropically driven attractive interactions between two brushes immersed in the melt, which can ultimately derive in particle aggregation[15].

The transition from a wet brush to a dry brush depends on the grafting density, σ, the length of grafted and free chains, N and P, and the interaction between grafted and free chains χ (where χ is the Flory-Huggins interaction parameter). In the absence of enthalpic interactions (that is, when the melt and grafted chains are chemically identical, $\chi=0$), detailed diagrams of state of a polymer brush immersed in a melt have been constructed. In figure 1.2c, one such diagram[13] obtained from scaling laws illustrates the conditions under which the attached chains undergo transitions to different brush behavior. In the case of incompatible polymers ($\chi<0$) mixing of grafted and free chains is discouraged leading to a collapse of the grafted layer. Leibler and coworkers[13] recently calculated diagrams for the case of compatible polymers ($\chi>0$); they indicate that favorable enthalpic interactions can change the structure of the brush from a dry brush to a wet brush and consequently favor particle dispersion.

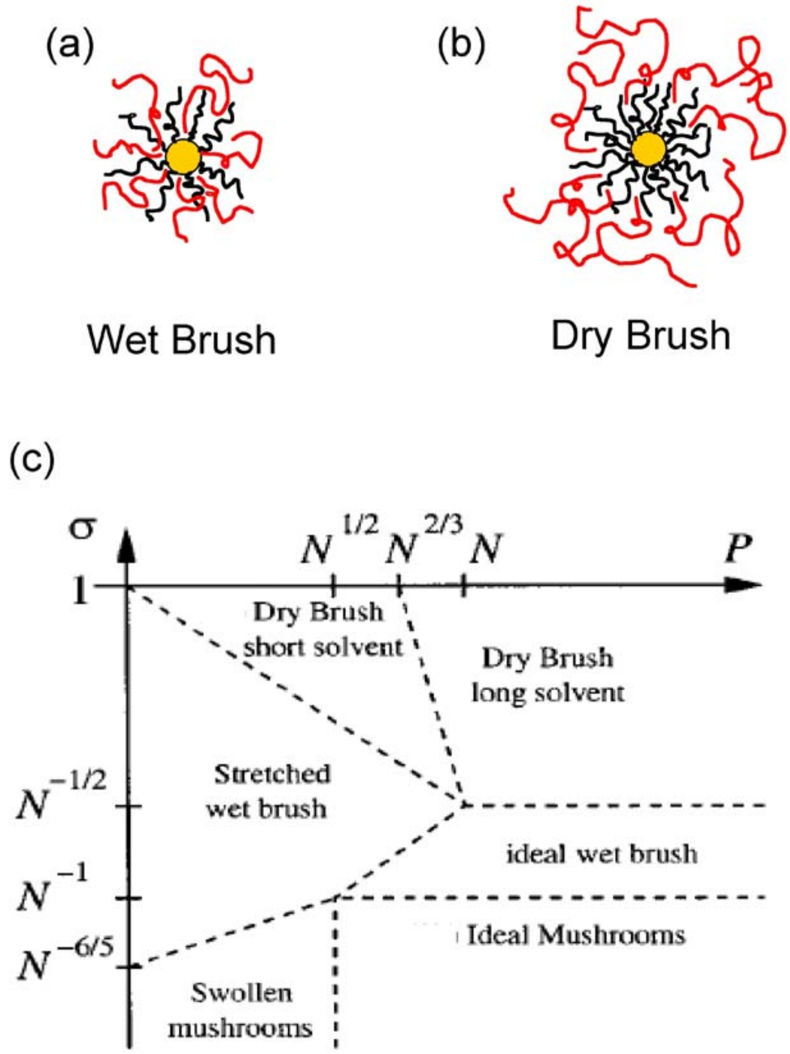

Figure 1.2: (a, b) Nanoparticle with end-tethered polymers of length N immersed in a homopolymer melt of chain length P. (a) Wet brush condition: there is complete penetration of the matrix chains into the brush when the grafted chains are sparsely packed on the surface and their size is comparable to that of the host chains (b) Dry brush condition: the polymer chains attached to the particle are short (compared to the homopolymer chains) and densely packed permitting only partial interpenetration by the host chains. (c) Diagram of states for grafted polymer in contact with a chemically identical polymer melt. This figure is originally taken from the work of Borukhov[13] et al. with slight modifications.

1.2.3 Homopolymer/Nanoparticle Mixtures Confined to a Thin Film Geometry

The presence of interfaces is an additional factor that can alter the spatial distribution of nanoparticles in a polymer melt. For thin films, the polymer-interface and particle-interface interactions, ε_{PI} and ε_{CI}, as well as the film thickness, h, are parameters that need to be accounted for to understand the structure of the nanocomposite.

Balazs and coworkers[20] performed computational studies of compatible hard-sphere filler/homopolymer mixtures near a surface containing a crack, where $\varepsilon_{PI}= \varepsilon_{CI}= 0$. They show that the particles tend to localize at the damaged wall with significant volume fractions found within the crack. Despite the compatibility between the particles and the polymer, they demonstrate that segregation of the particles to the interface is induced by an entropic depletion attraction between the particles and the surface. That is, the polymer chains expel the particles to the surface (and to the crack) to avoid the loss of conformational entropy incurred by having to stretch around the particles. The predictions of this study were experimentally demonstrated in a multilayer system comprised of PEO-covered CdSe nanoparicles dispersed in poly(methyl methacrylate) (PMMA) in contact with a brittle silicon oxide layer[21]. After crack formation was achieved by heating the bilayer above the glass transition (T_g), CdSe particles that were comparable in size to the radius of gyration (R_g) of the PMMA matrix migrated to the crack. Smaller particles remained uniformly dispersed within the matrix because the polymer could easily accommodate the particles without a significant entropic penalty.

It is important to note that preferential interactions between particles and an interface can further direct the migration of nanoparticles to a particular interface. For example, Barnes[22] et al. demonstrated that fullerene particles embedded in a poly(styrene) (PS) film tend to enrich the silicon substrate due to preferential interactions with this interface. Interestingly, such highly segregated nanocomposite structures were shown to effectively inhibit dewetting of the PS films.

In Chapter 3 of this dissertation, we perform a systematic study of the spatial distribution of brush-coated nanoparticles immersed in a chemically identical homopolymer thin film matrix. We show how the brush structure, the relative size of the particles, and interfacial energy between the brush and the polymer melt affect the depth distribution of nanoparticles within the film

1.3 MORPHOLOGY OF BLOCK COPOLYMER/NANOPARTICLE MIXTURES

1.3.1 Self-Assembly of Diblock Copolymers

Block copolymers (BCP) molecules are known to self-assemble into geometrical nanostructures below an order-disorder temperature, ODT. More explicitly, dissimilar blocks tend to phase separate into microphases, having the spatial extent of these domains constrained by the chemical connectivity of the blocks. Thus, upon phase separation, the system minimizes the sum of the interfacial energy associated with A-B contacts and the elastic free energy associated with normal stretching of the chains, forming self-organized periodic microstructures of incredible variety.

The phase behavior of an A-b-B diblock copolymer in the bulk is determined by the Flory-Huggins energetic interaction parameter, χ ($\sim T^{-1}$), the total number of segments, N, and volume fraction of A segments, f[23]. As compositional asymmetries go from low (f~0.5) to high values ($f \rightarrow 0$), microstructures go from lamellae, to bicontinuous structures, to hexagonally packed cylinders, and finally to body-centered cubic arrays of spheres (Figure 1.3). For every volume fraction, there is a specific χN value above which the diblock will phase separate into its designated morphology.

In thin films, the morphology and topography of the BCP in its ordered state will be influenced by additional variables such as film thickness and the interaction of the copolymer with both interfaces (substrate and free surface). Polymer molecules are far more sensitive to surface segregation effects than small molecules due to their low combinatorial entropy of mixing which facilitates their phase separation. In most situations, a block constituent is preferentially attracted to one (asymmetric wetting case), or both (symmetric wetting case) external interfaces, which can induce preferential alignment with the interfaces. For instance, lamellae-forming blocks usually align parallel to the interfaces (Figure 1.4a and 1.4b). However, perpendicular-aligned domains can be induced by chemically modifying the substrate to neutralize preferential interactions (Figure 1c).

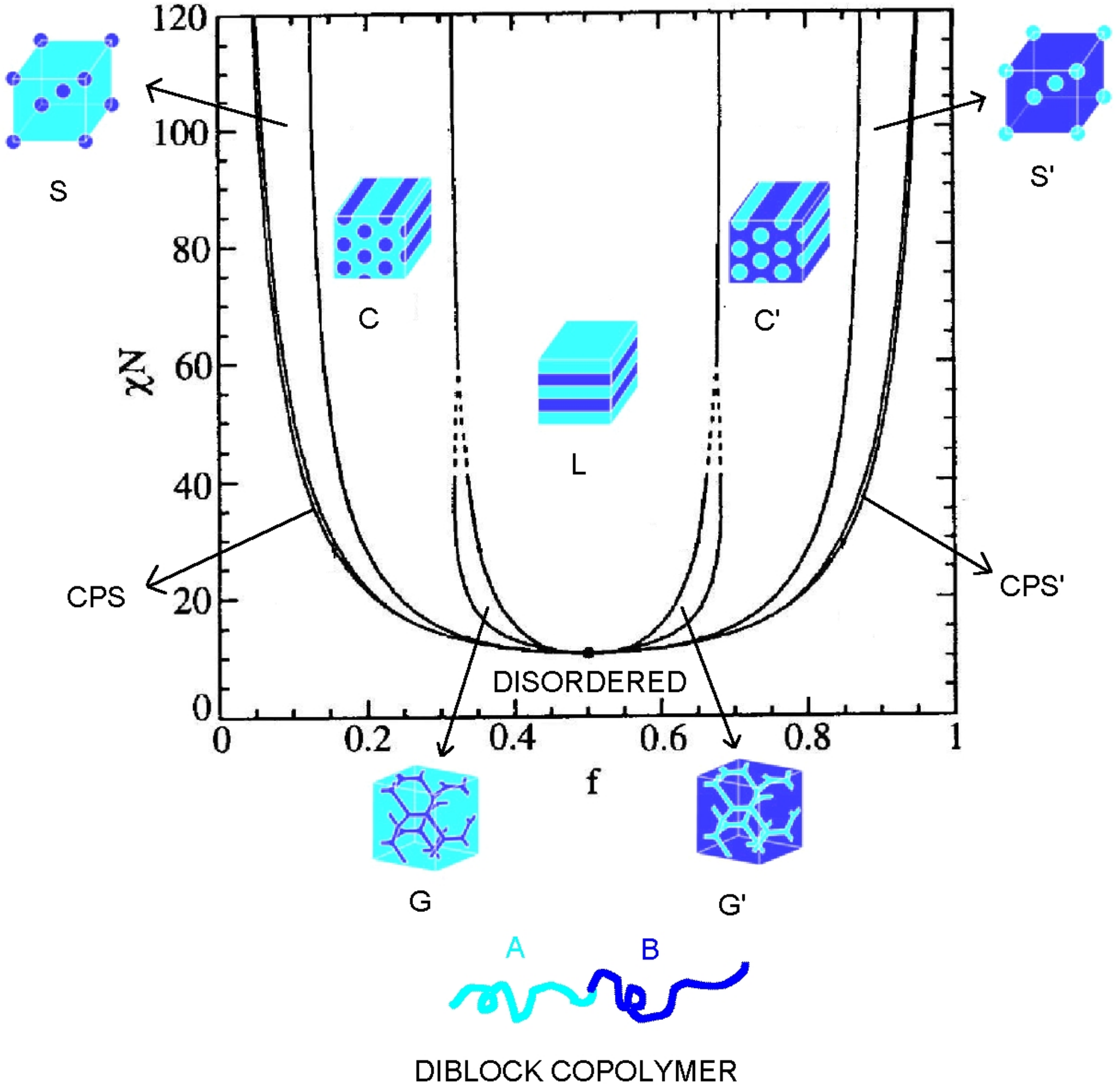

Figure 1.3: Mean-field phase diagram for a symmetric diblock copolymer, reproduced from reference 23. The diagram was modified to include illustrations of the different microstructures found: L, lamellar; G, gyroid; C, cylinder in a hexagonal array; S, spheres in a body center cubic array; and CPS; close-packed spheres.

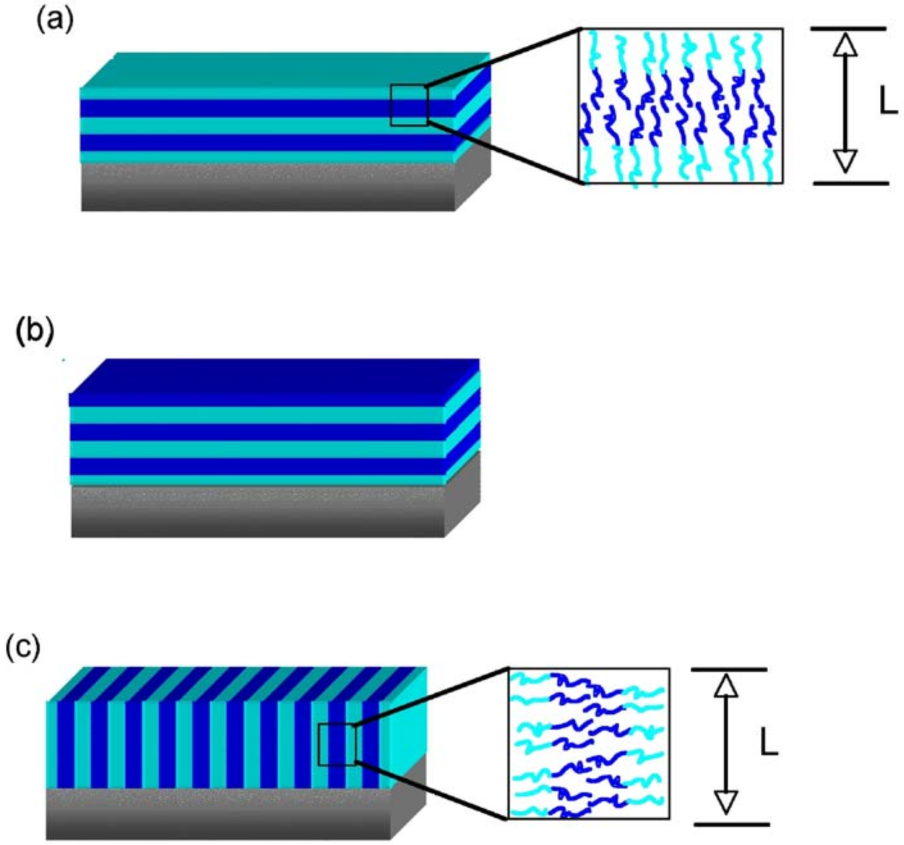

Figure 1.4: Structures of a phase segregated symmetric diblock copolymer thin film. (a, b) Schematics of lamellae oriented parallel to the substrate for the symmetric (a) and asymmetric (b) wetting case. (c) Perpendicularly-aligned lamellae arise when preferential interactions between the blocks and the interface are neutralized.

1.3.2. Structure of Bulk Block Copolymer/Nanoparticle Mixtures

In recent years, researchers have been seeking to harness the periodic domains obtained by microphase separation of a BCP to direct the spatial distribution of nanoparticles within the polymer matrix[2, 24-27]. The general strategy involves tailoring the surface chemistry of nanoparticles, such that the compatibility with one of the blocks of the copolymer drives the particles into the respective block domain. Compatibilization is usually achieved by grafting ligands or polymers to the particle surface. The ultimate goal is to arrange the nanoscopic objects by 'bottom-up' processes to create hierarchically ordered materials with tailored structures and properties that extend through multiple length scales.

Theoretical and computer simulation studies[28-30] have begun to elucidate the delicate interplay between enthalpic and entropic effects that lead to structure development in these systems. By using a combination of self-consistent field theory (SCF) for the A-b-B block copolymer and density functional theory (DFT) for the particles (which were assumed to be hard spheres with neutral interactions with the A block and repulsive interactions with the B block), Thompson[29] et al. found that larger nanoparticles ($R=0.3R_o$, where R is the radius of the nanoparticle and R_o the root-mean-square end-to-end distance of the diblock chain) located at the center of the A block domains, whereas smaller particles ($R=0.2R_o$) dispersed more uniformly throughout these domains (Figure 1.5a and 1.5b, respectively). The results were interpreted as a compromise between the gain in translational entropy obtained by free particle dispersion within the A domains, and the conformational entropy penalty associated with stretching of A block chains around the particles. Similar findings were obtained by using analytical scaling theory to investigate particle penetration in ultrathin films of end-tethered grafted polymer chains[31].

Monte Carlo simulations that examining the behavior of a single neutral nanoparticle showed that the particle locates preferentially at the A-B block interface[28] (Figure 1.5c). Shultz[32] et al. arrived at a similar conclusion, using discontinuous molecular dynamics simulations to study the phase behavior of diblock copolymer/nanoparticle composites. These results are consistent with the segregation of neutral good solvent molecules at the A-B interface, which can screen repulsive interactions between the blocks and consequently minimize the overall energy of the system.

Experimental and theoretical studies have also shown the possibility of inducing phase transitions upon addition of nanoparticles[29, 33]. The nanoparticles act to increase the effective volume fraction of the block chain, resulting in a phase transition of the equilibrium microdomain structure if the amount of particles exceeds a threshold value.

Finally, the effect of brush structure has been addressed in blending experiments of PS-functionalized fullerenes in a poly(styrene sulfonic acid)-b-poly(isoprene) matrix[34]. The authors show that with increasing length and grafting density of the PS ligand, the particles migrate to the center of the PS block domains, as opposed to the more homogenous distribution of particles found when shorter PS ligands are scarcely tethered to the fullerene surface. These experiments clearly demonstrate that the wetting behavior of the brush can significantly alter nanoparticle dispersion within BCP microodomains.

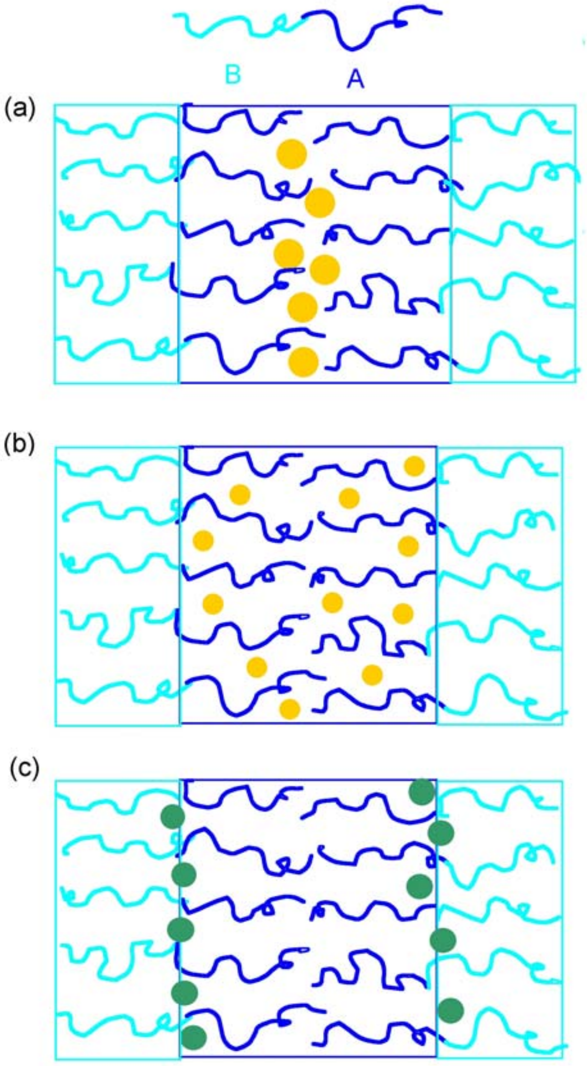

Figure 1.5: Schematic representation of the distribution of nanoparticles within a block copolymer for (a) large fillers ($R=0.3R_o$) with neutral nanoparticle-A block interactions and repulsive particle-B block interactions, small fillers ($R=0.2R_o$) with neutral nanoparticle-A block interactions and repulsive particle-B block interactions and, (c) filler with neutral interactions towards both blocks.

1.3.3 Structure of Confined Nanoparticle/Block Copolymer Mixtures

As in the case of thin film homopolymer nanocomposites discussed in section 1.2.3, interfacial interactions and chain stretching can play an important role in determining the equilibrium morphology of a BCP/nanoparticle composite.

Lee[35] et al. examined the structure of a symmetric A-b-B diblock copolymer confined between to A-like surfaces using the SCF/DFT model mentioned in the previous section. As expected, the lamellar microdomains orient parallel to the interfaces when only the pure BCP is considered. The mixing of non-selective nanoparticles with the BCP leads to segregation of the nanopaticles to the surfaces as a result of an entropic induced attraction between the particles and the walls. In addition, when the particle concentration at the interface is sufficiently high the microdomains switch orientation to form a surface-perpendicular lamellar structure. The reorientation of the lamellae is a consequence of the fact that the particles effectively modify the chemical nature of the interfaces, and thus the wetting characteristics of the polymer.

Chapter 5 of this dissertation examines the morphology of thin films of a diblock copolymer/nanoparticle mixture where the nanoparticles exhibit a stronger affinity for one of the blocks. The experiments reveal that nanoparticles are indeed sequestered within the preferred block domain, but in the proximity of the substrate, and not homogenously distributed across the film. The distribution of the nanoparticles is controlled by several competing factors: the van der Waals interaction between nanoparticles and interfaces, favorable ligand-block enthalpic interactions, and the conformational entropy of the host chains.

1.4 THIN FILM MORPHOLOGY UNDER SUPERCRITICAL CARBON DIOXIDE ENVIRONMENTS

1.4.1 Use of Supercritical Carbon Dioxide in the Processing of Polymer Matrices

Supercritical fluids have been studied extensively as alternatives to replace organic solvents and water in numerous industrial processes due, in part, to the possibility of changing the properties of the fluid with small adjustments in pressure and/or temperature. For example, the ability to change the solvent strength of the supercritical fluid using pressure offers many advantages in the control of reactions[36] and in separation processes[37]. Supercritical carbon dioxide is especially attractive because of its accessible critical conditions, its availability, its non-toxicity, and its good interfacial and transport properties. Moreover, while $scCO_2$ is a poor solvent for most hydrocarbon polymers, it can swell and plasticize the macromolecules causing depressions in their glass transition temperatures of several tens of degrees. This characteristic makes it a good processing aid for polymeric materials. For instance, plasticization can lead to viscosity reductions convenient for polymer extrusion, enhancement of monomer diffusion for polymer synthesis, foaming of polymers, and changes in polymer morphology[37]. The use of compressed CO_2 as a transient plasticizing agent can be particularly helpful in the processing of polymer nanocomposites, where it can allow diffusion of fillers at milder processing temperatures than normally required. Indeed, in Chapter 4 of this dissertation we demonstrate that $scCO_2$ can be used to anneal polymer nanocomposites, allowing polymer chain relaxation at low temperatures, while preventing coarsening of surface-protected nanoparticles.

1.4.2 Structure and Properties of Homopolymer Thin Films in CO_2

In recent years, the properties of homopolymer thin films in CO_2 have been subject to scrutiny, and are now reasonably well understood. Swelling and T_g (or glass transition pressure, P_g) measurements of polymeric thin films in supercritical fluids have been the focal point of several studies[36, 38-41]. Researchers have found that swelling and CO_2 sorption are higher in polymer thin films than in their bulk analogues[39, 41]. This phenomenon has been attributed to adsorption of excess CO_2 at both interfaces. Clearly the influence of the interfaces on the overall CO_2 content in the polymer becomes more significant as the film gets thinner, causing greater sorption of CO_2 with decreasing film thickness.

The presence of excess CO_2 also affects the pressure at which the glass transition occurs. Namely, the pressure required to plasticize the film and induce devitrification will decrease appreciably with decreasing film thickness due to the associated increase in the average amount of CO_2 in the film[36, 38].

On the other hand, in Chapter 2 we examine structural instabilities of PS thin films in liquid and supercritical CO_2 environments. The work on this area has yielded interesting information regarding the influence CO_2 sorption has on both the intermolecular interactions that may engender dewetting of the system, and on the kinetics of film dewetting.

1.4.3 Effects of CO_2 on the Phase Behavior of Block Copolymers

Before considering the effect that supercritical CO_2 has in the phase behavior of BCPs it is useful to first discuss the effect of liquid solvents on these systems. Liquid solvents have been shown to have two main effects in block copolymer phase transitions: the screening of unfavorable enthalpic interactions between dissimilar segments which leads to a depression in the ODT, and in some cases, preferential swelling of one phase that leads to a change in the effective composition of the block copolymer that ultimately may give rise to order-to-order transitions[42].

The case of compressible solvents involves additional complications and advantages. First, the solvent strength of the compressed fluid, which relates to solvent density, is highly dependent upon pressure and temperature. Also, hydrostatic pressure effects on phase behavior may be non-negligible when dealing with compressed solvents systems. Finally, the compressibility of a polymer/compressed fluid mixture may increase drastically in comparison to the undilated melt. This effect can cause differential dilation of the copolymer components that may exacerbate entropic penalties of mixing. Extensive studies by Watkins and coworkers[43-45] have shown that bulk BCP with upper order-disorder transitions show slight enhancement in miscibility due to a lowering of interfacial tensions and screening of unfavorable enthalpic interactions between A and B segments (Figure 1.6a). On the other hand, the effects of compressible solvents in diblock copolymers with lower disorder-order transitions are significantly different. Namely, that sorption of small amounts of compressed solvent causes a free volume mismatch between polymeric components that induces lower critical phase transitions at temperatures hundreds of degrees below those at ambient conditions (Figure 1.6b).

Although the effect of compressible fluids in thin film BCPs has been scarcely studied, there is evidence that suggests a strong influence of interfaces in the phase behavior of confined diblock copolymers. Experiments on a symmetric diblock copolymer with an upper ODT (PS-b-PMMA) show enhanced immiscibility of the polymer when subject to supercritical CO_2 environments[46]. The authors suggest that the differences in CO_2 absorption (selectivity) and compressibility between the two blocks becomes exacerbated with decreasing film thickness and creates density fluctuations that ultimately lead to enhanced phase segregation. Subsequently, Shah and coworkers[47] provided a theoretical calculation where they show that the interplay between confinement, and the solvent's selectivity and compressibility can lead to a change in the ordering behavior that agrees qualitatively with the experimental results of reference 46.

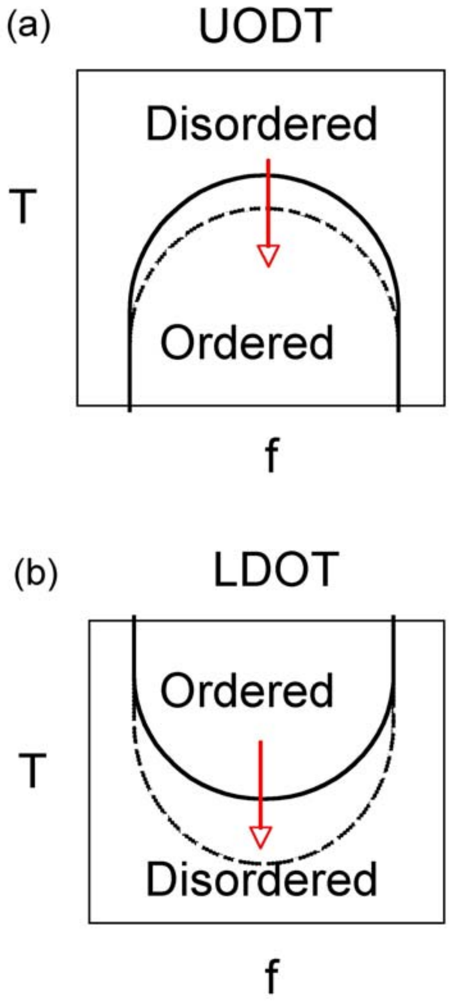

Figure 1.5: Schematic representation illustrating the effect of CO_2 sorption on the phase behavior of a bulk block copolymer with (a) upper order-disorder transition (UODT) temperature and, (b) lower disorder-order transition (LDOT) temperature. The solid curves show the phase diagram under vacuum conditions whereas the dashed curves show the phase diagram under CO_2 conditions.

1.5 REFERENCES

1. Balazs, A. C.; Emrick, T.; Russell, T. P. *Science* **2006,** 314, (5802), 1107-1110.
2. Bockstaller, M. R.; Mickiewicz, R. A.; Thomas, E. L. *Advanced Materials* **2005,** 17, (11), 1331-1349.
3. Zamborini, F. P.; Leopold, M. C.; Hicks, J. F.; Kulesza, P. J.; Malik, M. A.; Murray, R. W. *Journal of the American Chemical Society* **2002,** 124, (30), 8958-8964.
4. Janssen, R. A. J.; Hummelen, J. C.; Saricifti, N. S. *Mrs Bulletin* **2005,** 30, (1), 33-36.
5. Ouyang, J. Y.; Chu, C. W.; Szmanda, C. R.; Ma, L. P.; Yang, Y. *Nature Materials* **2004,** 3, (12), 918-922.
6. Hooper, J. B.; Schweizer, K. S. *Macromolecules* **2005,** 38, (21), 8858-8869.
7. Hooper, J. B.; Schweizer, K. S. *Macromolecules* **2006,** 39, (15), 5133-5142.
8. Hooper, J. B.; Schweizer, K. S.; Desai, T. G.; Koshy, R.; Keblinski, P. *Journal of Chemical Physics* **2004,** 121, (14), 6986-6997.
9. Pryamitsyn, V.; Ganesan, V. *Macromolecules* **2006,** 39, (24), 8499-8510.
10. Starr, F. W.; Schroder, T. B.; Glotzer, S. C. *Physical Review E* **2001,** 6402, (2), -.
11. Starr, F. W.; Schroder, T. B.; Glotzer, S. C. *Macromolecules* **2002,** 35, (11), 4481-4492.
12. Vacatello, M. *Macromolecules* **2001,** 34, (6), 1946-1952.
13. Borukhov, I.; Leibler, L. *Macromolecules* **2002,** 35, (13), 5171-5182.
14. Degennes, P. G. *Macromolecules* **1980,** 13, (5), 1069-1075.
15. Ferreira, P. G.; Ajdari, A.; Leibler, L. *Macromolecules* **1998,** 31, (12), 3994-4003.
16. Gay, C. *Macromolecules* **1997,** 30, (19), 5939-5943.
17. Shull, K. R. *Macromolecules* **1996,** 29, (7), 2659-2666.

18. Striolo, A.; Egorov, S. A. *Journal of Chemical Physics* **2007,** 126, (1), -.

19. Zhulina, E. B.; Borisov, O. V.; Brombacher, L. *Macromolecules* **1991,** 24, (16), 4679-4690.

20. Lee, J. Y.; Buxton, G. A.; Balazs, A. C. *Journal of Chemical Physics* **2004,** 121, (11), 5531-5540.

21. Gupta, S.; Zhang, Q. L.; Emrick, T.; Balazs, A. C.; Russell, T. P. *Nature Materials* **2006,** 5, (3), 229-233.

22. Barnes, K. A.; Douglas, J. F.; Liu, D. W.; Karim, A. *Advances in Colloid and Interface Science* **2001,** 94, (1-3), 83-104.

23. Hamley, I. W., *The physics of block copolymers*. Oxford University Press: Oxford, 1998.

24. Cheng, J. Y.; Ross, C. A.; Smith, H. I.; Thomas, E. L. *Advanced Materials* **2006,** 18, (19), 2505-2521.

25. Chiu, J. J.; Kim, B. J.; Kramer, E. J.; Pine, D. J. *Journal of the American Chemical Society* **2005,** 127, (14), 5036-5037.

26. Hamdoun, B. *European Polymer Journal* **2004,** 40, (7), 1559-1564.

27. Haryono, A.; Binder, W. H. *Small* **2006,** 2, (5), 600-611.

28. Wang, Q.; Nealey, P. F.; de Pablo, J. J. *Journal of Chemical Physics* **2003,** 118, (24), 11278-11285.

29. Thompson, R. B.; Ginzburg, V. V.; Matsen, M. W.; Balazs, A. C. *Science* **2001,** 292, (5526), 2469-2472.

30. Huh, J.; Ginzburg, V. V.; Balazs, A. C. *Macromolecules* **2000,** 33, (21), 8085-8096.

31. Kim, J. U.; O'Shaughnessy, B. *Physical Review Letters* **2002,** 89, (23), -.

32. Schultz, A. J.; Hall, C. K.; Genzer, J. *Macromolecules* **2005,** 38, (7), 3007-3016.

33. Kim, B. J.; Chiu, J. J.; Yi, G. R.; Pine, D. J.; Kramer, E. J. *Advanced Materials* **2005,** 17, (21), 2618-+.

34. Schmaltz, B.; Brinkmann, M.; Mathis, C. *Macromolecules* **2004,** 37, (24), 9056-9063.

35. Lee, J. Y.; Shou, Z. Y.; Balazs, A. C. *Macromolecules* **2003,** 36, (20), 7730-7739.

36. Pham, J. Q.; Johnston, K. P.; Green, P. F. *Journal of Physical Chemistry B* **2004,** 108, (11), 3457-3461.

37. Kazarian, S. G. *Polymer Science, Series C* **2000,** 42, (1), 78-100.

38. Pham, J. Q.; Sirard, S. M.; Johnston, K. P.; Green, P. F. *Physical Review Letters* **2003,** 91, (17), -.

39. Sirard, S. M.; Green, P. F.; Johnston, K. P. *Journal of Physical Chemistry B* **2001,** 105, (4), 766-772.

40. Sirard, S. M.; Gupta, R. R.; Russell, T. P.; Watkins, J. J.; Green, P. F.; Johnston, K. P. *Macromolecules* **2003,** 36, (9), 3365-3373.

41. Sirard, S. M.; Ziegler, K. J.; Sanchez, I. C.; Green, P. F.; Johnston, K. P. *Macromolecules* **2002,** 35, (5), 1928-1935.

42. Hanley, K. J.; Lodge, T. P.; Huange, C.-I. *Macromolecules* **2000,** 33, 2289.

43. RamachandraRao, V. S.; Watkins, J. J. *Macromolecules* **2000,** 33, 5143.

44. Newkome, G. R.; Moorefield, C. N.; Vogtle, F., *Dendrimers and Dendrons: Concepts, Syntheses, Applications*. Wiley-VCH: Winheim, 2001.

45. Pai, R. A.; Humayun, R.; Schulberg, M. T.; Sengupta, A.; Sun, J. N.; Watkins, J. J. *Science* **2004,** 303, (5657), 507-510.

46. Arceo, A.; P.F.Green. *To be published* **2004**.

47. Shah, M.; Pryamitsyn, V.; Ganesan, V. *Journal of Physical Chemistry B* **2007,** 111, (2), 402-407.

CHAPTER 2. Effects of CO_2 on the Stability of Homopolymer Films

2.1 INTRODUCTION

Liquid and supercritical CO_2 processing of thin polymer films has important technological implications. Both liquid and supercritical CO_2 are known to plasticize many polymers, including polystyrene[1, 2]. In lithographic processes CO_2 could function as spin-coating solvent[3] as well as a drying agent to prevent collapsing of small feature sizes in photoresist films, a problem associated with the use of organic solvents, and in the removal of etch residues from low k dielectrics[4-8]. Moreover, CO_2 is a viable non-toxic replacement for organic solvents in nanoparticle impregnation of polymers[9] and in the formation of nonporous films through foaming[10]. The density and solvent quality of supercritical carbon dioxide can be tuned markedly with only small variations in pressure and/or temperature. Thus, modest changes in the processing conditions can enable effective manipulation of the interfacial, thermodynamic, and transport properties of polymer films.

Reprinted with permission from Meli, L., Pham, J. Q., Johnston, K. P., Green, P. F, *Physical Review* , 051601, 69 (**2004).** Copyright © 2004 American Physical Society. **http://link.aps.org/abstract/PRE/v69/p051601**

An important issue associated with the use of thin polymer films in various applications is the tendency of these films to exhibit thickness fluctuations at the surface that would eventually become unstable, and the film would "break up" into droplets, dewetting. One of the best known cases of this phenomenon involves polystyrene, PS, films supported by silicon substrates with a native oxide layer in air, or vacuum[11-16].

Numerous studies[13, 15, 17-23] propose that the stability, morphology and dynamics of polymer films can be understood in terms of an excess intermolecular interaction free energy per unit area, or equivalently an effective interface potential, ΔG(h), between the external interfaces (free surface and substrate). Both short- and long-range intermolecular interactions are accounted for in ΔG(h).

The short-range repulsive forces close to the solid surfaces may stem from chain adsorption and compression, and Born repulsion[24]. These forces, however, are often ill defined and are usually assigned a general analytical representation to capture the effect they have on the interface potential. Some of the most common representations of these forces are exponentially decaying functions of the thickness, h, or Lennard-Jones type of potentials.

In non polar films, the long-range forces are normally taken as dispersive van der Waals forces and as such, are accounted for by the effective Hamaker constant A of the system. Hence, for a non-polar film it is commonplace to write the interaction free energy as,

$$\Delta G\,(h) = -A/(12\pi h^2) + b/h^8, \qquad (1)$$

where *b* is the strength of the short-range interactions. As expected from equation 1, the equilibrium morphology depends on the initial film thickness. For the specific situation involving PS on SiO_x/Si substrates, the form of the van der Waals contribution to the interface potential is modified to include the additional interface created by the silicon oxide layer of thickness d,

$$\Delta G(h) = -\frac{A_{Air-PS-SiO_x}}{12\pi h^2} + \frac{A_{Air-PS-SiO_x} - A_{Air-PS-Si}}{12\pi (h+d)^2} \tag{2}$$

The excess free energy of PS films with air as surrounding medium is a combination of a long-range repulsion and an intermediate-range attraction. That is, the Hamaker constant between the film and the wettable silicon substrate is negative, signifying a long-range van der Waals repulsion. On the other hand, the positive value of the Hamaker constant between the non-wettable silicon oxide coating and polystyrene is a result of an intermediate-range van der Waals attraction[25]. The inclusion of short-range interactions, such as Born repulsion, leads to the global minimum at a finite thickness, as illustrated in Figure 2.1. This scenario will produce spinodal instability at intermediate thicknesses when $\partial^2 \Delta G / \partial h^2 < 0$. Thicker films are stable with respect to a spontaneous (spinodal) process and dewetting of the films occurs by nucleation and growth of holes.

Researchers have examined the interplay between long- and short-range forces by employing a range of strategies, including grafting polymer molecules onto the substrate to form a brush[26], varying the thickness of native oxide layer on the substrate[27], changing the substrate[20], or replacing the medium (air) by liquids such as water or ethylene glycol[28]. In this paper we are particularly interested in the influence of a CO_2 medium on the stability of liquid PS films (h<100nm) supported by SiO_x/Si substrates (CO_2/PS/SiO_x/Si).

We examined the structural stability of PS films (5 nm<h<100nm) supported by SiO_x/Si substrates in liquid and supercritical CO_2 environments over a temperature range from 25°C to 50°C. The PS films, which are plasticized in this temperature range, were found to be metastable, wherein holes nucleated and increased in size. Calculations of the effective interface for the system suggests that the barrier to nucleation is higher in CO_2 than in air and at vanishingly small PS volume fractions the films should be stable. We propose that the kinetics of destabilization are controlled by three factors, film thickness, CO_2 pressure (which dictates the amount of CO_2 mixed in the film) and temperature.

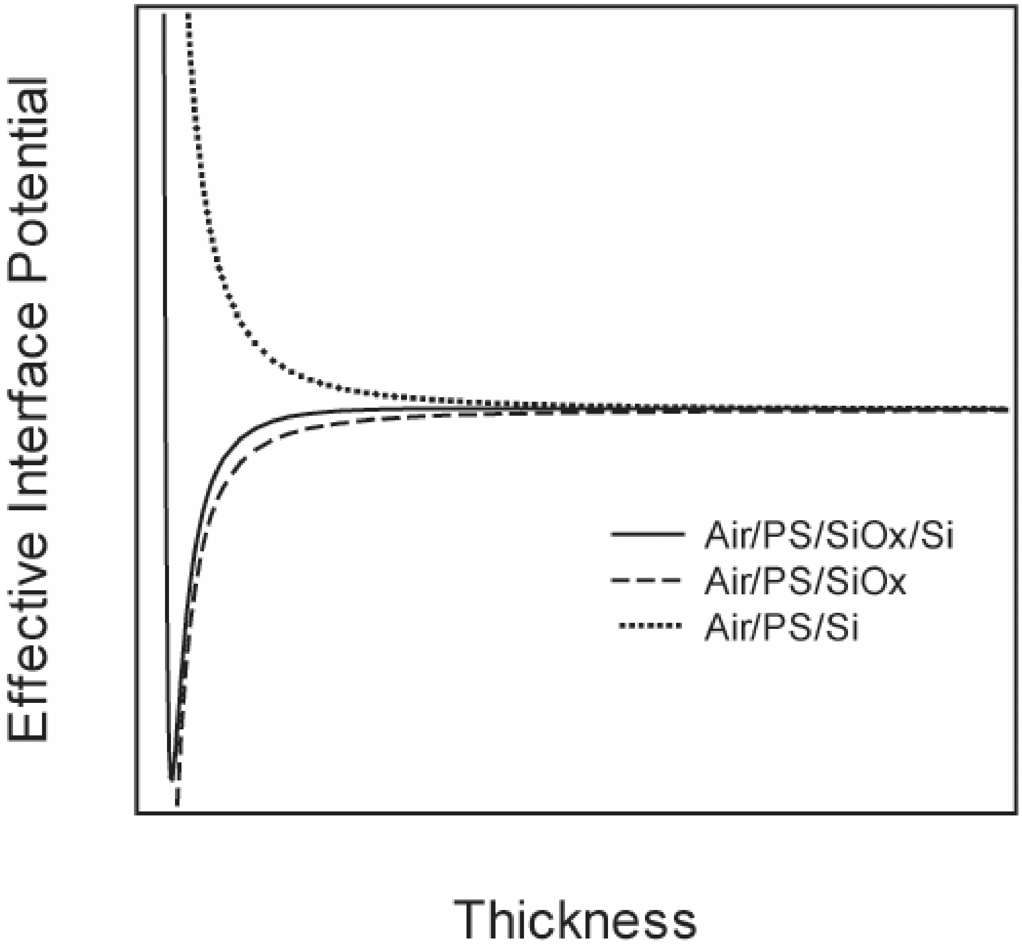

Figure 2.1: Schematic of the thickness dependent effective interface potential of a PS film on an oxide covered silicon substrate, illustrating long- and short-range contributions. There is a long-range van der Waals repulsion between the substrate and PS. The dispersive attraction between silicon oxide and PS is of intermediate-range when the oxide layer in the substrate is thin. A short-range repulsion near the solid surface leads to the minimum in the potential curve.

2.2 EXPERIMENTAL SECTION

Thin films with thicknesses between 5 and 90 nm were prepared by spin-coating toluene (EM Science) solutions of polystyrene (M_w=90,000, M_w/M_n=1.04), purchased from Pressure Chemical, onto silicon substrates (orientation 100). The silicon wafers (Wafer World Inc.) were previously cleaned by soaking in a 1:1 (w/w) methanol (EM Science)/hydrochloric acid (EM Science) solution for 30 minutes. Subsequently, they were rinsed with deionized water (NANOpureII, Barnstead) and dried with nitrogen gas (Matheson Gas Products, >99.999%). The wafers were then soaked in 95% sulfuric acid (Mallinckrodt, analytical grade) for 30 min, rinsed once more with deionized water and dried. The silicon substrates had a native SiO_x layer of approximately 1.7 nm as measured by spectroscopic ellipsometry (J.A. Woollam Co., Inc.). The surfaces of the films were flat and smooth, exhibiting no topographical features, when spun from solution. Prior to annealing, the polymer films were scored to expose the underlying substrate.

The samples were then loaded into a fixed volume cell, which was subsequently sealed and pressurized with carbon dioxide (Air Products, >99.999%) using a manual pressure generator (High-Pressure Equipment Co.) and heated to the desired temperature in a water bath. The pressure was controlled with a strain gauge pressure transducer (Sensotec) calibrated to within $\pm 7 \times 10^{-3}$MPa. Vitrification in these systems is determined by pressure and temperature. We note that, at the conditions studied, 25°C, 35°C and 50 °C and a CO_2 pressure of 31 MPa, all the CO_2-PS systems are in a plasticized state[1, 2]. The cell was cooled to approximately 25 °C and depressurized by venting CO_2 as a vapor from the top of the cell after processing samples for a period of 120 hours. In the process of depressurization and cooling, the film returns to the glassy state and the morphology of the film is frozen.

Some additional samples in the same thickness range were processed for shorter periods of time (10 and 40 hours). Since it was observed that the exposure time changed the dewetting pattern (the stage of structural evolution) in samples otherwise identical, we are able to confirm that the morphology encountered is not an effect of the depressurization process.

The samples were probed with Autoprobe CP scanning force microscopy (SFM) from Park Scientific. Ex-situ images of the surface morphologies were taken with the SFM operating in the contact mode.

Finally, contact angles were approximated by taking the radial cross section of the droplets using SFM. The contact angle measurements were obtained from the macroscopic dimensions of the droplets since local forces can distort the shape in the vicinity of the contact line[29]. Measurements of the drop radius, r, and height, H, yield the "macroscopic" contact angle using: $\tan \theta/2 = H/r$.

2.3 RESULTS

Generally, we found that ultrathin liquid PS films dewet the substrate at a much more rapid rate than thicker films in CO_2 environments, which is not unexpected. Liquid PS films of comparable thickness annealed in vacuum at 130°C, 30°C above the glass transition temperature, ruptured and dewet completely over similar time scales. At higher temperatures the process was more rapid, as one would anticipate.

We now describe our data in supercritical CO_2 at 50°C. SFM images of the topographies of PS films of varying thicknesses, processed in CO_2 at T= 50°C for 5 days (CO_2 density of 0.88 g/cm^3), are shown in Figure 2.2. Holes nucleated in films in the thickness range 20 nm ≤ h ≤ 34 nm, whereas the thinner films, h ≤10 nm, completely dewet, forming droplets. On the other hand, films of h=90 nm show no evidence of rupturing during this period

Experiments conducted at T=35°C reveal qualitatively similar results, as shown by the representative topographies presented in Figure 2.3. Samples of h ≥ 30 nm annealed at 35°C (CO_2 density of 0.94 g/cm^3) show no signs of rupturing after five days, while films of thickness h ≤ 21 nm exhibited signs of dewetting during this period. Finally, with regard to PS films annealed in liquid CO_2 at a temperature of 25°C (density of 0.97 g/cm^3), films thinner than 10 nm ruptured and dewet, whereas thicker films remained flat and smooth after annealing for 120 hours, as shown in Figure 2.4.

Overall, these results indicate the kinetics of destabilization increased with increasing temperature. Secondly, the thickness range of apparent kinetic stability increased with decreasing temperature.

Naively, one might interpret the former statement as an obvious one, namely that the kinetics increase with thermal energy, k_BT. However, there are three other factors to consider. (1) The PS films are plasticized by CO_2 and the CO_2 solubility increases with decreasing temperature. In fact, the CO_2 compressibility is a maximum near 35°C. (2) Moreover, this phenomenon is film thickness dependent, where the effect of plasticization increases with decreasing film thickness. (3) The shape of the effective interface potential is influenced by CO_2 volume fraction, and as we show later, as the CO_2 volume fraction approaches 1, the system should become thermodynamically stable.

In the next section, we calculate the effective interface potential for these systems and discuss the issues of wetting of PS on SiO_x/Si substrates in air/vacuum and in CO_2 environments. We subsequently discuss the issue of the thickness and temperature dependence of the kinetics

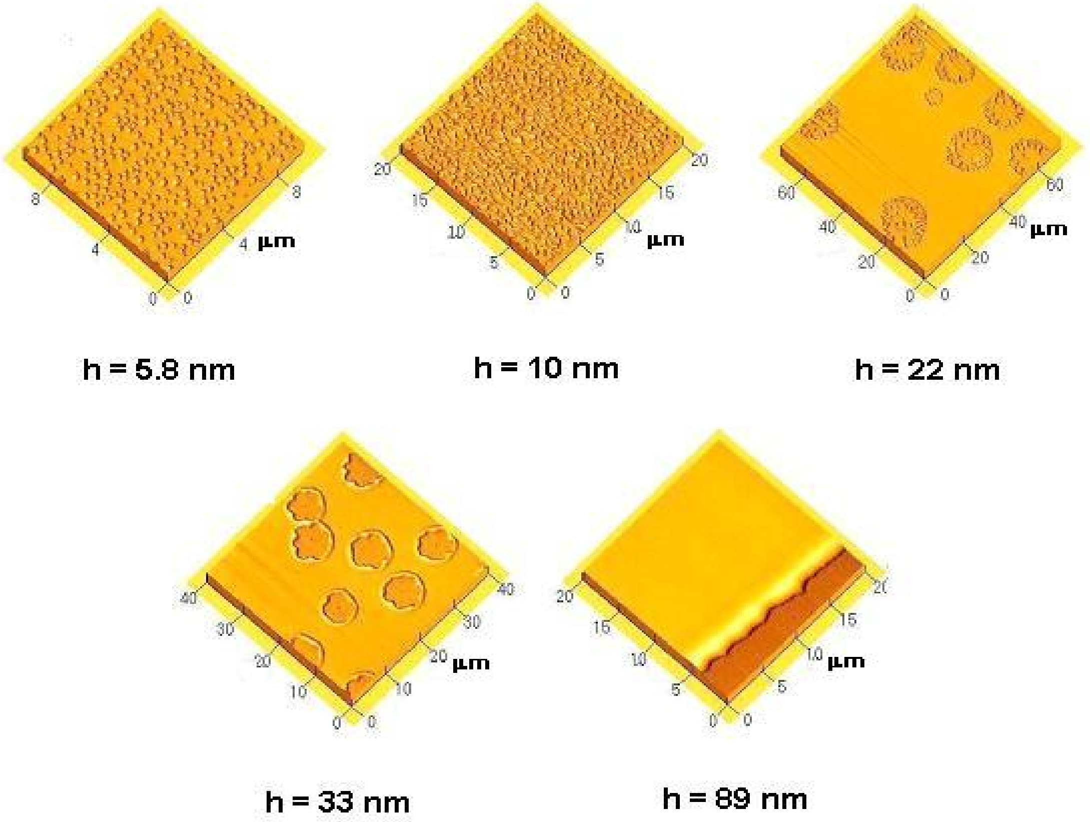

h = 5.8 nm

h = 10 nm

h = 22 nm

h = 33 nm

h = 89 nm

Figure 2.2 Three-dimensional SFM images of the thickness dependent stability of PS films annealed in supercritical CO_2 at 50°C and 31 MPa, after 120 h. The calculated volume fraction of CO_2 in the films is 0.14. Films of thickness $h \leq 33$ nm dewet the substrate. Prior to annealing, the polymer films were scored to expose the underlying substrate, as seen on the film with thickness h =89nm.

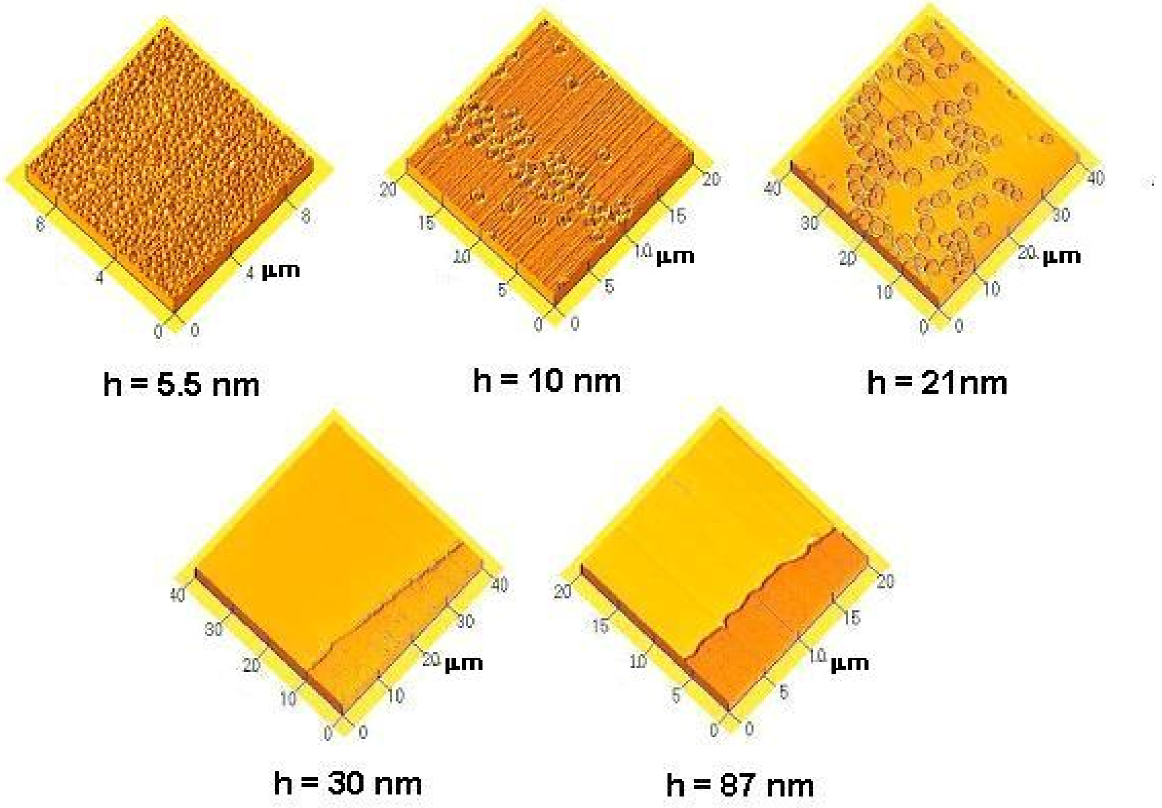

h = 5.5 nm h = 10 nm h = 21nm

h = 30 nm h = 87 nm

Figure 2.3 SFM images of the stability of PS films in supercritical CO_2 at 35°C and 31 MPa after 120 h. The approximate volume fraction of CO_2 in the films is 0.16. Films ruptured when $h \leq 21$ nm. Thicker films, $h \geq 30$ nm, showed only the score made to monitor changes in thickness with respect to the bare substrate.

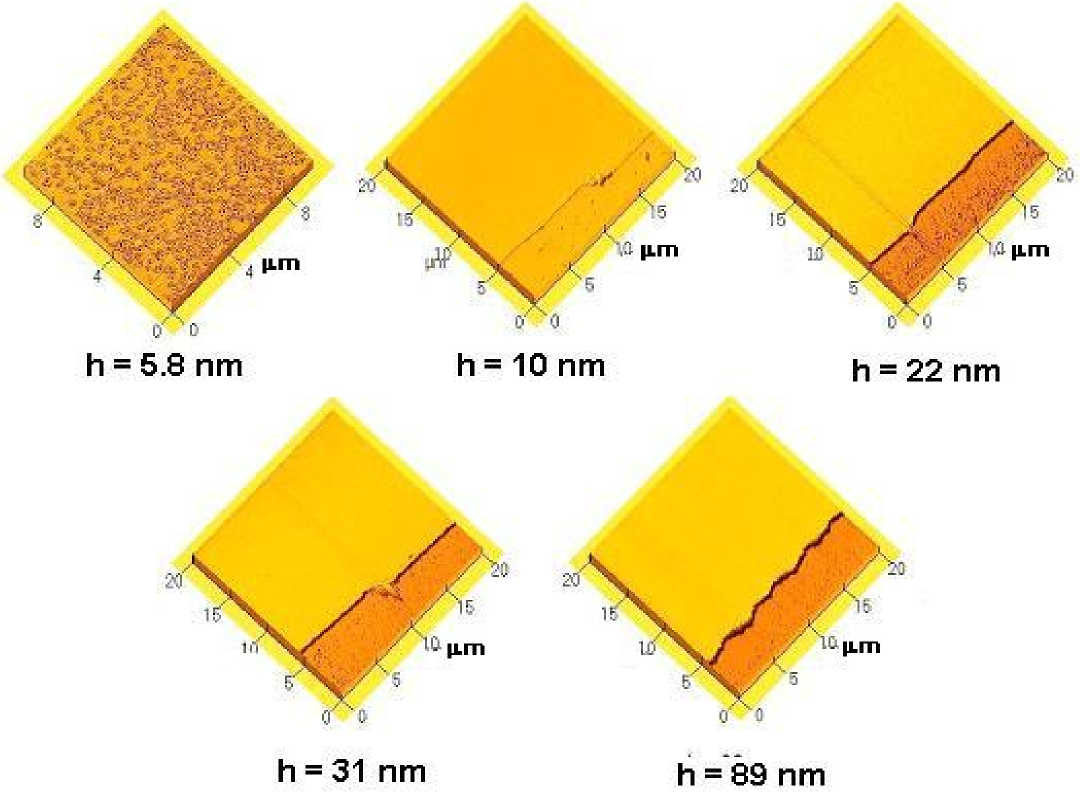

h = 5.8 nm

h = 10 nm

h = 22 nm

h = 31 nm

h = 89 nm

Figure 2.4 SFM Images of the thickness dependent stability of PS films in liquid CO_2 at 25°C and 31 MPa after 120 h of annealing. The volume fraction of CO_2 in the films is 0.17. The thinnest film, with thickness h = 5.8nm, showed hole formation. Films with thickness $h \geq 10$ nm showed only the score made prior to annealing.

2.4 CALCULATIONS OF THE EFFECTIVE INTERFACE POTENTIAL

The van der Waals free energy of interaction per unit area for the three interface system, CO_2/PS/SiO_2/Si, has the same functional form of equation (2), but with Hamaker constants of the film on the oxide layer and on the substrate, $A_{CO_2-PS'-SiO_x}$ and $A_{CO_2-PS'-Si}$, respectively,

$$\Delta F(h) = -\frac{A_{CO_2-PS'-SiO_x}}{12\pi h^2} + \frac{A_{CO_2-PS'-SiO_x} - A_{CO_2-PS'-Si}}{12\pi(h+d)^2}. \qquad (3)$$

The prime on PS indicates that the sorption of carbon dioxide within the film is considered in the calculation of both constants.

The following *combining* relation was used to calculate these non-retarded Hamaker constants:

$$A_{132} \approx \left(\sqrt{A_{11}} - \sqrt{A_{33}}\right)\left(\sqrt{A_{22}} - \sqrt{A_{33}}\right) \qquad (4)$$

The values taken for the silicon and silicon oxide constants, $A_{\text{Si-Si}} = 21.1\times10^{-20}\,J$ and $A_{\text{SiOx-SiOx}} = 5\times10^{-20}\,J$, agree well with experimental measurements reported in literature[15, 30, 31]. For the CO_2 phase, and the CO_2-filled PS phase, we used a simplification of the Lifshitz theory through which the Hamaker constants of two identical macroscopic phases interacting across vacuum is given by[31],

$$A_{11} = \frac{3}{4}kT\left(\frac{\varepsilon_1 - 1}{\varepsilon_1 + 1}\right)^2 + \frac{3h\nu_e}{16\sqrt{2}}\frac{\left(n_1^{\,2} - 1\right)^2}{\left(n_1^{\,2} + 1\right)^{3/2}}. \qquad (5)$$

The dielectric constants are 2.55 for PS[32], 1.518 for CO_2 at 31 MPa and 50ºC, and 1.570 for CO_2 at 31 MPa and 25ºC[33]. The refractive indices are 1.557 for PS[32], 1.228 for CO_2 at 31 MPa and 50ºC, and 1.207 for CO_2 at 31 MPa and 25ºC[34]. The Lorentz-Lorentz mixing rule was used to calculate the refractive indices of the CO_2/PS mixtures from the pure component indices, assuming ideal mixing,

$$\frac{\left(n_{mix}{}^2-1\right)}{\left(n_{mix}{}^2+2\right)}=\sum \phi_i \frac{\left(n_i{}^2-1\right)}{\left(n_i{}^2+2\right)} \quad , \tag{6}$$

where n_i is the refractive index and ϕ_i is the volume fraction of component i.

For the purposes of our calculation, we will assume that the concentration of CO_2 in the film is uniform. This is not an unreasonable assumption since any excess CO_2 in the vicinity of the interfaces occupies a very narrow region of thickness small (~ 1 nm) compared to the film thickness. The ideal mixing assumption mentioned before is not entirely accurate since volume changes of a few percent are expected in these systems. However, the influence of the volume expansion on the value of the effective Hamaker constant should be a second order effect. The volume fraction of CO_2 was estimated to be approximately 0.14, 0.16 and 0.17, at 50°C, 35 °C and 25°C, respectively, in each film[35].

The refractive indices of the 14 vol% and 17 vol% CO_2/PS mixtures were 1.518 and 1.511, respectively. By replacing n with $\varepsilon^{1/2}$ in the mixing rule expression, we estimated the dielectric constant of the mixtures to be 2.419 at 50ºC, and 2.397 at 25ºC.

With the dielectric constants and refractive indices of all the phases in each system, we were in a position to compute their respective Hamaker constants with equation (5). Thus, the system at 50ºC and 31 MPa has $\mathrm{A}_{\mathrm{CO_2\text{-}CO_2}} = 1.44\times10^{-20} J$ and $\mathrm{A}_{\mathrm{PS'\text{-}PS'}} = 7.52\times10^{-20} J$, while the system at 25ºC and the same pressure has $\mathrm{A}_{\mathrm{CO_2\text{-}CO_2}} = 1.73\times10^{-20} J$ and $\mathrm{A}_{\mathrm{PS'\text{-}PS'}} = 7.35\times10^{-20} J$. These constants, along with equation (4), allowed us to obtain the long-range contribution to the interface potential. At this point, it is important to note that the Hamaker constants were also calculated using the complete Lifshitz theory by constructing the dielectric response function of each material using refractive index vs. wavelength data. This procedure yielded similar results as the one described above.

The repulsive interactions that prevent divergence of the dispersive forces when h approaches zero were modeled with a Born-like repulsion term: $\Delta G = \Delta F + b/h^8$. The constant "b" of the short-range contribution was estimated by measuring contact angles of PS on the substrate. That is, with the surface tension of the polymer, we obtained the values of the free energy at the thicknesses where the minima lie by using the extended Young-Dupré equation[36]:

$$\cos\theta = 1 + \frac{\Delta G(h_{\min})}{\gamma_{lv}}. \qquad (7)$$

Then, we adjusted the value of "b" such that the value of the minimum, $\Delta G(h_{min})$, as obtained form minimizing the gibbs free energy expression, matched the value calculated with equation (7).

The measured contact angle of PS above Tg was 28.5±2°, over a temperature range of 140^0C-180^0C. For films annealed in CO_2 at 35°C the average contact angle was 46.9±3°, while at 50°C it was 45.3±4° (in the case of PS films annealed in CO_2 at 25°C it was not possible to measure contact angles, since no droplet formation was observed in any sample). This means that there was no appreciable change in the contact angle between the two temperatures within experimental error. Consequently, the contact angle for the calculation of the depth of the minima in all CO_2/PS/SiOx/Si systems was fixed to a value of 46°. It is noteworthy that the contact angle of PS droplets in CO_2 is considerably higher than that in air, indicating that the wettability of polystyrene on SiO_x/Si substrates decreases in CO_2. This statement also confirms the notion that the stability of the thick PS films in CO_2 must be dictated by the dispersive properties of the substrate, regardless of the short-range interactions with the substrate.

2.5 DISCUSSION

The effective interface potential curves predicted by the calculations are presented in Figure 2.5. As in the case of liquid PS in air, the curves for the CO_2/PS'/SiOx/Si systems at 50°C and 25°C describe metastable films that result from a combination of dispersive long-range repulsion with shorter-range attraction. However, in the case of PS in CO_2, the curves shift to smaller values of h as the CO_2 content in the film is increased. We also observe that the magnitudes of the maxima in the potential curves of PS in CO_2 environments are greater than that of PS in vacuum. As the height of the maxima rises with increasing CO_2 content, a higher barrier to nucleation will be established that effectively opposes dewetting of the films. Furthermore, the shifts in the effective interface potential curves imply that spinodal stability ($\partial^2\Delta G/\partial h^2 > 0$) of the PS films should be achieved in thinner regimes when CO_2 acts as bounding fluid, as illustrated in Figure 2.6. Unfortunately, we were unable to confirm this observation experimentally, since the films that would lie in the spinodal regimes are too thin to form smooth, continuous, films when spun from solution.

It is important to mention that a wetting layer was experimentally observed in all CO_2/PS'/SiO_x/Si systems as seen in Figure 2.7, which confirms the existence of a minimum in the interface potential. Its thickness, however, is larger than the value of h_{min} predicted by the calculations.

Qualitatively, the model suggests that the barrier to nucleation of holes in PS films in the CO_2 environments is larger than that in atmospheric environments. In fact, further increases in the CO_2 content of the film, achieved by increasing the pressure or decreasing the temperature, have the effect of increasing the magnitude of the maximum (barrier) in the interface potential. In the limiting case where the volume fraction of PS is negligible, we would effectively have a layer of pure CO_2. Since the Hamaker constant of a Si/SiOx/CO_2 system is negative for a wide range of processing conditions, one would expect stability of the CO_2 layer. Therefore, in principle one could achieve complete thermodynamic stability if the uptake of carbon dioxide reaches a critical value where $A_{Air\text{-}PS'\text{-}SiOx}$ becomes negative. However, in practice it becomes increasingly difficult to augment the content of CO_2 because the slope of the sorption isotherms above the compressibility regime is very small[37]

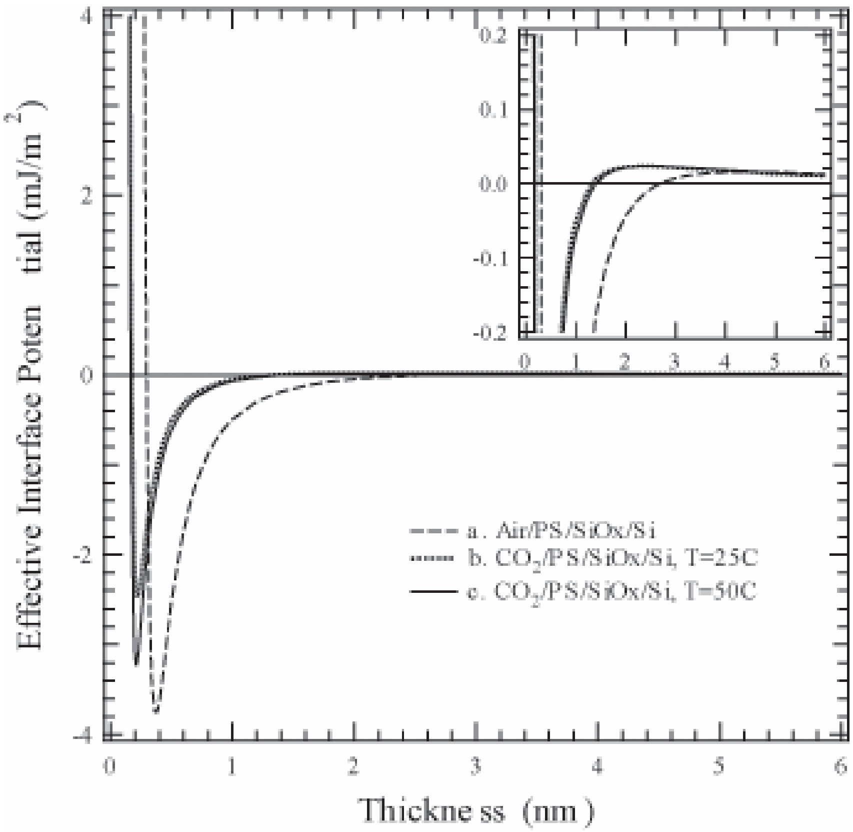

Figure 2.5 The calculated effective interface potential as a function of film thickness for a model PS film in silicon substrate with a native oxide layer of thickness d = 1.7nm. Curve (a) represents the case where the bounding fluid is air: $A_{\text{Air-PS-Si}}$ = -4.87x10-20 J, $A_{\text{Air-PS-SiOx}}$ = 2.93x10-20J, $\gamma_{\text{PS-Air}}$ = 31 mJ/m^2, θ = 28.5°. In curve (b) the bounding fluid is liquid CO$_2$ at T = 25°C and P = 31 MPa: $A_{\text{CO2-PS'-Si}}$ = -2.78x10-20 J, $A_{\text{CO2-PS'-SiOx}}$ = 6.63x10-21 J, ϕ = 0.17, $\gamma_{\text{PS-CO2}}{}^{41}$ = 8 mJ/m^2, θ = 46°. Curve (c) has supercritical CO$_2$ at T = 50°C and P = 31 MPa:$A_{\text{CO2-PS'-Si}}$ = -3.02x10-20J, $A_{\text{CO2-PS'-SiOx}}$ = 7.81x10-21J, ϕ = 0.14, $\gamma_{\text{PS-CO2}}{}^{41}$ = 10.5 mJ/m^2, θ = 46°. The inset presents an enlarged view at small potentials.

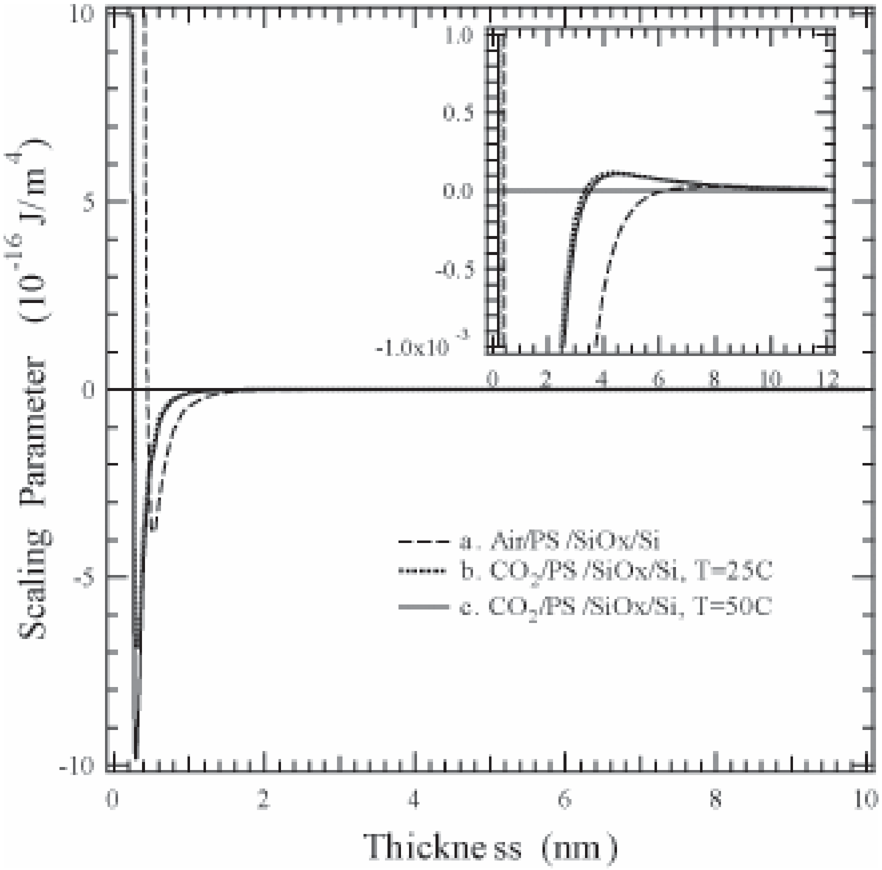

Figure 2.6 Second derivative of the effective interface potential with respect to film thickness for a PS film on a silicon substrate. The parameters used to calculate each curve are presented in caption in figure 2.5.

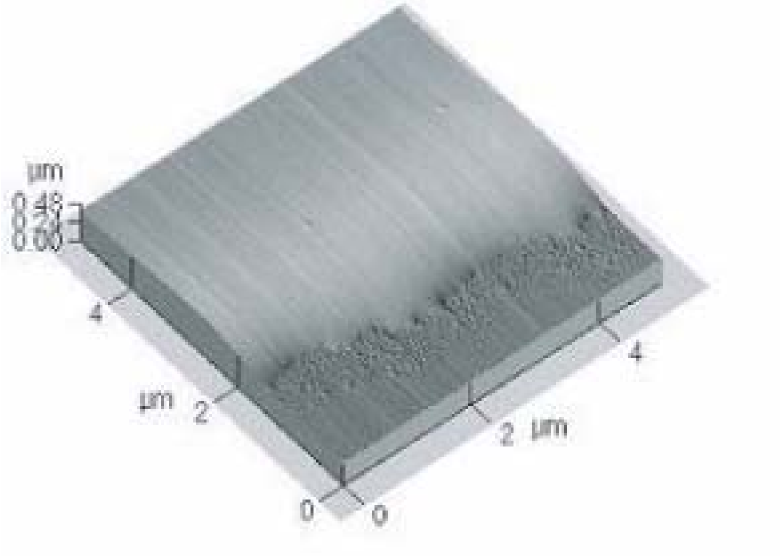

Figure 2.7 5x5 µm SFM image of a 89 nm thick film in supercritical CO_2 at 50°C and 31 MPa, after 120 h. In the image we can discern between the bare substrate exposed by the scoring made prior to annealing, and the wetting layer that has ruptured and formed droplets.

The model also suggests that the behavior of the films at 25°C and 50°C should be similar, since in reality the difference in CO_2 absorption between the two temperatures is small (approximately 3%). That is, identical samples of a given thickness should exhibit similar morphologies at equilibrium, regardless of which temperature is chosen to anneal the films. Nevertheless, experimentally we observe an apparent increase in the structural stability of the samples in the time scale of our experiments. We are therefore lead to believe that the difference in morphologies of the films at the different temperatures should be primarily related to kinetics.

In air or vacuum environments, the kinetics of destabilization should be largely dictated by two parameters: thickness, and thermal energy, k_BT. One can envision that in CO_2 environments a third parameter may come into play namely, CO_2 pressure. More specifically, if the vitrification (liquid to glass) transition pressure is P_g then, $\Delta P = P-P_g$ is a key parameter for understanding the kinetics of destabilization of the films. This issue is examined in further detail below.

It is well established that the T_g of a polymer film exhibits a thickness dependence under atmospheric environments when the thickness is sufficiently small[38-40]. In a similar fashion, the CO_2 pressure at which devitrification of a polymer film occurs, P_g, has also been found to be thickness dependent. Specifically, it has been found that lower CO_2 pressures are required to plasticize thinner films[41]. This dependence can be rationalized in terms of the effective amount of CO_2 in the film, which is responsible for the plasticization of the polymer. For several polymers, like PDMS and PS, there exists an enhancement of CO_2 sorption[42, 43] in thin films due mainly to excess CO_2 at the boundaries. As the thickness of a film decreases, the effect of the boundaries on the overall content of CO_2 becomes more pronounced and a decrease of the P_g relative to the bulk can be observed.

In addition, bulk and thin film systems may exhibit atypical vitrification effects under CO_2 environments. Some polymers, like PMMA, undergo the expected vitrification when decreasing the temperature isobarically, due to loss of configurational entropy. However, upon further cooling, they devitrify because of the increase in the solubility of CO_2 with decreasing temperature at a given pressure[1]. The phenomenon is known as retrograde vitrification, and it is characterized by a vitrification envelope below a maximum pressure on a pressure vs. temperature plot, as seen in Figure 2.8. It has been observed in bulk and thin film PMMA and PEMA, but does not occur in bulk PS. Recent experimental work, however, has shown that retrograde vitrification does indeed occur in thin film PS systems. A detailed account of these results and their implications can be found in the work of Pham et al[44].

In the aforementioned work, measurements of the CO_2-induced devitrification of PS were performed at different thickness and at isotherms of 25, 35, 50 and 75°C. A representative curve of their data at a thickness of 17nm is presented in Figure 2.8. The P_g thickness dependence was fitted to a modified version of the empirical equation proposed by Keddie et al.[38],

$$P_g\,(h)= P_{gbulk}[1-(A/h)^{\delta}], \qquad (8)$$

with adjustable parameters A and δ. The equation describes the P_g vs. film thickness data for PS, at our experimental isotherms and film thickness (see Table 1), reasonably well.

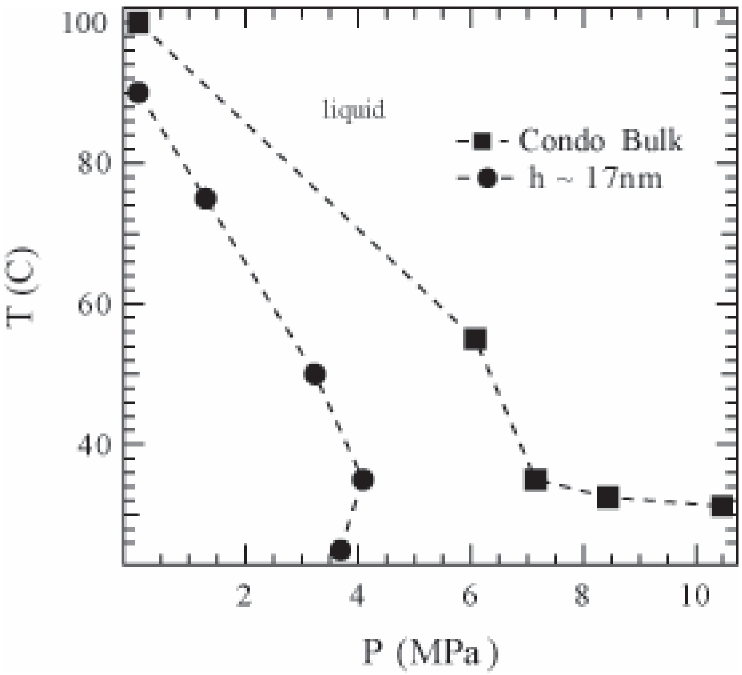

Figure 2.8 Vitrification envelope for a PS thin film with a thickness of h=17nm (circles) and for bulk PS (Condo and coworkers[1]) are shown here. Films outside the relevant envelope are plasticized (liquid). The lines drawn through the data are guides to the eye.

Table 1. Film Plasticization Pressures.

h (nm)	Pg (MPa)			ΔP (MPa)		
	25°C	35°C	50°C	25°C	35°C	50°C
5.5	0.9	1.2	1.0	30.1	29.8	30.0
10	2.2	3.1	2.4	28.8	28.0	28.6
20	3.5	4.3	3.6	27.5	26.7	27.4
30	4.0	4.6	4.0	27.0	26.4	27.0
90	4.8	5.2	4.5	26.2	25.8	26.5

Table 1**.** To the left, the pressures at which the films become plasticized are shown for different temperatures. To the right, the pressures beyond Pg at which films are processed are shown for different temperatures.

As mentioned before, the kinetics of destabilization of the films are determined by the CO_2 pressure, the temperature and by the film thickness. From Table 1 we see that ΔP decreases with increasing film thickness. Hence, in addition to the disjoining pressure, the increasing ΔP with decreasing film thickness contributes to an increase in destabilization kinetics.

It is interesting to note that there should be an enhancement of the kinetics of destabilization at lower temperatures due to the increased solubility of CO_2 at these conditions that leads to lower viscosity of the films. On the other hand, the increased solubility at low temperatures also helps stabilize the films towards hole formation, as suggested by calculations. Despite these two effects, it appears in this case that temperature has a larger impact on the destabilization kinetics, with the fastest kinetics observed at the highest temperature, 50°C.

We can get some insight into the relative contributions of the effects of CO_2 volume fraction compared to that of temperature. This can be accomplished using a model developed by Chow et al.[45] to predict the depression of T_g due to sorption by a gas. The model predicts that

$$\ln\left[\frac{T_g}{T_g(w_{CO_2}=0)}\right] = \beta\left[(1-\theta)\ln(1-\theta)+\theta\ln\theta\right] \tag{9}$$

$$\theta = \alpha\left[\frac{w_{CO_2}}{1-w_{CO_2}}\right]$$

where w_{co2} is the weight fraction of CO_2, and parameters β and α are constants that depend on the polymer and the gas. Values of β and α used to calculate the T_g depression were taken from the literature[46] *(β=0.635* and *α=0.972*) for CO_2 sorption in PS. We now proceed by considering the thick films, where T_g is independent of thickness (h~90nm). At temperatures of 50, 35, and 25°C the thick films should be approximately 30, 27, and

24°C above their T_g, respectively. According to this model a thinner film, of h=14 nm, should be 43, 39, and 35°C above its T_g, at 50, 35 and 25°C respectively. The observed increasing kinetics with increasing temperature is consistent with the notion that the effective viscosities should decrease as the temperature increases above the T_g.

It is clear from the aforementioned that PS films can be processed at low temperatures compared to those required for processing in air. In fact, to achieve the same conditions in air (or vacuum), our estimates suggest that the experiments would have to be conducted between 130° and 140°C, where they are at comparable temperature differences above their T_gs.

2.6 CONCLUSIONS

We showed that thin liquid PS films (h<100nm) supported by SiO_x/Si substrates in liquid and in supercritical CO_2 environments are metastable. Holes nucleate throughout the films, grow, and eventually form droplets on the substrate. The contact angle of the PS droplets in CO_2 environments was found to be significantly higher than that of PS droplets in air, indicating a decrease in the wetting tendency of the polymer on the substrate in CO_2 environments. Estimates of the effective interface potentials suggest that a higher barrier to nucleation exists in the CO_2 environments than in air. In fact, at vanishingly small PS volume fractions in the films, the film should become stable.

In air, increasing the thermal energy of a system results in increased kinetics of destabilization. However in liquid and in supercritical CO_2 environments, competing factors control destabilization of the film. The decreased CO_2 solubility at high temperatures causes slower destabilization kinetics, but augments the stability of the film because of an increase in the effective barrier to nucleation. On the other hand, increases in thermal energy lead to faster kinetics as the viscosity of the film decreases. Thus, there is a delicate interplay between effects due to CO_2 sorption, and those due to temperature. In this case the effects of temperature control the kinetics of destabilization of the PS films.

In any event, it is clear that the morphological structures observed in CO_2 are similar to those in air. However, the main advantage of processing PS in CO_2 is that films can be processes at much lower temperatures with similar results.

2.7 REFERENCES

1 P. D. Condo, D. R. Paul, and K.P.Johnston, Macromolecules 27, 365 (1994).

2 R. G. Wissinger and M. E. Paulaitis, Journal Of Polymer Science: Part B: Polymer Physics 29, 631 (1991).

3 B. J. Novick, R. G. Carbonell, and J. M. DeSimone, Polymeric Material Science and Engineering 84, 51 (2001).

4 S. G. Kazarian, Polymer Science 41, 78 (2000).

5 X. Zhang, J. Q. Pham, H. J. Martinez, et al., Journal of Vacuum Science and Technology B (Submitted 2003).

6 H. Namatsu, Journal of Vacuum Science and Technology B 19, 2709 (2001).

7 C. M. Stafford, T.P. Russell, and T. J. McCarthy, Macromolecules 32, 7610 (1999).

8 D. L. Goldfarb, J. J. d. Pablo, P. F. Nealy, et al., Vac. Sci. Technology B 18 (2000).

9 H. Liu and M. Z. Yates, Langmuir 18, 6066 (2002).

10 S. K. Goel and E. J. Beckman, AIChE Journal 41, 357 (1995).

11 R. Seeman, S. Herminghaus, and K. Jacobs, Journal of Physics: Condensed Matter 13, 4925 (2001).

12 G. Reiter, Physical Review Letters 68, 75 (1991).

13 K. Jacobs and S. Herminghaus, Langmuir 14, 965 (1998).

14 J. A. Forrest, The European Physical Journal E (2002).

15 P. Muller-Buschbaum, P. Vanhoorne, V. Scheumann, et al., Europhys.Lett 40, 665 (1997).

16 J. L. Masson, O. Olufokunbi, and P. F. Green, Macromolecules 35, 6992 (2002).

17 F. Brochard-Wyart and J. Daillant, Canadian Journal of Physics 68, 1084 (1990).

18 G. Reiter, Physical Review Letters 81, 75 (1992).

19 P. G. de Gennes, Rev. Mod. Phys. 57, 827 (1985).

20 R. Limary, P. F. Green, and K. R. Shull, European Physical Journal E 8, 103 (2002).

21 A. Sharma, Langmuir 9, 861 (1993).

22 A. Sharma, Langmuir 9, 3580 (1993).

23 M. P. Valignat, S. Bardon, S. Villete, et al., Fluid Phase Equilibria 150-151, 615 (1998).

24 K. Kargupta, R. Konnur, and A. Sharma, Langmuir 16, 10243 (2000).

25 K. Kagrupta and A. Sharma, Journal of Colloid and Interface Science 245, 99 (2002).

26 G. Reiter, A. Sharma, A. Casoli, et al., Europhys.Lett 46, 512 (1999).

27 R. Seeman, S. Herminghaus, and K. Jacobs, Physical Review Letters 86, 5534 (2001).

28 G. Reiter, A. Sharma, A. Casoli, et al., Langmuir 15, 2551 (1999).

29 E. Vitt and K. R. Shull, Macromolecules 28, 6349 (1995).

30 J. Visser, Advances in Colloid and Interface Science 3, 331 (1972).

31 J. N. Israelachvili, Intermolecular and Surface Forces (Academic Press, 1992).

32 D. B. Hough and L. R. White, Advances in Colloid and Interface Science 14, 3 (1980).

33 M. Hourri, J. M. St-Arnaud, and T. K. Boser, Journal of Chemical Physics 106, 1780 (1997).

34 A. Michels and J.Hamers, Physica IV, 995 (1937).

35 K. Lee and I. C. Sanchez, Private Communication .

36 A. Sharma, Langmuir 14, 4915 (1998).

37 P. D. Condo, I. C. Sanchez, and K.P.Johnston, Macromolecules 25, 6128 (1992).

38 J. L. Keddie, R. A. Jones, and R. A. Cory, Europhysics Letters 27, 59 (1994).

39 J. Q. Pham and P. F. Green, Journal of Chemical Physics 116, 5801 (2002).

40 J. Q. Pham and P. F. Green, Macromolecules 36, 1665 (2003).

41 J. Q. Pham, S. M. Sirard, K. P. Johnston, et al., Physical Review Letters 91, 175503/1 (2003).

42 S. M. Sirard, R. R. Gupta, T. P. Russell, et al., Macromolecules 36, 3365 (2003).

43 T. Koga, Y.-S. Seo, X. Hu, et al., Europhysics Letters 60, 559 (2002).

44 J. Pham, P. F. Green, K. P. Johnston, Journal of Physical Chemistry, accepted January 2004.

45 T. S. Chow, Macromolecules 13, 362 (1980).

46 R. R. Gupta, K. A. Lavery, T. J. Francis, et al., Macromolecules 36, 346 (2003).

Chapter 3. Spatial Distribution of Sterically Stabilized Nanoparticles in Chemically Identical Thin Film Melts

3.1 INTRODUCTION

The grafting of polymer chains onto nanoparticle surfaces is a common strategy to prevent aggregation of the colloidal particles in solution. The tethered chains can extend into solution, creating steric repulsions that can offset the strong van der Waals attractions between nanoparticle cores.

Theoretical approaches[1, 2] were originally employed to describe the structure and interaction between two flat brushes, which correspond to the scenario where the thickness of the polymer brush is much smaller than the diameter of the particles. It has been shown that the interactions between flat brushes are always repulsive under good solvent conditions, promoting particle stabilization. More recent efforts have shown this to be true for spherical brushes, as well (particles for which core and the brush are comparable in size)[3-5].

Changes in the solvent quality can of course lead to brush attraction and colloidal aggregation when the solvent is poor, and unfavorable enthalpic interactions dominate the interactions between particles. Perhaps a more interesting case to consider is when attraction between brushes is promoted by entropic effects alone. Studies of non-adsorbing polymer solutions, where the grafted chains and the free chains are chemically identical, have demonstrated that it is possible to induce an effective attraction between brushes, for both the flat[6, 7] and the spherical brush cases[3]. In these systems, the exclusion of free polymer from the gap between the particles can give rise to an osmotic pressure that induces a depletion attraction between the brushes.

Entropic effects have also been shown to induce attractive interactions between flat brushes when the solvent is completely replaced by a melt of non-adsorbing polymer chains. The large size of the free polymer chains limits their ability to penetrate the grafted chains because of their reduced entropy, forming a so called ‘dry brush’, that is, a brush where only partial penetration of the chains is achieved. The entropic restrictions of the chains in a dry brush may then lead to an effective positive interfacial tension between matrix and grafted chains (a negative spreading coefficient, $S < 0$), which induces the attraction between brushes. In particular, it was found that the entropic attraction between two grafted surfaces exists when $\sigma\sqrt{N} > (N/P)^2$, where σ is the grafting density, and N and P are the lengths of grafted and free chains, respectively[8]. Generally, this means that brushes with high grafting densities embedded in a matrix of long polymer chains tend to attract each other. Indeed, detailed diagrams of state that depend on σ, N, and P, and that document the structure a polymer brush immersed in a melt, have been constructed[2, 7, 9].

The brush structure and wetting transitions of nanoscopic spherical brush in a polymer melt, however, are expected to deviate from the behavior predicted in the aforementioned phase diagrams. The non-negligible particle curvature in these systems should lead to a decrease in steric crowding away from the particle surface[4], which in turn should result in less excluded volume interactions between grafted chains, and possibly to increased wetting relative to the flat brush case[10]. Evidence of changes in the wetting behavior of chains grafted onto curved surfaces has been found experimentally[11, 12].

Of special interest to this work are the results from Shull et at.[12], who reported that curved brushes formed by PS-PVP micelles in a PS film preferentially segregate to the interfaces. The authors argue that the interfacial segregation of the micelles is a manifestation of attractive interactions between polymer brushes, as well as of an attractive interaction between the brush and the free surface. Specifically, they mention that the attraction between brushes stems from entropic loss of the homopolymer matrix chains in the vicinity of the brush, and that the appearance of these attractive interactions between micelles is accompanied by the onset of macrophase separation of the micelle/homopolymer mixture.

Later, Balazs and coworkers[13] performed computational studies of compatible hard-sphere filler/homopolymer mixtures near a non-interacting surface containing a crack. They showed that the particles tend to localize at the damaged wall with significant volume fractions found within the crack. Despite the compatibility between the particles and the polymer, they demonstrate that segregation of the particles to the interface is induced by an entropic depletion attraction between the particles and the surface. That is, the polymer chains expel the particles to the surface (and to the crack) to avoid the loss in conformational entropy incurred by having to stretch around the particles.

In this chapter, we consider the dispersion of gold nanoparticles grafted with PS chains embedded in a PS film. We demonstrate that preferential segregation of particles to the interfaces is commonplace and depends on the grafting density of the brush, the length of both matrix and grafted chains, as well as the relative size of the nanoparticle in comparison to the size of the polymer melt chains. The depth distribution of nanoparticles within the non-adsorbing polymer matrix can be explained as a result of three main effects: (1) an entropic depletion attraction between nanoparticles and interfaces due to the reduced conformational entropy of the matrix chains near a large particle, (2) the interfacial interaction between the polymer host and the grafted brush, and (3) the translational entropy of the nanoparticles which promotes their dispersion within the film.

3.2 EXPERIMENTAL SECTION

3.2.1 Synthesis and Characterization of PS-Coated Gold Nanoparticles

Gold nanocrystals stabilized with thiol-terminated poly(styrene) (PS-SH) were synthesized using a modification of the established two-phase arrested precipitation methods[14]. The initial molar ratio of PS-SH to Au atoms was varied depending on the molecular weight of the PS-SH ligand. Two molecular weights of thiol-terminated PS were used in this study: a low molecular weight PS_{10}-SH (Polymer Source, Inc, M_n = 1000 g/mole, PDI =1.3,) and a relatively high molecular weight PS_{481}-SH (Polymer Source, Inc, M_n = 50,000 g/mole, PDI = 1.06). The gold core size was adjusted by quenching the growth of the Au cores through addition of the thiolated ligands at different reaction times, as reported by Saunders et al.[15]. The reaction product was precipitated in ethanol to remove the supernatant and re-dissolved in toluene. The centrifugation process was repeated several times (10 cycles) to remove unbound thiols and salts. The characteristics of the PS-coated nanoparticles are summarized in Table 3.1.

The average size of the nanocrystals was determined with a JEOL 2010F transmission electron microscope operating at an accelerating voltage of 200kV in scanning mode (STEM) using a high-angle annular dark-field (HAADF) detector. A drop of dilute toluene PS-Au solution was deposited directly on a copper grid (300 mesh) with a thin carbon support film (Ted Pella), and the solvent was allowed to evaporate at ambient pressure and temperature. The average gold core size was obtained by analyzing more than 300 particles using Image J software. The polymer shell thickness was then estimated from the nearest-neighbor distance between particles in the monolayer film, to obtain the total diameter of the nanoparticle (core + shell).

Thermogravimetric analysis (TGA) was used to determine the weight fractions of gold and polymer ligands. The TGA runs were performed under air environments on a TA 2960 instrument at a heating rate of 5°C/min. The grafting densities were estimated with the weight fractions of gold and grafted PS chains, the densities of the species, and the average volume and surface area per gold particle (from TEM Au core size measurements). Greater grafting density is expected in particles with shorter ligand chains. The high grafting density in the Au-PS_{481}-SH nanoparticles is thus unexpected, especially considering the small initial thiol/Au ratio in the synthesis. It is important to note that σ values are extremely sensitive to TGA measurements, as reported by Bansal et al.[11].

3.2.2 Preparation of PS/PS-Coated Gold Nanoparticle Thin Film Composites

To prepare the nanocomposite films, the gold nanoparticles were mixed with PS (Pressure Chemical) solutions to produce a weight fraction of 0.02 of solids in toluene (Fisher Scientific). The weight fraction of Au in the homopolymer was fixed to 0.05 for all samples. Three different molecular weights of PS were used in this work: M_w = 13,000 g/mole (PDI = 1.06), M_n = 152,000 g/mole (PDI = 1.06), and M_n = 900,000 g/mole (PDI = 1.10). The salient characteristics of each nanocomposite film sample are summarized in table 3.2.

Nanocomposite films with thicknesses between 95 to 117 nm were prepared by spin-coating the PS/Au-PSSH solutions on silicon substrates with a silicon nitride layer of 100 nm grown by LPCVD (WaferNet, Inc.). The films were subsequently annealed under a saturated solvent atmosphere at 25°C for different periods of time, depending on the molecular weight of the matrix (10-120 min) to avoid dewetting of the PS films. After solvent annealing, the films were dried in air for approximately 12 h, followed by removal of residual solvent under vacuum for an additional 4 h. Finally, deuterated PS (Polymer Source, Inc, M_n = 41,500, PDI = 2.0) films of approximately 80 nm were spin-coated onto glass slides, floated on water and off the glass substrate, and deposited on top of the nanocomposite films. The films were dried once more in a vacuum for 12 h.

Dynamic secondary ion mass spectrometry (DSIMS) was used to obtain the depth profile of Au within the PS films. Prior to the analysis, the thickness of the film was measured using spectroscopic ellipsometry (J.A. Woollam Co., Inc.). SIMS was performed at UCSB with a Physical Electronics 6650 Quadropole instrument. Sputtering was accomplished with the use of a cesium primary ion beam monitoring negative secondary ions. The negative carbon, deuterium, and silicon secondary ion currents were measured to monitor the stability of the profile, and to serve as indicators of the polymer-air and polymer-substrate interfaces. These profiles, along with the previously determined film thickness, allowed us to convert the sputtering time to a depth scale. Since in these studies we are not concerned about the absolute gold concentration, the Au^- signal was scaled with the total number of Au^- counts to obtain a the relative concentration of gold across the film.

Table 3.1 Physical Characteristics of the PS-Coated Gold Nanoparticles

Nanoparticle	Thiol/Au ratio, f_{PS}[a]	M_n (g/mole)	$<D_{Au}>$ (nm)[b]	$<D_{np}>$ (nm)	Areal Grafting Density, σ/a^2 (nm^{-2})	Grafting Density, σ[e]
Au(2)PS_{10}-SH	0.2	1000	1.82 (30%)	4.5	1.8	0.54
Au(5)PS_{10}-SH	0.2	1000	4.99 (24%)	10.0	1.5	0.45
Au(5)PS_{481}SH	0.06	50,000	4.83 (25%)	54.0	1.4	0.42

[a] Initial mole ratio of PS ligands to Au in the particle synthesis. [b]The standard deviation as a percentage of the average particle size is shown in parenthesis. [c]A styrene monomer size of 0.55nm was taken for calculation.

Table 3.2 Characteristics of the Film Nanocomposites

Sample	Nanoparticle	h (nm)	P	N	R_{Au}/R_g	R_{np}/R_g	$\sigma N^{1/2}$	$(N/P)^2$
I	Au(2)-PS_{10}-SH	107	125	9.6	0.3	0.74	1.67	$5.92*10^{-3}$
II	Au(5)-PS_{10}-SH	117	125	9.6	0.83	1.65	1.39	$5.92*10^{-3}$
III	Au(5)-PS_{481}-SH	96	125	481	0.80	8.9	9.21	14.81
IV	Au(5)-PS_{481}-SH	106	1462	481	0.23	2.6	9.21	0.11
V	Au(5)-PS_{481}-SH	117	8654	481	0.10	1.08	9.21	$3.09*10^{-3}$

3.3 RESULTS AND DISCUSSION

This article is organized as follows. The dispersion of the different types of nanoparticles in a given matrix (fixed P) is first described. We then examine how the distribution of each type of nanoparticle changes as we modify the molecular weight of the polymer melt. Finally, we discuss the mechanisms that can lead to preferential enrichment of gold in one of the interfaces that is, to a greater fraction of nanoparticles residing at one of the interfaces.

3.3.1 Effect of Ligand and Core Size on the Spatial Distribution of Nanoparticles

We begin by discussing the dispersion of the Au(2)PS_{10}-SH, Au(5)PS_{10}-SH, and Au(5)PS_{481}-SH nanoparticle in the lowest molecular weight PS thin film host. Lower and upper bounds for the effective size of the nanoparticles, with respect to the unperturbed radius of gyration, R_g, of the host chains are presented in Table 3.2 As a lower bound we take the ratio of the Au core radius, R_{Au}, divided by R_g. For the case of a wet brush, the effective size of the particle should approach this ratio, i.e. $R_e \approx R_{Au}/R_r$. This is because the matrix chains penetrate all the way to the core surface.. On the other hand, the upper bound is considered to be the total radius of the nanoparticle (Au core + shell), R_{np}, divided by R_g. This ratio, R_{np}/R_g, should be closer to the effective size of the nanoparticle in the dry brush regime, for which the interface between the brush and the polymer melt is relatively sharp. To compare our systems to the wetting behavior predicted for planar brushes by the self-consistent field (SCF) theory, we also include calculation of $\sigma(N)^{1/2}$ and $(N/P)^2$ in Table 3.2. It is important to emphasize that $\sigma(N)^{1/2}$ =

$(N/P)^2$ is the wetting transition that delimits the regions of negative and positive interfacial energy between the grafted and free chains[8]. This transition differs from the wet-to-dry brush transition; i.e.: from the transition where mobile chains start to be expelled from the brush (the transition is located at $\sigma(N)^{1/2} = (P/N)^{-1/2}$ for $P/N < 1$ and at $\sigma(N)^{1/2} = 1$ for $P/N > 1$). Under these conditions, *all* of our samples have particles in the dry brush regime (interpenetration of grafted and free chains is partial), while only sample III has a negative interfacial energy between brush and melt ($S > 0$).

In Figure 3.1 we present the normalized concentration profiles of Au as a function of PS film thickness for samples I, II, and III. Sample I and II contain particles with short, highly-grafted chains that are not wetted by the matrix chains according to the SCF calculations for planar brushes ($\sigma N^{1/2} > (N/P)^2$). The effective size of the nanoparticles, which should approach R_{np}/R_g for these dry brushes is much smaller for sample I (the Au core diameter of sample II is nearly 3 times greater than that of sample I). The concentration profile for sample II shows two distinct, non-symmetric, Gaussian peaks located at the interfaces of the film (free surface and substrate), while the relative Au concentration drops to zero in the middle region of the film (the middle region comprises approximately 60% of the total film thickness). Thus, the DSIMS analysis reveals that the nanoparticles in sample II are completely segregated at the interfaces of the polymer film. In contrast, the smaller Au particles contained in sample I are more homogeneously dispersed across the film, displaying a very slight enrichment at the interfaces. In this section we will concentrate on explaining why particles migrate to the interfaces as opposed to distributing uniformly across the film, leaving the discussion of the symmetry of these peaks for the last section.

Considering that both samples have grafted particles that lie well within the region of negative spreading coefficient, a repulsive interaction between nanoparticle brush and polymer melt (and an attractive interaction between particles) is anticipated. This repulsive interaction should favor segregation of the particles to the interfaces in the two samples. Additionally, the chains in the vicinity of the particles lose conformational entropy (due to stretching), leading to a polymer-induced depletion attraction between particles and interfaces proposed by Balazs and coworkers[13]. The stretching energy penalty decreases with decreasing particle size since the polymers do not lose as much conformational entropy in stretching around smaller particles (the stretching energy scales as $(D/R_g)^2$). On the other hand, the translational entropy of mixing of the particles should promote dispersion of the particles throughout the material, with the smaller particles exhibiting greater translational entropy than the larger ones. Thus, we propose that the enhanced dispersion observed in sample I in comparison to sample II is related to a considerable decrease in the size of the embedded nanoparticles that increases the translational entropy of mixing of the particles, at the same time reducing the stretching energy of the polymer melt near the particle.

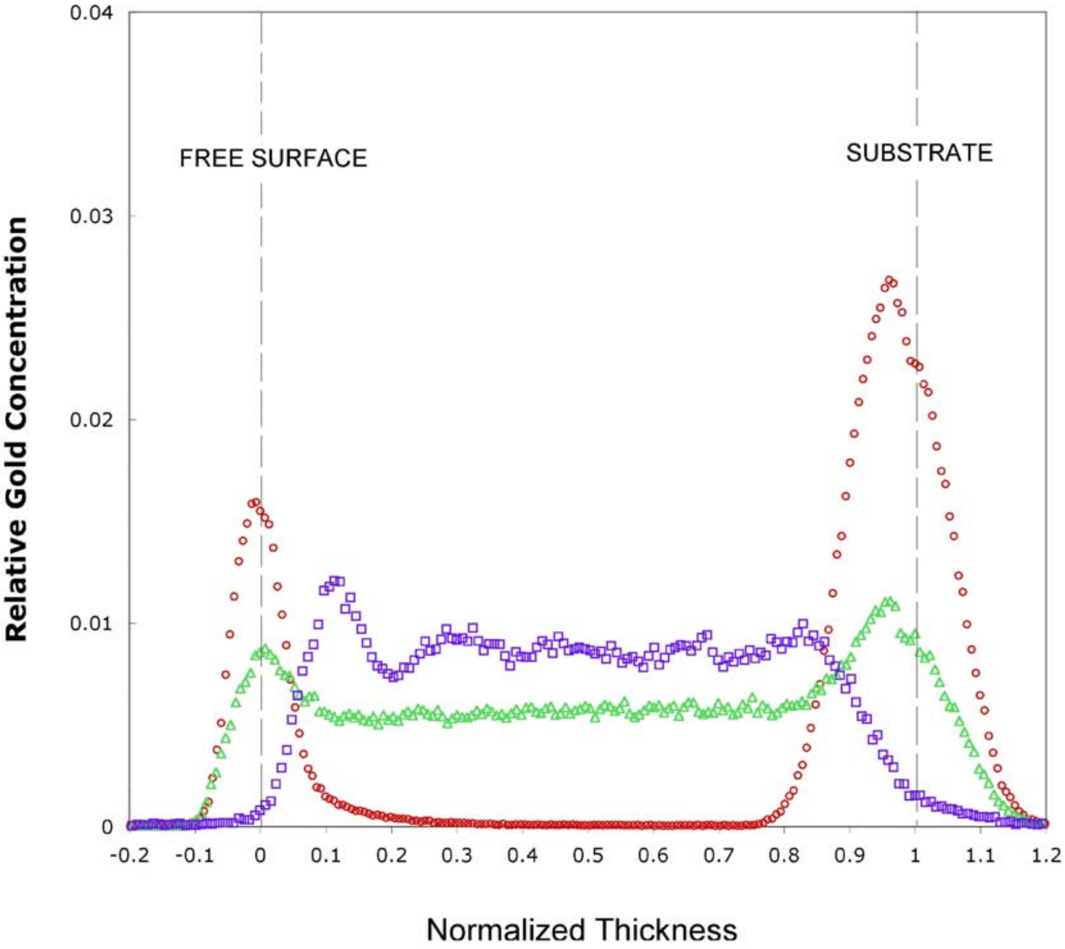

Figure 3.1: Depth distribution of gold nanoparticles in a PS film of M_n = 13,000 g/mole, as measured by dynamic secondary ion mass spectroscopy. Green triangles correspond to the depth profile of Au(2)-PS_{10}-SH nanoparticles (sample I), red circles represent the relative concentration of Au(5)-PS_{10}SH nanoparticles, (sample II), and purple squares correspond to Au(5)-PS_{481}-SH nanoparticles (sample III).

It is important to note that in this analysis we are not taking into account the possibility of increased wetting due to the spherical nature of the particle brush, as mentioned in the introduction. Such an effect should be more significant for the smaller particle, since the brush curvature increases as the radius of the particle decreases, and would be an additional factor that could explain uniform distribution of these nanoparticles in the matrix.

We now analyze sample III, which contains particles with approximately the same Au core size as sample II, but with much longer brush chains ($N = 9.6$ for II, and $N = 481$ for III). Indeed, in this case the grafted chains are longer than the matrix chains ($P/N < 1$), leading to wetting of the brush by the polymer melt ($\sigma N^{1/2} < (N/P)^2$, $S < 0$). However, the penetration of the matrix chains into the grafted ones is only partial, since $\sigma(N)^{1/2} > (P/N)^{-1/2}$. Thus, once more we assume that the effective size of the particle is closer to $R_{np}/R_g(R_{np} = 8.9R_g)$. If size effects dominate dispersion, we would expect more interfacial segregation in this sample than in sample I, which contains very small particles but has a positive spreading coefficient. In fact, the depth profile of Au for sample III (Fig. 3.1) is fairly uniform, with only a small peak at the free surface. Based on the foregoing discussions, we conclude that the negative interfacial energy between brush and polymer melt dominates over the size effects that promote interfacial segregation of the nanoparticles. Nevertheless, it is worth mentioning that a spherical brush with such long grafted chains should allow considerably more interpenetration of the matrix chains than a flat brush of the same characteristics, since it has been shown that the steric crowding in a curved brush decreases monotonically from the core surface[4]. Therefore, the curvature of the brush should attenuate size effects by allowing more interpenetration of grafted and matrix chains.

3.3.2 Effect of Matrix Molecular Weight on Nanoparticle Distribution

Let us consider what happens to the distribution of a given type of nanoparticle within the film if we change the molecular weight of the matrix. Figure 3.2 shows the relative concentration of Au in a 13,000 g/mole (sample III), 152,000 g/mole (sample IV), and 900,000 (sample V) molecular weight matrix for the Au(5)-$PS_{481}SH$ nanoparticles. According to the SCF approximation for flat brushes, only the low molecular weight melt in sample III should wet the particle brush. A transition from a wetting to a non-wetting melt should have a significant impact on nanoparticle dispersion, driving segregation of the particles to the interfaces since brush-polymer interactions become repulsive ($S > 0$ to $S < 0$). On the other hand, the effective size of the nanoparticle should decrease with increasing P. Since all of the brushes are only partially penetrated by the mobile PS chains (dry brushes), we take the upper bound of nanoparticle size (R_{np}/R_g) as R_e such that: $R_e = 8.9$ for III, $R_e = 2.6$ for IV, and $R_e = 1.08$ for VIII. The decrease in relative nanoparticle size with increasing P should promote dispersion by increasing the translational entropy of the nanoparticles as well as by inhibiting the depletion attraction between particle and interfaces.

Figure 3.2 shows that the concentration profiles of samples III and IV are qualitatively similar, exhibiting uniform dispersion of the nanoparticles with only a slight enrichment near the free surface. On the other hand, sample V develops a very broad peak located at the substrate, illustrating a much greater degree of interfacial segregation in this sample. According to the SCF theory the wetting transition should lie between samples III and IV. If this is indeed true, the similarities between the two curves should be merely coincidental. That is, their similarity implies that the opposing driving forces in the system offset one another. Specifically, the tendency for better dispersion imparted by the decrease in particle size as P increases is countered by a change in the sign of the spreading coefficient that enhances interfacial segregation. The concentration profile of sample V would then result from further increase in the repulsive interaction between brush and polymer melt as P increases, an effect which evidently dominates the energetics for this sample (since segregation is enhanced with increasing P).

Once again, this analysis depends on the applicability of the SCF theory to the spherical brushes of our particles. An enhancement in the wetting properties of the melt for the spherical brushes could have possibly shifted the wetting transition in between samples IV and V. This would imply that the interfacial energy between brush and polymer is the dominant driving force for interfacial segregation in coated particles, since the concentration profiles of the samples with the two lowest molecular weights (III and IV) are very similar, even though their size differs considerably (R_e (III) = 3.5 R_e (IV)).

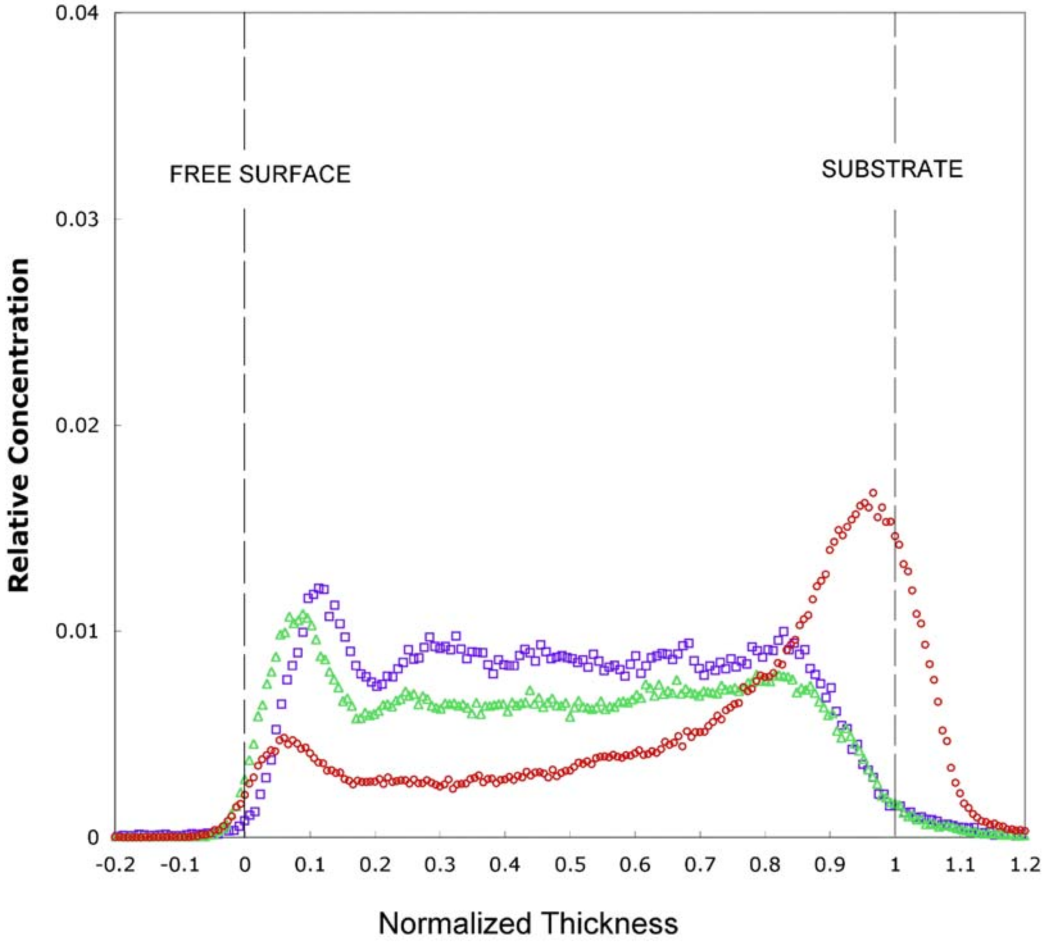

Figure 3.2: Depth distribution of Au(5)-PS$_{481}$-SH nanoparticles in PS films of varying molecular weights, as measured by dynamic secondary ion mass spectroscopy. Purple squares correspond to the depth profile of Au(5)-PS$_{481}$-SH nanoparticles in a PS matrix of M_n = 13,000 g/mole (sample III), green triangles represent the relative concentration of the nanoparticles in a melt of M_n = 152,000 g/mole (sample IV), and red circles correspond to the matrix with M_n = 900,000 g/mole (sample V).

3.3.3 Nanoparticle Partition to Interfaces

In the previous sections we discussed the interplay between energetic interactions that can favor dispersion vs. interfacial segregation. We now turn our attention to the factors that can drive preferential segregation of nanoparticles to one of the interfaces. Figure 3.2, for example, shows that the Au(5)-PS$_{481}$-SH particles enrich the free surface slightly (judging by the very small peak located at this interface in both concentration profiles) when they are embedded in matrices with relatively low molecular weights (III and IV). On the other hand, in the matrix with the highest molecular weight an extremely broad peak appears at the substrate (V), indicating enrichment of Au at this interface.

It is clear that preferential enrichment of one interface should be a consequence of a minimization of the free energy of the system. The conformational entropy of a polymer chain near a hard wall is compromised with respect to that of a chain in the 'bulk' of the film. The same chain near the free surface of the film will experience greater conformational freedom than the average polymer chain. These entropic penalties, and gains, should also be applicable to the grafted chains when a particle is segregated to an interface. Hence, a polymer-coated nanoparticle that is driven to surface should select the interface that minimizes the entropic penalties of grafted and free polymer chains in the vicinity of the substrate (or maximizes the entropic gain of the chains at the free surface). In relatively high molecular weight matrices (P>>N), such as sample V (Fig. 3.2) and sample II (Fig 3.1), the entropy of the system will be maximized when the long matrix chains have more access to the free surface, and thus a greater fraction of the grafted particles will locate at the substrate. Interestingly, sample I (Fig. 3.2) shows a slightly lower degree of nanoparticle enrichment at the substrate, even though the relative size of the matrix chains is this same as in sample II. As the molecular weight of the matrix is decreased (with respect to N), the fraction of nanoparticles that migrates to the substrate should also decrease. Indeed, samples III and IV (Fig. 3.2) show enrichment of gold exclusively at the free surface. This fact is somewhat surprising for sample IV, for which the molecular weight of the matrix is still greater than that of the grafted chains (P>N). However, it is possible that the grafted chains have an additional tendency to segregate to the free surface due to the relatively high concentration of chain ends at the edge of the brush[12].

3.4 CONCLUSIONS

In this work we showed how polymer-coated nanoparticles distribute in a neutral homopolymer film. We propose that the dispersion of nanoparticles across the homopolymer film is the result of three contributions: (1) the conformational entropy of the chains, which induces a depletion attraction between the particles and interfaces that depends on the effective size of particle; (2) the translational entropy of mixing of the particles, which encourages dispersion of the fillers and is also size dependent; (3) the interfacial energy between the grafted and mobile chains that can enhance or hinder dispersion depending on the particular wetting characteristics of the polymer/brush pair. Thus, a prerequisite to understand the interplay of these contributions is the knowledge of the wetting transitions and structure of the brush in the chemically identical polymer melt. General trends obtained from comparing experimental nanoparticle concentration profiles with the existing diagrams of state (N,P, σ) for flat brushes seem to indicate that the sign (and perhaps magnitude) of the spreading coefficient plays a primary role in determining the extent of interfacial segregation of the nanoparticles in the film.

However, greater theoretical understanding of the effect of brush curvature on the phase diagrams is necessary to make a quantitative comparison with our experiment. Experiments on the wetting of the Au-PSSH surfaces by the PS matrices are underway, and should provide further insight into this topic.

3.5 REFERENCES

1. Alexander, S. *Journal De Physique* 1977, 38, (8), 983-987.

2. Degennes, P. G. *Macromolecules* 1980, 13, (5), 1069-1075.

3. Striolo, A.; Egorov, S. A. *Journal of Chemical Physics* 2007, 126, (1), -.

4. Wijmans, C. M.; Leermakers, F. A. M.; Fleer, G. J. *Langmuir* 1994, 10, (5), 1331-1333.

5. Witten, T. A.; Pincus, P. A. *Macromolecules* 1986, 19, (10), 2509-2513.

6. Gast, A. P.; Leibler, L. *Macromolecules* 1986, 19, (3), 686-691.

7. Wijmans, C. M.; Zhulina, E. B.; Fleer, G. J. *Macromolecules* 1994, 27, (12), 3238-3248.

8. Ferreira, P. G.; Ajdari, A.; Leibler, L. *Macromolecules* 1998, 31, (12), 3994-4003.

9. Gay, C. *Macromolecules* 1997, 30, (19), 5939-5943.

10. Yezek, L.; Schartl, W.; Chen, Y. M.; Gohr, K.; Schmidt, M. *Macromolecules* 2003, 36, (11), 4226-4235.

11. Bansal, A.; Yang, H. C.; Li, C. Z.; Benicewicz, R. C.; Kumar, S. K.; Schadler, L. S. *Journal of Polymer Science Part B-Polymer Physics* 2006, 44, (20), 2944-2950.

12. Shull, K. R.; Winey, K. I.; Thomas, E. L.; Kramer, E. J. *Macromolecules* 1991, 24, (10), 2748-2751.

13. Lee, J. Y.; Buxton, G. A.; Balazs, A. C. *Journal of Chemical Physics* 2004, 121, (11), 5531-5540.

14. Brust, M.; Walker, M.; Bethell, D.; Schiffrin, D. J.; Whyman, R. *Journal of the Chemical Society-Chemical Communications* 1994, (7), 801-802.

15. Saunders, A. E.; Sigman, M. B.; Korgel, B. A. *Journal of Physical Chemistry B* 2004, 108, (1), 193-199.

CHAPTER 4. Comparative Study of the Coarsening of Gold Nanoparticles in Poly(methyl methacrylate) Thin Films under Vacuum and Compressed Fluid Environments

4.1 INTRODUCTION

The fabrication of polymer-based composites by incorporating inorganic fillers is nowadays a widespread strategy to improve the performance of polymer systems in a vast range of applications. Nanoscopic inorganic fillers are of special interest largely due to their size-dependent properties: photonic, magnetic, chemical and electronic. Significant property enhancements [1-11], viscosity, diffusion, glass transition, wetting, interfacial processes, optical, thermal, electrical and mechanical properties, are exhibited by these nanocomposites when the dimensions of the particles are comparable to the average chain dimension of the polymer, R_g[10-16].

It is evident that the particle size property dependence, particle composition and spatial distribution, have an important influence on the properties of nanocomposites. However, control over the spatial distribution has posed many challenges largely because the particles exhibit a strong tendency to aggregate and subsequently coarsen during processing[17, 18]. In this paper we examine the structural evolution (coarsening) of the size of dodecanethiol functionalized gold nanoparticles embedded in a poly(methyl methacrylate) film upon processing.

Coarsening is ubiquitous and is responsible for a diverse range of processes that include aerosol aggregation[19, 20], phase separation of liquid-liquid mixtures([21, 22]), the morphology of thin metallic and semiconductor films on substrates([23-26]). Indeed, coarsening models have been shown to provide a good description for social phenomena such as the distribution of city populations and the exchange of wealth between individuals[27]. Two general mechanisms have been proposed to explain late-stage coarsening behavior: Ostwald ripening (OR) and coalescence. OR is a growth process where particles that are fixed in space grow by transferring atoms/molecules from smaller particles to larger ones driven by a difference in their chemical potential. On the other hand, dynamic coalescence involves the collective motion of particles or clusters that grow upon collision increasing the mean cluster size with time. The growth kinetics of the mean cluster size follows a power law for OR, as well as for coalescence when the latter is limited by diffusion of clusters (also referred to as rapid aggregation), such that $\langle R \rangle \propto t^{\beta}$. The value of this power-law exponent can provide insight into the nature of the growth process, but it is, in itself, insufficient to deduce the coarsening mechanism[28]. Using scaling arguments, however, it has been shown that models for both mechanisms can lead to a unique scale-invariant distribution function for the particle size, $F(R/\langle R \rangle)$ vs $R/\langle R \rangle$, in the asymptotic limit ($t \rightarrow \infty$). Thus, comparison of the growth exponent and the asymptotic size distribution function with their corresponding theoretical predictions for OR and coalescence can be an effective means of elucidating the coarsening mechanism of a given system[29, 30].

This study was aimed at understanding the coarsening behavior of the nanoparticles in our nanocomposite films under two processing conditions: thermal annealing above the glass transition temperature in vacuum environments, and supercritical carbon dioxide ($scCO_2$) annealing at low temperatures. The effect of $scCO_2$ annealing is expected to be two-fold. First, CO_2 is expected to plasticize the polymer allowing enhanced mobility of the nanoparticles due to lowering of the polymer viscosity. Further, the plasticization of the polymer by $scCO_2$ should allow for the processing of the films at a low annealing temperature thus preventing thermal desorption of the steric stabilizer. Indeed, our results show that thermal annealing results in a significant increase in the gold nanoparticle diameter, whereas the size of the particles in the nanocomposite processed in supercritical carbon dioxide does not change in the timescale of our experiment. By analyzing the growth kinetics, the distribution of particle sizes, and sequential images of the coarsening of nanoparticles, we also show that the evolution of particle size in the thermally annealed film can be divided into two stages: an initial stage where growth occurs simultaneously through OR and coalescence, and a late-stage characterized by a scale-invariant distribution reminiscent of growth by coalescence. The two different growth regimes are thought to be facilitated by desorption of the dodecanethiol ligands.

4.2 EXPERIMENTAL SECTION

Gold nanocrystals stabilized with dodecanethiol were synthesized by a modification of the two-phase arrested precipitation method reported by Brust et al.[31] using a 1/1 dodecanethiol/$HAuCl_4$ ratio. The gold cores had an average diameter of 4.68 nm with a relatively broad size distribution, $\sigma/\langle R\rangle_{t=0} \sim 21\%$, as determined by HAADF imaging using scanning transmission electron microscopy (STEM).

The gold particles were used to prepare composite solutions with Poly(methyl methacrylate) (Polymer Source, Inc, Mw=92,000g/mole, $M_w/M_n = 1.08$), PMMA, in toluene (Fisher Scientific) yielding a concentration of polymer in solution of 2w/w%. The weight fraction of nanoparticles in the homopolymer was 13w/w%.

Films with thicknesses of approximately 200 nm were prepared by spin-coating the composite solution onto glass slides. After spin-coating, the films were floated on water and off the glass substrate and deposited onto transparent silicon nitride windows (SPI supplies) to achieve film uniformity. Once prepared, the films were annealed in vacuum at 65˚C for a period of 30 h to remove excess solvent. Additional PMMA/Au nanocomposite films and pure PMMA films were spin-coated directly on silicon substrates with a silicon nitride layer of 100 nm grown by LPCVD (WaferNet, Inc.) for dynamic secondary ion mass spectrometry (DSIMS) analysis.

The films were then subjected to one of the following processes: annealing above the glass transition temperature in a vacuum and subsequent quenching to room temperature, or CO_2 annealing. Supercritical CO_2 ($scCO_2$) annealing was achieved by loading the sample into a fixed volume cell, which was sealed and pressurized with carbon dioxide (Air Products, >99.999%) using a manual pressure generator (High-Pressure Equipment Co.) and heated to a temperature of 50ºC in a water bath. The pressure, set to 10 MPa, was controlled with a strain gauge pressure transducer (Sensotec) calibrated to within $\pm 7 \times 10^{-3}$MPa. After each annealing period, the cell was cooled to room temperature and depressurized by venting CO_2 as a vapor from the top of the cell.

Following each annealing period, the films were characterized with a combination of scanning force microscopy and scanning transmission electron microscopy. Ex situ images of the topography of the films were taken with Nanoscope IV Scanning Force Microscope operating in tapping mode.

The spatial distribution and size of the gold nanoparticles within the homopolymer films were analyzed with a JEOL 2010F transmission electron microscope operating at an accelerating voltage of 200kV in scanning mode (STEM) using a high - angle annular dark-field (HAADF) detector. The signal from the detector forms an image that is composed primarily by electrons scattered to high angles, which are associated with electron interactions close to the atomic nucleus. In such cases, the cross-section for scattering approaches the unscreened Rutherford cross-section, which is proportional to square of the atomic number, Z^2. Thus, contrast in the image is given mostly by the average atomic number[32]; this is the reason why this technique is often referred to as Z-contrast. Variations in sample density and thickness/mass can also provide noticeable contrast[33] (the HAADF signal varies as $\rho h Z^{3/2}$, where ρ is density and h is specimen thickness), making this technique ideal for imaging our nanocomposite samples, since we can clearly determine the metallic particle size distribution and shape characteristics while monitoring possible changes in film thickness due for example, to beam damage or dewetting. The technique also has the advantages of allowing the imaging of thicker samples, with a less damaging effect on the specimen in comparison to TEM because the beam is being scanned[34].

Images for particle size measurement were acquired in at least three different regions of the sample. The images were then threshold and treated with several digital filters using Clemex Vision image analysis software v2.2 (Clemex Technologies, Inc.) as well as Image J software. On average, 1400 particles were measured for determination of the particle size distribution at each annealing period. The average radius per particle $\langle R(t) \rangle$ (obtained from the projected, planar, surface area of the particles, S, assuming $R(t)=(S(t)/\pi)^{1/2}$), the fractional surface area covered by the particles, $\phi(t)$, the shape factor, S_f (defined such that $S_f = 4\pi S/P$, where P is the perimeter of the particle), and the number of particles per unit area, N(t), were calculated at various stages during the coarsening of the particles.

Dynamic secondary ion mass spectrometry (DSIMS) was used to obtain the depth profile of Au within the PMMA films. Prior to the analysis, the thickness of the film was measured using spectroscopic ellipsometry (J.A. Wollam Co., Inc.). SIMS was performed at UCSB with a Physical Electronics 6650 Quadropole secondary ion microscope. Sputtering was accomplished with the use of a cesium primary ion beam monitoring negative secondary ions. The negative carbon and silicon secondary ion currents were measured to monitor the stability of the profile, and to serve as indicators of the polymer-air and polymer-substrate interfaces. These profiles, along with the previously determined film thickness, allowed us to convert the sputtering time to a depth scale. Since in these studies we are not concerned about the absolute gold concentration, the Au^- signal was scaled to yield a maximum value of 1 and a minimum value of 0.

4.3. RESULTS

Z-contrast images of the as-cast PMMA/Au nanocomposite films are presented in figure 4.1a and 4.1c. The gold nanoparticles initially form self-organized, two-dimensional networks. The 2-D Fourier transform power spectra included as insets confirm hexagonal symmetry. The measured edge-to-edge distance is 1.9 nm, revealing interdigitation of the alkyl chains given that the length of a dodecane chain is calculated to be 1.77 nm[35]. Higher magnification images (Fig. S1) of these films indicate that the brighter regions observed are domains of nanoparticle bilayers, which cover approximately 5% of the film surface after spin-coating.

The relative concentration of gold ions as a function of distance from the free surface (Fig S2 (a)), from DSIMS analysis of a PMMA/Au nanocomposite film, reveals that the nanocrystals are segregated and reside at the free surface of the polymer film. Evidence of this interfacial segregation is also observed in the SFM image of the as-cast films which present and relatively large RMS roughness (1.9 nm) with features of depth comparable to the size of the nanoparticles(Fig S2 (b)). Computational models of diblock copolymer/nanoparticle mixtures confined between walls have shown that it is possible to induce a depletion attraction between particles and walls, wherein a fraction of the particles are pushed to the film interfaces to maximize the conformational entropy of the polymer chains([36]). In our case, the colloidal nanocrystals may be segregated exclusively at the free surface due to the relatively low surface tension of the dodecanethiol ligands ($\gamma_{DT\text{-}Air}$, = 25.4 mJ/m^2) with respect to that of PMMA (γ_{PMMAr} = 40.2 mJ/m^2). This is better understood by considering that the adsorption energy of a particle at an interface[37, 38] is given by Ea -= $\pi R_{eff}^2 \gamma_{PMMA}(1-|\cos\theta|)^2$, where $\cos\theta = (\gamma_{DT} - \gamma_{DT\text{-}PMMA})/\gamma_{PMMA}$, and R_{eff} is the radius of the coated particle (gold core radius plus brush thickness). The particle is most strongly held at the interface when $\cos\theta$ =1. Here, $\gamma_{DT\text{-}PMMA}$ = 5.2 mJ/m^2 and $R \approx 4.1$ nm, which yields Ea >> 10kT. In other words, the energy required to remove a particle from the free surface of the film is large compared to the thermal energy and thus the particles are expected to be bound at this interface.

Parenthetically, it is interesting to note that the dynamics of the organization of nanoparticles has been examined by a number of authors[39-41], specifically in controlled drying of particle solution systems onto solid substrates. However, to our knowledge, the formation of self-assembled monolayers of nanoparticles on polymer surfaces through rapid evaporation (spin-coating) of polymer/nanoparticle solutions has never been demonstrated and requires further study. Ultimately, a clear understanding of the dynamics of nanoparticle formation on the polymer matrix would be desirable to produce transferable self-assembled nanocrystalline monolayers with improved long-range order.

After annealing one of the nanocomposite films in vacuum at 150°C for a period of 1920 min, it is evident even from the low magnification image presented in figure 4.1b, that the particles have coarsened considerably, and that all order in the particle array has been lost (see inset Fig. 1b). On the other hand, the nanoparticles in the sample annealed in CO_2 at 50°C and 100 bar for a slightly longer period of time (2040 min) still seem to posses some crystalline order (Fig. 1d), while coarsening of the particles is not obvious from this image. However, the rearrangement of the monolayer[42] to form particle-void regions suggests that there is nanoparticle diffusion along the surface of the polymer film. It is noteworthy that the formation of these particle-depleted regions in the polymer surface is accompanied by an increase in the area of the bilayer domains. This seems to suggest that the particles are not as strongly adsorbed at the free surface in CO_2 environments as they are in air. In fact, the interfacial tension between PMMA and CO_2 is lowered considerably at the experimental conditions[43] ($\gamma_{PMMA\text{-}CO2} \approx 9$ mJ/m^2),. Such a drastic reduction in the surface energy of the polymer would make it energetically favorable to expose more PMMA to the free surface in order to increase nanoparticle-nanoparticle contacts by expanding bilayer domains.

Higher magnification HAADF images of both the vacuum (Fig. 2a) and CO_2 annealed (Fig. 3a) nanocomposite films show more clearly the progression of particle size with annealing time. Measurements of the size of the particles demonstrate nearly a 3-fold increase in the diameter of the gold cores after 1920 min of annealing in vacuum environments, accompanied by an increase in the polydispersity of the particle size ($\sigma/\langle R\rangle_{t=1920min} \sim 44\%$.). From the Z-contrast images, it is also clear that particles become more irregular at long times (t = 5700 min). This statement becomes evident when examining the plot of the average shape factor, S_f, versus time (circles in figure 4.4a), which provides a measure of the relative circularity of planar shapes($S_f = 1$ for a circle). The value of S_f remains relatively constant and close to 1 for $t \leq 480$ min, and decreases considerably in the last two experimental measurements.

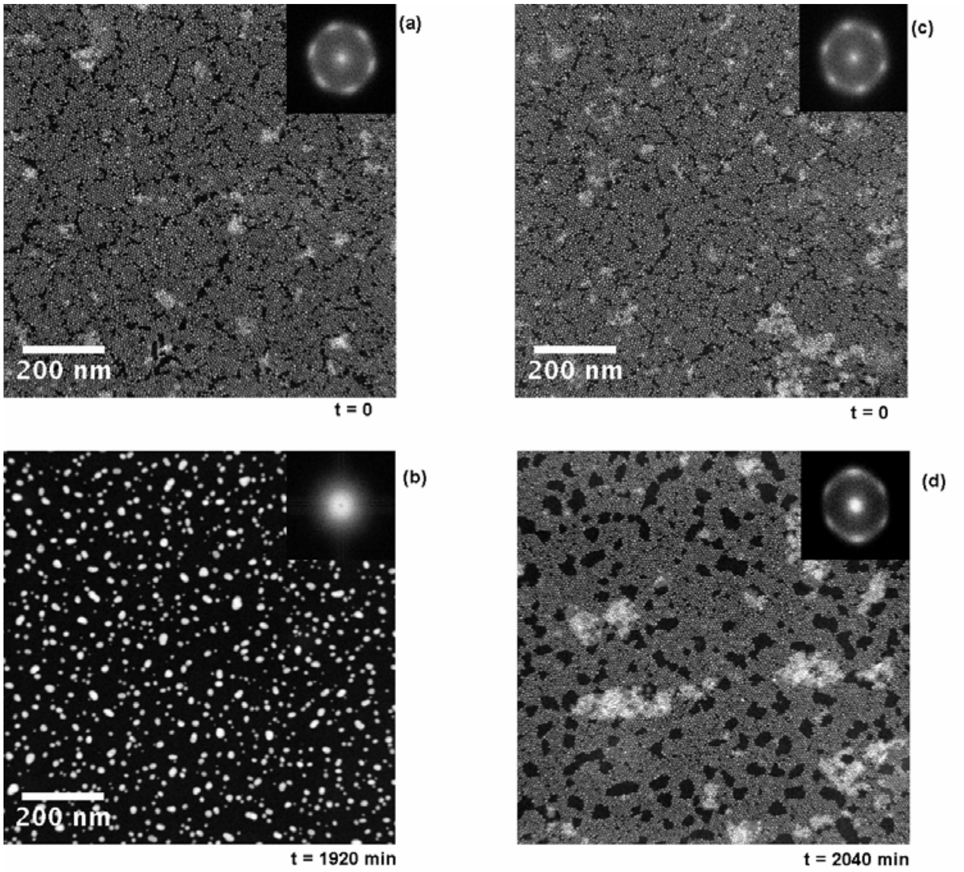

Figure 4.1. HAADF images illustrating the morphologies of PMMA/gold nanoparticle nanocomposite films. The as-cast films, images **(a)** and **(c),** present self-assembled two-dimensional networks of Au nanocrystals, with some nanoparticle bilayer domains (brighter regions). The 2-D Fourier power spectra included as insets confirm hexagonal symmetry in the lattices. **(b)** The image depicts coarsening of the gold nanoparticles after annealing the film in vacuum environments at T = 150°C. The power spectrum demonstrates loss of order in the nanoparticle array. **(d)** Hexagonal symmetry is still present in the nanoparticle array when the film is annealed in $scCO_2$ at T = 50°C and P = 10MPa. Particle void domains are formed in the lattice.

Particle coarsening in the vacuum sample is perhaps better captured in the broadening of the distribution of particle sizes to larger values of R(t), the particle radius, with increasing time, shown in the frequency histogram of figure 4.2b. In contrast, the particles in the film annealed in CO_2 remain virtually intact after 2000 min, as exhibited by the nearly constant distribution of particle sizes shown in figure 4.3b. It is important to note that only monolayer domains were considered in the size measurements, since particle perimeter is harder to distinguish in the superimposed particles of the bilayers domains. As expected, the shape factor in this sample remains constant throughout the time of the experiment (squares in figure 4.4a).

To gain insight into the mechanism of coarsening of the gold nanoparticles in the films, we examined the time dependencies of <R(t)> and N(t). In the case of the sample annealed in vacuum environments, both quantities seem to exhibit a power-law dependence on time (black circles in figure 4.4b and its inset), showing that the growth of gold cores with annealing time, as described by <R(t)>, is naturally accompanied by a decrease in the number of particles present in the film. The value of the power-law exponent for the former is 0.192 while the latter is -0.627.

Conservation of mass defines the relationship between N(t) and <R(t)>. Assuming that the characteristic length R scales as $m^{1/D}$, where m is the mass of the aggregate and D is its fractal dimension (equal to 3 for the compact, approximately spherical clusters obtained after shape relaxation), then $\langle R(t)\rangle^3 N(t) \approx$ const., as confirmed from their time-dependence. Thus, the coarsening exponent, β, is given by: $\langle R(t)\rangle \propto t^{\beta}$ and $N(t) \propto t^{-3\beta}$. Figure 4.4b also presents measurements of these quantities for the CO_2 annealed sample to further prove that no coarsening is present in this film.

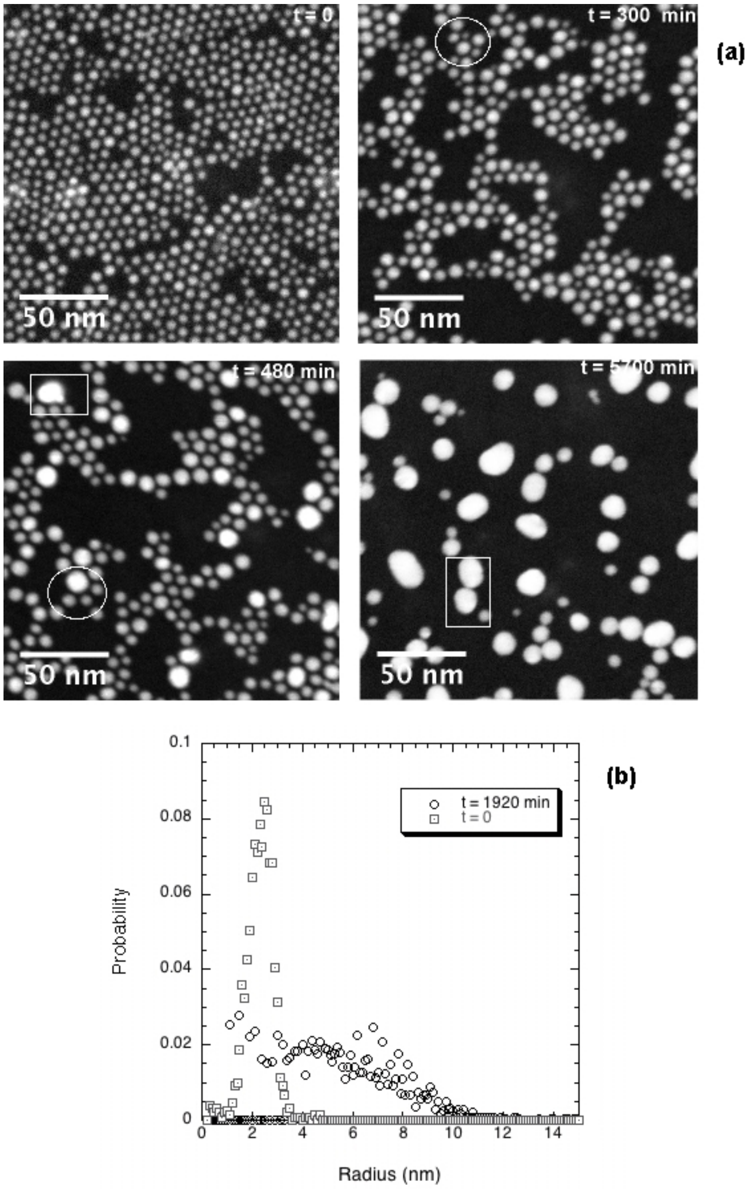

Figure 4.2. (a) The evolution of particle size within the film processed in vacuum environments (T = 150°C) is shown in the HAADF images at four different annealing times. (b) The coarsening of the nanoparticles is captured in the broadening of (non-normalized) distribution of nanoparticle sizes with time.

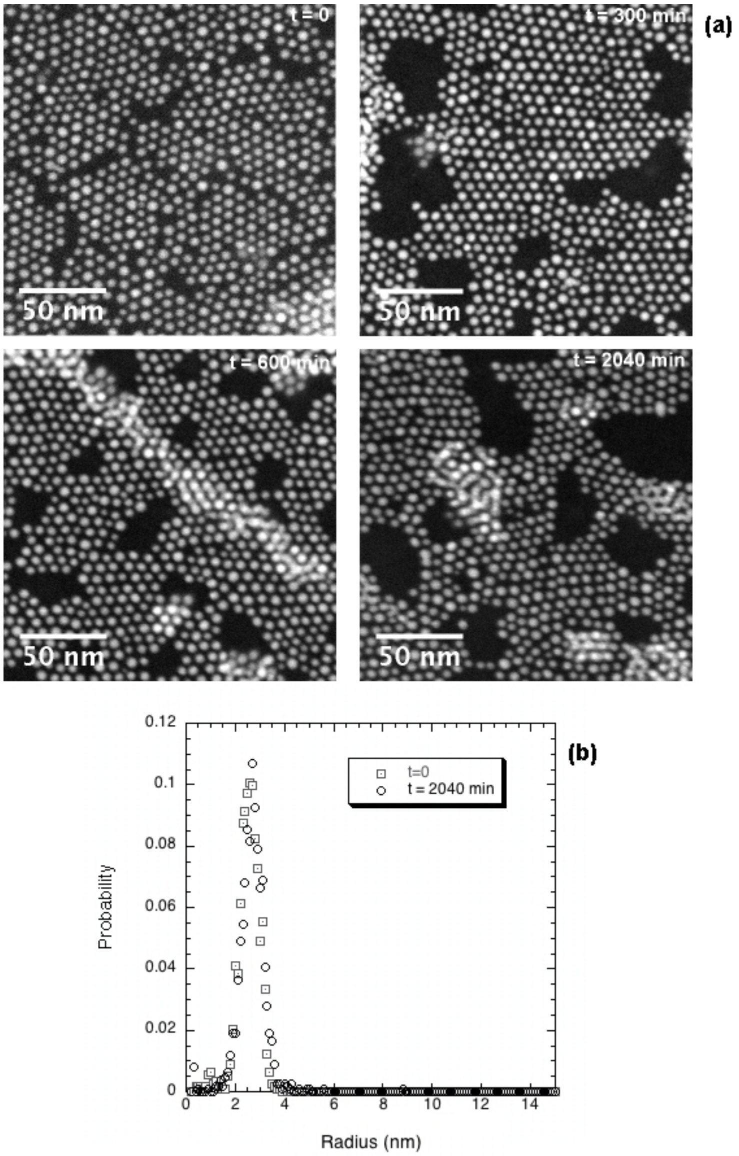

Figure 4.3 (a) HAADF images of the nanocomposite film processed in $scCO_2$ environments (T = 50°C, P = 10MPa) at four different times. (b) The size distribution of nanoparticles shown here remains constant after 2040 min of annealing, with respect to t = 0.

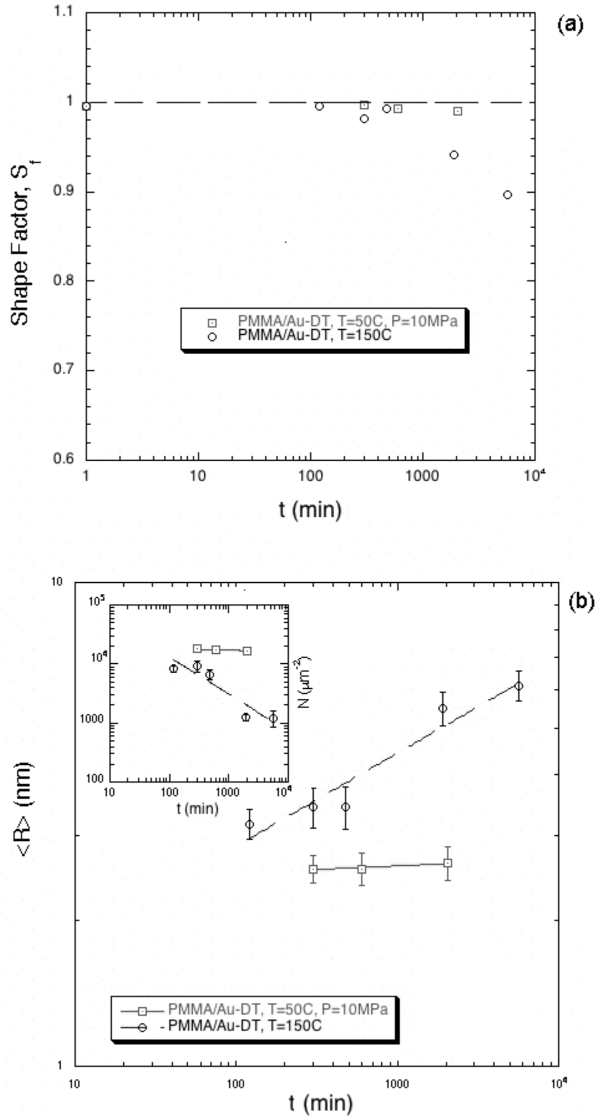

Figure 4.4 (a) The time dependence of the shape factor, Sf, for the vacuum and scCO2 processed samples is shown here. (b) Time dependencies of <R> and N(t) exhibit power-law behavior for the film annealed in vacuum environments (circles), <R> ∝tβ and N∝t-3β, where the coarsening exponent is approximately β = 1/5. <R> and N(t) remain approximately constant throughout the annealing period when the nanocomposite is annealed in scCO2 environments (squares).

As expected, the values of <R(t)> and N(t) remain constant throughout the annealing period (gray squares).

In the next section, we will review some of the basic assumptions and distinctive features, such as the growth kinetics and the characteristic size distribution functions, of the two predominant models of coarsening, Ostwald ripening and dynamic coalescence. We will then compare the theoretical predictions given by these two models with the data obtained for the sample processed in vacuum environments to determine the mechanism that engenders growth of the gold nanoparticles in the nanocomposite. Finally, we will discuss qualitatively the influence that temperature and CO_2 plasticization have on the stability of the particles in the nanocomposite annealed in $scCO_2$

4.4 DISCUSSION

4.4.1 Coarsening models

As mentioned above, one of the most widely studied mechanisms used to describe late-stage coarsening in dispersed two-phase systems is Ostwald ripening[23, 44-49] (OR). This mechanism describes low-coverage systems with stationary clusters that can exchange mass through detachment and migration of atoms (or molecules) across the diffusion field. OR is a competitive growth process governed by the Gibbs-Thompson effect, which states that the chemical potential of a cluster is inversely proportional to its radius of curvature. The difference in chemical potentials between clusters of different sizes leads to growth of large clusters at the expense of small ones, thereby reducing the total surface to volume ratio of the system[46, 48, 49].

Formulation of a mean-field theory of ripening by Lifshitz, Slyozov[50], and Wagner[51] (LSW theory) for three-dimensional clusters in a matrix (3D/3D systems) and its subsequent extension for 2D/2D systems by Marquesee[52] (islands on a substrate), has led to a cluster growth law as a function of time and a cluster size distribution function. It has been found that at long times, the average cluster radius obeys the scaling relation $<R(t)> \sim t^{\beta}$. For dimensionally homogenous systems, i.e. 2D/2D and 3D/3D systems, the value of $\beta = ½$ when the rate limiting step for transport is associated with detachment of atoms, while $\beta = 1/3$ when transport is limited by surface diffusion of the species[44, 46]. For 3D particles in a 2D diffusion field, a divergence in the steady state solution of the two-dimensional diffusion equation complicates the analysis[53]. However, an asymptotic growth exponent $\beta = ¼$ has been found when transport is determined by diffusion. On the other hand, for interface-limited mass transport in 3D/2D systems it was found that $\beta = 1/3$[23]. The scaling properties of the ripening process at long time also result in a cluster size distribution function, F(R,t), which has a scale invariant form, F(R/<R>). This cluster size distribution function is a normalized probability distribution that defines the number of clusters of each size in a fixed volume (or area) as a function of time.

For 3D/3D systems, F(R/<R>) is given by equation (1) when coarsening is interface driven[49],

$$F(R') = \begin{Bmatrix} \dfrac{CR'\exp\left(\dfrac{-3R'}{2-R'}\right)}{(2-R')^{5}} & if\ R' < 2 \\ 0 & if\ R' > 2 \end{Bmatrix} \qquad (1),$$

where R′ = R/<R> and C is a normalization constant. When the rate determining step is diffusion of atoms, *F*(R’) is given by[45] :

$$F(R') = \begin{Bmatrix} \dfrac{4R'^{2}}{9}\left(\dfrac{3}{3+R'}\right)^{7/3}\left(\dfrac{-3/2}{R'-3/2}\right)^{11/3}\exp\left(\dfrac{R'}{R'-3/2}\right) & if\ R' < 3/2 \\ 0 & if\ R' > 3/2 \end{Bmatrix} \qquad (2).$$

These distribution functions, plotted against R′ in figure 4.5, yield negatively skewed curves, with tails that extend to zero as R′ approaches zero. The maxima in the functions define a critical cluster size below which clusters shrink in size.

Let us now consider another mechanism of coarsening, in which clusters are allowed to diffuse, collide and coalesce to increase the mean cluster size. The kinetics of coarsening through coalescence were first studied by von Smoluchowski[54], under the assumption that collisions between clusters are binary (valid for low coverages) and that concentration fluctuations are negligible resulting in a mean-field rate equation. The kinetic equation that describes the collision of an i-mer with a j-mer to form a k-mer is essentially the equation of an irreversible second-order chemical reaction. Thus, the rate of formation of the k-mer is proportional to the product of the concentration of the reacting species and a rate constant, β_{ij},

$$\frac{dn_k}{dt} = \tfrac{1}{2}\sum_{i+j=k} \beta_{i,j} n_i n_j - n_k \sum_i \beta_{i,k} n_k \qquad (3),$$

where n_k is the number of aggregates per unit volume (or area)[55-57]. The first term in the right-hand side of this population balance accounts for the formation of k-mers due to aggregation of clusters smaller than k, while the second term is the loss of these k-mers due to coalescence with clusters of all sizes. This results in a set of equations with a matrix of rate constants, or kernels, which contain the microscopic details of the collision process. Two-limiting regimes for the irreversible colloidal aggregation process have been identified and studied in the literature: rapid, diffusion-limited aggregation (DLCA), and slow, reaction-limited aggregation (RLCA)[55, 58]. Both of these models assume that clusters diffuse randomly (through Brownian motion), and that bond breakup cannot occur once an aggregate is formed. Consequently, they describe scenarios where the particles do not interact because their interparticle potential is of short range compared to their size, and where this potential has a deep primary minimum (greater than k_bT) that accounts for the irreversibility of the aggregation process. The difference between the two mechanisms is that in DLCA every collision leads to bond formation, while in RLCA this constraint is relaxed by introducing a probability that two particles attach together upon collision. The end result is that in DLCA the increase in average cluster size with time follows a power law, while in RLCA it increases exponentially in time[58, 59].

In order to gain some insight into how variables like temperature or ligand coverage may affect coalescence, a brief description of common functional forms for the collision kernel is necessary.

The simplest kernel for DLCA neglects the size dependence of the aggregation rate (by considering equally-sized particles) leading to a constant collision kernel that takes on the following form: $K_{Smol} = 8k_bT/3\mu$, when it is assumed that aggregates are spherical and that their diffusion coefficient, D_i, can be represented by the Stokes-Einstein relation[60].

A more general approach allows for clusters of different sizes and assumes that the $D_i \propto i^{\alpha}$. The kinetic parameter, α, has a negative value, illustrating the fact that larger clusters should diffuse more slowly than smaller ones. If the aggregates diffuse in d dimensions, the result is a kernel, $B_{ij} = (i^{\alpha} + j^{\alpha})(i^{1/D} + i^{1/D})^{d-2}$, which takes into account the rate of transport (first factor) and the collision cross-section of the aggregates (second factor). Thus, the total kernel for DLCA is $\beta_{ij} = ¼K_{Smol}B_{i,j}$. It can be demonstrated[55, 56, 61] that this kernel is homogeneous, i.e. it scales with i and j as in equation (4).

$$\beta_{\lambda i,,\lambda j} = \lambda^{2\omega}\beta_{ij}, \qquad (4),$$

with a homogeneity exponent $2\omega = \alpha + (d-2)/D$.

Villarica[56] and Jullien[61] have shown that when the kernel is homogeneous and time independent as in equation (4), it is possible to obtain an asymptotic solution for the population balance presented in Eqn. (3)). This solution can be related to a normalized scale-invariant cluster distribution function written in terms of the radii of the aggregates, F(R'=R/<R>). For 3-dimensional clusters diffusing in 3 dimensions the long-time distribution function should take the following form:

$$F(R') = \frac{3W(R'W)^{-3\alpha+1} e^{-(WR')^3}}{\Gamma(-\alpha + 2/3)} \qquad (5)$$

where $W = \dfrac{\Gamma(-\alpha+1)}{\Gamma(-\alpha+2/3)}$.

This is a log-normal shape size distribution that is positively skewed, with the longer tail extending toward large cluster sizes, as shown in figure 4.5. The long-time solution is also consistent with the expected power-law scaling behavior of the average particle size, $\langle R \rangle \sim t^{\beta}$, with $\beta = 1/[2 - 3\alpha]$. It is worth mentioning that for RLCA the kernel can be modified to account for the reduced 'sticking' efficiency of the particles due to the presence of repulsive interactions, such as the steric interactions generated by the presence of ligands, by including the stability ratio, W[59, 60, 62, 63]. The stability ratio is defined as the ratio of the diffusion-limited aggregation rate to the reaction-limited aggregation rate of the primary particles, that is, 1/W is the fraction of collisions between particles that lead to aggregation. Theoretically W can be determined from the area under a plot of the interaction potential between two approaching particles against separation, V(h). Thus, if one assumes that the reactivity of the aggregates does not depend on mass, the collision kernel for RLCA can be represented as $K_{ij} = K_{Smol}B_{i,j}W^{-1}$.

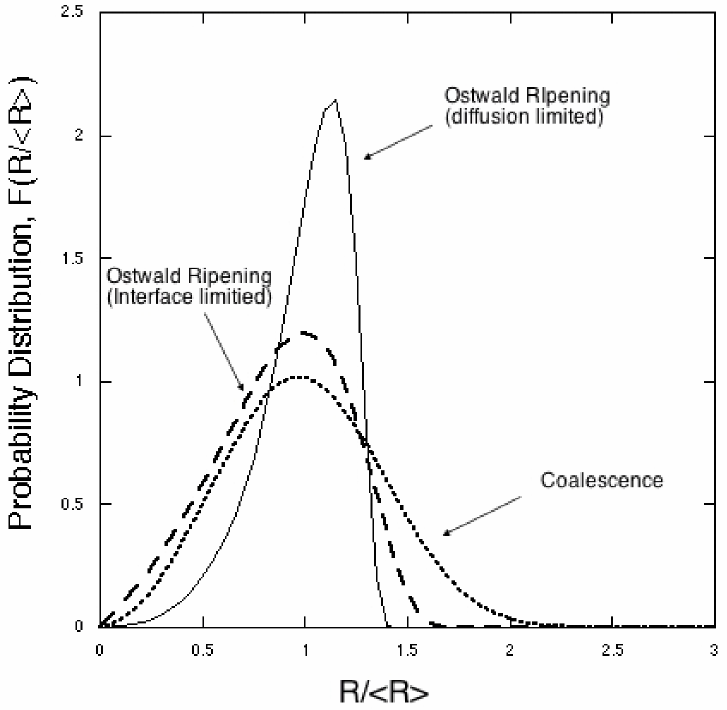

Figure 4.5 A comparison of the theoretical probability distribution functions, F(R/<R>) versus R/<R>. The solid line shows the distribution for diffusion limited OR, the dashed line is interface limited OR, and the dotted line is the coalescence distribution based on the Smoluchowski equation with $\alpha = -0.1$.

A final consideration that can be relevant for surface-protected particles is the possibility of reversible aggregation. In this case, the steric barrier (of thickness δ) generated by the ligands leads to a reduction in the depth of the minimum in the interaction potential, which in turn causes deaggregation of particles. Ordiozola[64] et al. addressed this problem by adding two terms that account for the deaggregation rate of k-mers in equation (3), each with its corresponding fragmentation kernel, f_{ij}.

In the next section, we will analyze the coarsening exponents as well as the nanoparticle size distribution function of the vacuum-annealed nanocomposite in view of the mechanisms of coarsening described above.

4.4.2 Coarsening in vacuum annealed sample

Let us begin by considering the coarsening exponent of the vacuum-annealed sample obtained from figure 4.4b. The value of $\beta \sim 1/5$ would seem to suggest that the coarsening process is not capillarity driven, since it is smaller than what is expected from the Ostwald ripening exponents discusses above, regardless of the rate-limiting step or of the dimensionality of the diffusion field and the dispersed particles. Consequently, based on the coarsening exponent alone, one would have to conclude that the main mechanism of coarsening is coalescence and that furthermore, the kinetics of aggregation are determined by diffusion of the particles through the matrix (DLCA). This is implied in the power-law behavior of the average cluster size with time characteristic of the DLCA regime, as opposed to the exponential behavior of $<R(t)>$ vs. t expected in the reaction-limited regime (RLCA). Nevertheless, as mentioned earlier, knowledge of the coarsening exponent is often not sufficient to determine the coarsening mechanism. More conclusive evidence can be obtained by relying on the shape and the time-dependence of the normalized probability distribution function.

The cluster size frequency distribution at each time was normalized to obtain the function F(R/<R>) plotted vs. R/<R> in figure 4.6. Interestingly, all the data did not collapse onto a single curve, as expected for a self-similar coarsening process. Indeed, in the initial stages of the coarsening process (t ~ 120-480 min) the normalized distribution functions are relatively narrow and symmetric, closely resembling the size distribution of the nanoparticles right after synthesis i.e., before annealing at 150°C(t = 0). On the other hand, the last two probability distributions (t =1920 min and t = 5700 min) collapse perfectly onto a single curve having a log-normal shape that is positively skewed. Moreover, the non-logarithmic plot of <R> vs. t (Fig. 7a) shows that the coarsening kinetics of the particles can be divided into two distinct growth stages having a discontinuity at ~ 480 min. In the following, we will examine both of these regimes separately.

Before we analyze the first regime we will consider the normalized size distribution of the gold particles at t = 0, which should reflect the late stages of nanocrystal growth during synthesis, that is, once formation of new nuclei has ceased. The experimental particle distribution shows best agreement with the diffusion-controlled OR equation, Eq. (2), with a calculated R-squared error $R^2 = 0.95$ (Fig. 8a). However, some of the features of the experimental curve, such as the slight tail extending to larger cluster sizes and the height of the maximum, are better captured by the analytical solution to the Smoluchowski equation, Eq. (5) ($R^2 = 0.93$, $\alpha = -1.75$). Thus, one could speculate that this distribution is the result of simultaneous coalescence and ripening-based growth. Friedlander[65] and coworkers made a theoretical study of the behavior of particle size distributions with simultaneous coalescence and diffusion-controlled condensation (that is, the deposition of free atoms/molecules onto existing nuclei with transport-limited growth). They show that the relative contributions of coalescence and condensation can be obtained from the moments of the nanocrystal size distribution, $\mu_1 = R_3/R_h$ and $\mu_3 = \langle R\rangle/R_3$, where $\langle R\rangle$ is the arithmetic mean radius, $\langle R\rangle = \Sigma R_i/n$, R_3 is the cube-mean radius, $R_3 = (\Sigma R_i^3/n)^{1/3}$, and R_h is the harmonic mean radius, $R_h = n/\Sigma(1/R_i)$. Both moments are unity for monodisperse particles obtained by condensation, while for $\mu_1 > 1.25$ and $\mu_3 < 0.905$ growth occurs only through coalescence[65]. If $1 < \mu_1 < 1.25$ and $1 > \mu_3 > 0.905$, coarsening is achieved by a combination of both mechanisms. For the as-cast sample, the moments of the particle size distribution were $\mu_1 = 1.168$ and $\mu_3 = 0.952$, indicating that both condensation and coalescence play a role in the late-stage growth of the particles during synthesis (Fig. 7b). It is important to note that the model in this study neglects the Gibbs-Thomson effect when considering the partial pressure driving force for condensation.

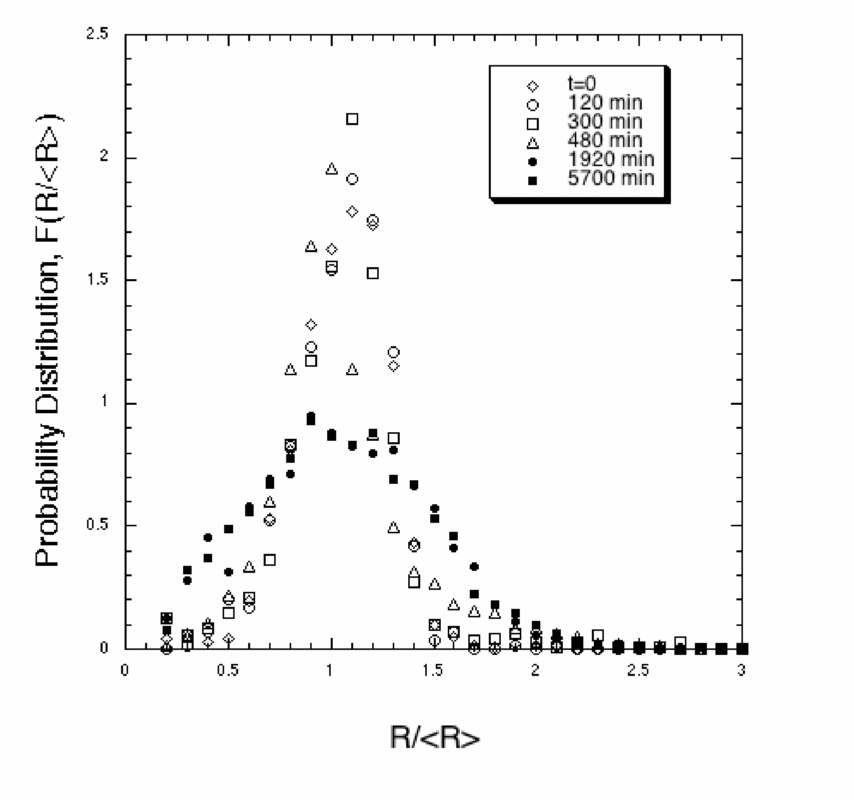

Figure 4.6 Normalized probability distribution functions for the system annealed at T = 150°C at five different annealing times. The initial normalized size distribution, t = 0, is included in the plot as a reference. The distributions for the last two annealing times, t = 1920 and t = 5700min, collapse onto a single curve.

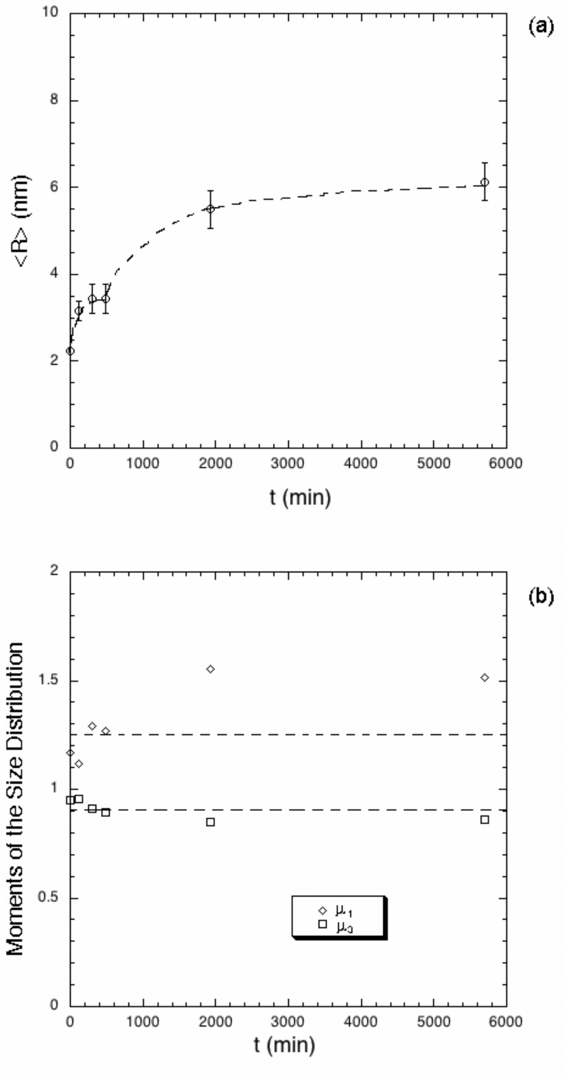

Figure 4.7 **(a)** The kinetics of nanoparticle growth due to thermal treatment (T = 150°C) are shown here in a linear plot of <R> versus t. The curve presents a discontinuity at ~500 min, suggesting the existence of two coarsening regimes. The dashed line is a guide to the eye. **(b)** The first, and third moments of the particle size distribution function, μ_1 (diamonds) and μ_3 (squares), gradually diverge from unity as the polydispersity of particles in the vacuum annealed nanocomposite grows.

As the polymer nanocomposite film is annealed, particle dimensions increase in size (as the number of particles decreases) and the moments of the distribution diverge gradually away from unity (Fig.7b) due to an increase in the polydispersity of the nanocrystals ($\sigma/\langle R\rangle_{t=480\min} \sim 30\%$). A close survey of the HAADF images of figure 4.2a gives evidence of growth by OR in the initial stages. At t = 300 min, particles retain the very smooth, spherical shape typical of growth by ripening[17], often seeing small particles ($R_i \ll \langle R\rangle$) close to big ones ($R_i \gg \langle R\rangle$), as exemplified by the circular region highlighted in the corresponding HAADF image. After 3 more hours of annealing, at $t \approx 480$ min, we can clearly distinguish merging particles in the image (square regions), even though most particles are not in contact with each other and retain their spherical shape (circular region). This suggests that in this initial stage, growth occurs by simultaneous OR and coalescence, and that coalescence may become more predominant with annealing time. The last statement is consistent with the increasing polydispersity of the particles with time, characteristic of coalescence-based growth[66].

Let us now examine the mechanism of coarsening in the late stages of growth, when t > 480 min. The HAADF image corresponding to t = 5700 min in figure 4.2a shows clusters of irregular shape in direct contact with each other, revealing the predominance of coalescence events at later times. As mentioned earlier, in this stage of growth the two normalized distribution functions collapse onto a single curve, manifesting the existence of a self-preserving distribution at long times. Not surprisingly, the line that fits our data best was calculated based on the Smoluchowski solution with $\alpha = -0.1$ and $R^2 = 0.98$ (Fig. 8b). The small magnitude of the diffusion scaling exponent, α, indicates a weak dependence of the cluster diffusion coefficient with mass, but its negative value is still consistent with the notion that small particles should diffuse more rapidly than larger ones. This weak dependence of D_i with mass is perhaps necessary for the large particles characteristic of this long-time regime to diffuse across the polymeric matrix and coalesce. From the asymptotic solution of the Smoluchowski equation given in Eqn. (5) one also obtains the relation between α and β ($\beta = 1/[2 - 3\alpha]$), yielding a value of $\beta = 0.43$. In principle, this value should be equal to the one obtained from the power-law exponent of <R> vs. t at long times. However, we only have a couple of experimental data points in this region and it is therefore impossible to compare the fit of the analytical solution to an experimental exponent. It is interesting to note that at t = 480 min the criteria $\mu_1 > 1.25$ and $\mu_3 < 0.905$ is met, supporting the theory that growth occurs exclusively through coalescence for t > 480 min (Fig. 7b). However, we must emphasize the fact that Friedlander's model is considering a condensation process where the driving force is supersaturation and not the difference in chemical potential between large and small clusters and is therefore not strictly applicable to our system,

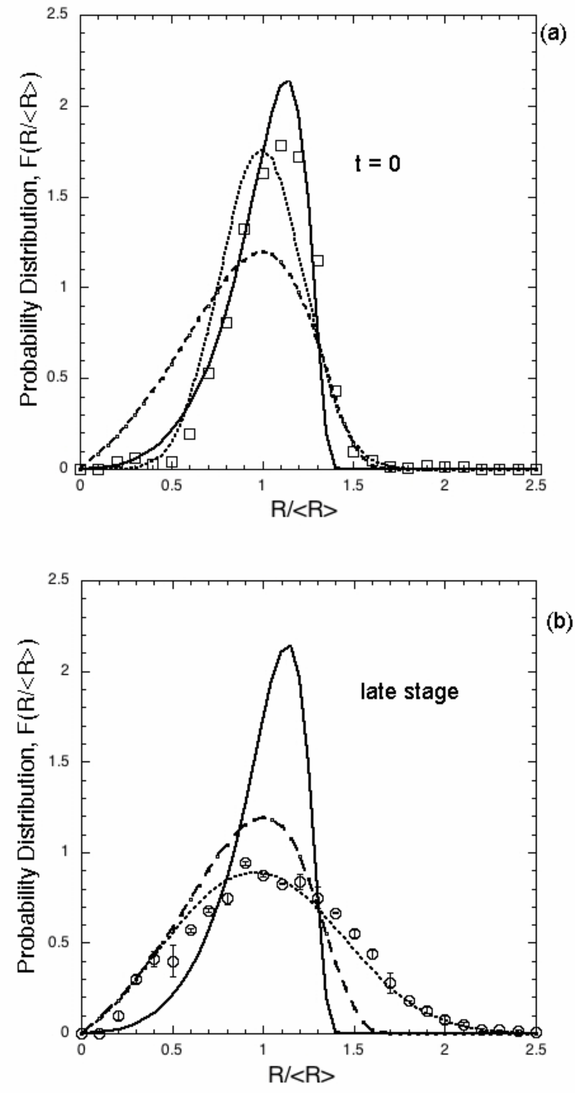

Figure 4.8 Comparison of the theoretical and experimental normalized distribution functions. The solid and the broken lines represent the distributions characteristic of OR, and the dotted line is the Smoluchowski distribution with α = -1.75 and α = -0.1 for **(a)** and **(b),** respectively. **(a)** The size distribution of the particles at t = 0 reflects the late stages of particle growth during synthesis. **(b)** The average size distribution of the nanoparticles at long times (t = 1920 min and t = 5700min) for the vacuum annealed film (T = 150°C).

Thus far, we have not explained the reason for the two stages of kinetic growth described above. We postulate that the transition from combined OR/coalescence-based growth to pure coalescence-based growth is mainly related to the complete thermal desorption of the dodecanethiol ligands from the gold metal cores. At the beginning of the annealing process, particles are protected from aggregation and fusion by a layer of ligands that cover the gold core surface completely. As a general guideline, metallic cores are able to fuse if they approach to within 0.5 nm (δ_c) of each other[67]. From the HAADF images of the film at the earlier annealing times, the interparticle separation distance, δ, was measured to be ~1.9 nm. Therefore, at this point particles are not able to come into close enough contact to coalesce. On the other hand, atomic diffusion of gold atoms should be somewhat restricted by the presence of the dodecanthiol molecules, and growth through OR will also be inhibited. In the course of the heating process, however, the ligands will gradually desorb[68] and particles will be only partially passivated. Diffusion of free atoms and small oligomers that are no longer bound by ligands will promote growth by OR. As dodecanethiol desorption continues, the partially pasivated particles will have an increasing probability of coming within δ_c upon collision and fuse. Thus, a competition between OR and coalescence will be established. When most ligands have been thermally desorbed every collision will lead to irreversible aggregation, and rapid coalescence will then dominate the growth of particles. We find evidence that total thermal desorption in our nanocomposite film occured after 480 min, since in the HAADF image corresponding to this annealing time we are still able to see many particles separated by a distance close to δ, the thickness of the steric barrier at $t = 0$.

To corroborate this hypothesis, we would need information about the ligand desorption rate in our particular system, which is difficult to obtain. Nevertheless, some analogies can be drawn with studies of the structural transformation of the Au(111) surface (with monolayer-high islands) covered by a self-assembled monolayer (SAM) of dodecanethiol molecules in vacuum from room temperature to the desorption temperature[68]. They show that at room temperature atomic diffusion is completely inhibited by the thiol molecule, but as temperature increases to ~90°C, the gold islands start growing through Ostwald ripening. Upon a further increase in temperature (~125 °C), rapid island growth was found to accompany the desorption of thiol molecules. Events of island-terrace fusion were often observed in the STM images, strongly suggesting the existence of growth by coalescence.

Further insight would be gained by understanding the influence of the ligand surface coverage on the interaction energy between colloidal particles, using the DLVO theory as the basis for studying the colloidal stability[69]. This would require not only an estimate of the van der Waals attractive interaction between gold spherical particles in a PMMA matrix (which can be easily approximated using the microscopic approach of London-Hamaker), but also knowledge of the steric (elastic and osmotic contributions) and depletion interactions of the passivated particles in the polymer melt, where the ligand and the free polymer are incompatible ($\chi_{\text{DT-PMMA}} > 0$). While the literature reports analytical expression for the contribution of these type of interactions to the total interaction potential between particles in dilute and semi-dilute polymer solutions[70], to our knowledge such relations have not been reported for polymer melts, specifically for $\chi_{\text{ligand-polymer}} > 0$. The form of the potential would ultimately give us information about the collision efficiency (the probability that particles adhere upon collision, 1/W), as well as the reversibility of the aggregation process as a function of ligand coverage.

A more complete picture of the problem at hand would also require knowledge of the interaction between gold and PMMA to account for possible adsorption of the polymer to the gold surface once dodecanethiol has thermally desorbed, as well as the possibility of depletion interactions between the bare metallic cores in the polymer melt. The possibility of other types of interactions, like the lateral long-range attraction sometimes observed between colloidal spheres trapped at an interface[71], should also be taken into consideration since our particles were shown to reside at the air-polymer interface.

Some final considerations that may affect the analysis of the kinetics of growth of the nanoparticles in our system are related to the fact that some assumptions in our coarsening models are violated in our system. First of all, the collisions between particles are not always binary, as assumed in the coalescence model. Most importantly, the coalescence model described above is strictly valid for particles that are randomly distributed in space, which is clearly not the case for our particles at the initial stages of growth. More specifically, for the collision kernel to be independent of time, as was assumed above, the spatial distribution of the particles must also be time-independent [72]. The spatial correlation between the particles in our sample will undoubtedly have an effect on the asymptotic distribution of particle sizes.

4.4.3 CO_2 effects on coarsening

The results on the evolution of nanocomposite structure upon annealing in scCO_2 for more than 2000 minutes clearly showed that the nanocrystals remained stable toward growth during processing, while still having enough mobility to diffuse across the polymer matrix. In contrast, rapid rates of nanocrystal growth were observed for the nanocomposite annealed in vacuum environments at higher temperatures. In this section we will analyze the effects of temperature and CO_2 sorption on coalescence, and then briefly discuss the effects of temperature on OR.

The effect of $scCO_2$ annealing in the rate of coalescence of the gold nanoparticles within the PMMA matrix, as compared to that in vacuum environments, is perhaps better understood by analyzing the effect that the processing conditions have on the collision kernel. As mentioned earlier, the collision kernel for DLCA can be expressed as: $\beta_{ij} = \frac{1}{4}K_{Smol}B_{i,j}$, where $K_{Smol} = 8k_bT/3\mu$,. Thus, the most obvious consequence of processing the nanocomposite in $scCO_2$ is probably related to the low annealing temperature, and its impact on the viscosity of the polymer melt. It is necessary to assess how much the viscosity of the PMMA matrix has changed with the addition of CO_2 by first considering how much the glass transition has been depressed due to CO_2 absorption. Condo and coworkers[73, 74] have reported data for the depression of the glass transition temperature of PMMA with increasing CO_2 pressure. In figure S3 we show the T_g's measured by Condo as a function of CO_2 activity, since activities include effects of both temperature and pressure. A fit to his experimental data can then give us a rough estimate of the $T_{g\text{-}co2}$ of our polymer film at the activity that corresponds to the processing conditions of the film (at T = 50°C and P = 10 MPa, $a_{CO2} = 0.9846$ and $T_{g\text{-}co2} \sim -1°C$). From the estimated $T_{g\text{-}co2}$, we note that the sample processed in CO_2 was annealed ~ 51°C above its glass transition ($T_{exp} - T_{g\text{-}co2} = \Delta T_{g\text{-}co2} \sim 51°C$), while the sample processed in vacuum was annealed ~ 45°C above ambient T_g ($T_{exp} - T_g = \Delta T_g \sim 45°C$, where T_g was measured by Condo to be 105°C). Researchers have shown that viscosity reductions in polymer-supercritical fluid mixtures are primarily the result of an increase in free volume which causes a depression in the Tg of the polymer[75, 76]. Based on this idea, if $\Delta T_g \approx \Delta T_{g\text{-}co2}$, then to a first order approximation the viscosity of both films should be equal, and therefore viscosity should not be a factor that significantly affects the diffusion coefficient nor the collision rate of the particles at our experimental conditions. This argument has the underlying assumption that T_g for the mixture will occur at the same value of the fractional free volume as the T_g for the pure polymer. It is clear that despite the lower $scCO_2$-annealing temperature, the gold particles have enough mobility to diffuse along the surface of the polymer film forming particle-depleted regions in the monolayer (see Figure 4.1).

Having addressed how $scCO_2$ may affect the simplest form of the collision kernel, we can comment on the effect the steric barrier is expected to have on colloidal stability in the polymer matrix. The most substantial effect of using $scCO_2$ to process the nanocomposite film is probably related to the fact that at 50°C the dodecanethiol ligands are unlikely to desorb from the gold core surface, since thermal desorption of these ligands is expected to occur several tens of degrees above the annealing temperature[68]. Complete passivation of the gold core surfaces by the alkanethiols will result in interparticle separation distances that are always greater than δ_c, making the likelihood of coalescence very slim.

In the same manner that the presence of ligands affects coarsening by coalescence, it is expected that coarsening by OR will by inhibited by the presence of the thiols, which can restrict atomic diffusion at the gold core surface, specially at low temperatures[68]. Apart from the restriction on atomic mobility caused by the stability of thiol molecules at the conditions studied, temperature is expected to affect the growth rate of the OR process through its effect on interfacial energy, diffusion and growth rate coefficients, and equilibrium solubility[48]. The resulting temperature dependence of the ripening rates can change drastically depending on the properties of the system at the microstructural level, which are unfortunately difficult to evaluate for our particular system.

4.5 CONCLUSIONS

Our results demonstrate that the use of supercritical fluids as processing media for nanocomposites can be an effective means of preserving the integrity of surface-protected nanofillers, while achieving polymer chain relaxation at low temperatures. In contrast, regular thermal processing in vacuum environments is shown to cause coarsening of the nanoparticles within the polymer matrix, a phenomenon that could potentially change the properties of the nanocomposite material. Analysis of the growth kinetics, the particle size distribution function, F(R/<R>) vs R/<R>, and the spatial distribution and shape characteristics of the nanoparticles via HAADF images, shed some light into the mechanisms that lead to coarsening at different stages of the process. The distinct growth stages observed were linked to the gradual desorption of the alkanethiol molecules at the high annealing temperature. Further experiments and theoretical efforts should address this issue in greater detail.

4.6 REFERENCES

1. Bliznyuk, V.; Ruhstaller, B.; Brock, P. J.; Scherf, U.; Carter, S. A. Advanced Materials **1999,** 11, (15), 1257-+.

2. Buxton, G. A.; Lee, J. Y.; Balazs, A. C. Macromolecules **2003,** 36, (25), 9631-9637.

3. Krishnamoorti, R.; Yurekli, K. Current Opinion in Colloid & Interface Science **2001,** 6, (5-6), 464-470.

4. Krishnan, R. S.; Mackay, M. E.; Hawker, C. J.; Van Horn, B. Langmuir **2005,** 21, (13), 5770-5776.

5. Li, C. X.; Wu, J. T.; Zhao, J.; Zhao, D. L.; Fan, Q. R. European Polymer Journal **2004,** 40, (8), 1807-1814.

6. Lin, Y.; Boker, A.; He, J. B.; Sill, K.; Xiang, H. Q.; Abetz, C.; Li, X. F.; Wang, J.; Emrick, T.; Long, S.; Wang, Q.; Balazs, A.; Russell, T. P. Nature **2005,** 434, (7029), 55-59.

7. Mackay, M. E.; Dao, T. T.; Tuteja, A.; Ho, D. L.; Van Horn, B.; Kim, H. C.; Hawker, C. J. Nature Materials **2003,** 2, (11), 762-766.

8. Papakonstantopoulos, G. J.; Yoshimoto, K.; Doxastakis, M.; Nealey, P. F.; de Pablo, J. J. Physical Review E **2005,** 72, (3), -.

9. Potschke, P.; Dudkin, S. M.; Alig, I. Polymer **2003,** 44, (17), 5023-5030.

10. Starr, F. W.; Schroder, T. B.; Glotzer, S. C. Physical Review E **2001,** 6402, (2), -.

11. Sternstein, S. S.; Zhu, A. J. Macromolecules **2002,** 35, (19), 7262-7273.

12. Usuki, A.; Hasegawa, N.; Kato, M. Inorganic Polymeric Nanocomposites and Membranes **2005,** 179, 135-195.

13. Coleman, J. N.; Khan, U.; Gun'ko, Y. K. Advanced Materials **2006,** 18, (6), 689-706.

14. Ganesan, V.; Pryamitsyn, V.; Surve, M.; Narayanan, B. Journal of Chemical Physics **2006,** 124, (22), -.

15. Schmidt, G.; Malwitz, M. M. Current Opinion in Colloid & Interface Science **2003,** 8, (1), 103-108.

16. Zhang, Q.; Archer, L. A. Macromolecules **2004,** 37, (5), 1928-1936.

17. Huang, F.; Zhang, H. Z.; Banfield, J. F. Journal of Physical Chemistry B **2003,** 107, (38), 10470-10475.

18. Zhang, H. Z.; Banfield, J. F. Nano Letters **2004,** 4, (4), 713-718.

19. Mukherjee, D.; Sonwane, C. G.; Zachariah, M. R. Journal of Chemical Physics **2003,** 119, (6), 3391-3404.

20. Jeong, J. I.; Choi, M. Journal of Colloid and Interface Science **2005,** 281, (2), 351-359.

21. Siggia, E. D. Physical Review A **1979,** 20, (2), 595-605.

22. Martula, D. S.; Hasegawa, T.; Lloyd, D. R.; Bonnecaze, R. T. Journal of Colloid and Interface Science **2000,** 232, (2), 241-253.

23. Zinke-Allmang, M. Thin Solid Films **1999,** 346, (1-2), 1-68.

24. Semin, D. J.; Lo, A.; Roark, S. E.; Skodje, R. T.; Rowlen, K. L. Journal of Chemical Physics **1996,** 105, (13), 5542-5551.

25. Floro, J. A.; Sinclair, M. B.; Chason, E.; Freund, L. B.; Twesten, R. D.; Hwang, R. Q.; Lucadamo, G. A. Physical Review Letters **2000,** 84, (4), 701-704.

26. Jeffrey, C. A.; Conrad, E. H.; Feng, R.; Hupalo, M.; Kim, C.; Ryan, P. J.; Miceli, P. F.; Tringides, M. C. Physical Review Letters **2006,** 96, (10), -.

27. Leyvraz, F.; Redner, S. Physical Review Letters **2002,** 88, (6), 16830-1-4.

28. Lo, A.; Skodje, R. T. Journal of Chemical Physics **2000,** 112, (4), 1966-1974.

29. Limary, R.; Green, P. F. Physical Review E **2002,** 66, (2), -.

30. Limary, R.; Green, P. F. Langmuir **2003,** 19, (6), 2419-2424.

31. Brust, M.; Walker, M.; Bethell, D.; Schiffrin, D. J.; Whyman, R. Journal of the Chemical Society-Chemical Communications **1994**, (7), 801-802.

32. Midgley, P. A.; Weyland, M. Ultramicroscopy **2003,** 96, (3-4), 413-431.

33. Liu, J. Y. Journal of Electron Microscopy **2005,** 54, (3), 251-278.

34. Hunter, R. J., Foundation of Colloid Science. 2nd ed.; Oxford University Press: New York, 2001.

35. Pileni, M. P. Journal of Physical Chemistry B **2001,** 105, (17), 3358-3371.

36. Lee, J. Y.; Shou, Z. Y.; Balazs, A. C. Macromolecules **2003,** 36, (20), 7730-7739.

37. Chiu, J. J.; Kim, B. J.; Kramer, E. J.; Pine, D. J. Journal of the American Chemical Society **2005,** 127, (14), 5036-5037.

38. Dickson, J. L.; Binks, B. P.; Johnston, K. P. Langmuir **2004,** 20, (19), 7976-7983.

39. Bigioni, T. P.; Lin, X. M.; Nguyen, T. T.; Corwin, E. I.; Witten, T. A.; Jaeger, H. M. Nature Materials **2006,** 5, (4), 265-270.

40. Tang, J.; Ge, G. L.; Brus, L. E. Journal of Physical Chemistry B **2002,** 106, (22), 5653-5658.

41. Lin, X. M.; Jaeger, H. M.; Sorensen, C. M.; Klabunde, K. J. Journal of Physical Chemistry B **2001,** 105, (17), 3353-3357.

42. Shah, P. S.; Novick, B. J.; Hwang, H. S.; Lim, K. T.; Carbonell, R. G.; Johnston, K. P.; Korgel, B. A. Nano Letters **2003,** 3, (12), 1671-1675.

43. Otake, K.; Kobayashi, M.; Ozaki, Y.; Yoda, S.; Takebayashi, Y.; Sugeta, T.; Nakazawa, N.; Sakai, H.; Abe, M. Langmuir **2004,** 20, (15), 6182-6186.

44. Ardell, A. J. Materials Science and Engineering a-Structural Materials Properties Microstructure and Processing **1997,** 238, (1), 108-120.

45. Ardell, A. J. Journal of the European Ceramic Society **1999,** 19, (13-14), 2217-2231.

46. Carlow, G. R. Physica A **1997,** 239, (1-3), 65-77.

47. Madras, G.; McCoy, B. J. Journal of Chemical Physics **2002,** 117, (17), 8042-8049.

48. Madras, G.; McCoy, B. J. Journal of Chemical Physics **2003,** 119, (3), 1683-1693.

49. Ratke, L.; Voorhees, P. W., Growth and Coarsening: Ripeningin Material Processing. Springer: Berlin, 2002.

50. Lifshitz, I. M.; Slyozov, V. V. Journal of Physics and Chemistry of Solids **1961,** 19, (1-2), 35-50.

51. Wagner, C. Zeitschrift fuer Elektrochemie und Angewandte Physikalische Chemie **1961,** 65, 581-591.

52. Marqusee, J. A.; Ross, J. Journal of Chemical Physics **1984,** 80, (1), 536-543.

53. Shorlin, K.; Krylov, S.; Zinke-Allmang, M. Physica A **1998,** 261, 248-265.

54. Von Smoluchowski, M. Zeitschrift fur Physik **1916,** 17, 585.

55. Jullien, R. New Journal of Chemistry **1990,** 14, (3), 239-253.

56. Villarica, M.; Casey, M. J.; Goodisman, J.; Chaiken, J. Journal of Chemical Physics **1993,** 98, (6), 4610-4625.

57. Meakin, P. Physica A **1990,** 165, (1), 1-18.

58. Lin, M. Y.; Lindsay, H. M.; Weitz, D. A.; Ball, R. C.; Klein, R.; Meakin, P. Physical Review A **1990,** 41, (4), 2005-2020.

59. Runkana, V.; Somasundaran, P.; Kapur, P. C. Aiche Journal **2005,** 51, (4), 1233-1245.

60. Stechemesser, H.; Dobias, B., Coagulation and Floculation. 2nd ed.; CRC: Boca Raton, 2005; Vol. 126.

61. Botet, R.; Jullien, R. Journal of Physics a-Mathematical and General **1984,** 17, (12), 2517-2530.

62. Sandkuhler, P.; Sefcik, J.; Lattuada, M.; Wu, H.; Morbidelli, M. Aiche Journal **2003,** 49, (6), 1542-1555.

63. Shah, P. S.; Husain, S.; Johnston, K. P.; Korgel, B. A. Journal of Physical Chemistry B **2002,** 106, (47), 12178-12185.

64. Odriozola, G.; Schmitt, A.; Moncho-Jorda, A.; Callejas-Fernandez, J.; Martinez-Garcia, R.; Leone, R.; Hidalgo-Alvarez, R. Physical Review E **2002,** 65, (3), -.

65. Pich, J.; Friedlander, S. K.; Lai, F. S. Aerosol Science **1970,** 1, 115-126.

66. Madras, G.; McCoy, B. J. Journal of Colloid and Interface Science **2003,** 261, (2), 423-433.

67. Israelachvili, J. N., Intermolecular and surface forces. 2nd ed.; Academic Press: Suffolk, 1992.

68. Guo, Q.; Sun, X.; Palmer, R. E. Physical Review B **2005,** 71, (3), -.

69. Fernandez-Nieves, A.; Fernandez-Barbero, A.; Vincent, B.; de las Nieves, F. J. Langmuir **2001,** 17, (6), 1841-1846.

70. Vincent, B.; Edwards, J.; Emmett, S.; Jones, A. Colloids and Surfaces **1986,** 18, (2-4), 261-281.

71. Kralchevsky, P. A.; Nagayama, K. Langmuir **1994,** 10, (1), 23-36.

72. Sholl, D. S.; Skodje, R. T. Physica A **1996,** 231, (4), 631-647.

73. Condo, P. D.; Johnston, K. P. Macromolecules **1992,** 25, (24), 6730-6732.

74. Condo, P. D.; Paul, D. R.; Johnston, K. P. Macromolecules **1994,** 27, (2), 365-371.

75. Kwag, C.; Manke, C. W.; Gulari, E. Industrial & Engineering Chemistry Research **2001,** 40, (14), 3048-3052.

76. Royer, J. R.; DeSimone, J. M.; Khan, S. A. Journal of Polymer Science Part B-Polymer Physics **2001,** 39, (23), 3055-3066.

CHAPTER 5. Templating of Gold Nanocrystals in Micellar Cores of Block Copolymer Films.

5.1 INTRODUCTION

The development of strategies to tailor and to control the structure of block copolymers (BCP) containing nanocrystals, block copolymer nanocomposites, is an especially active area of research. The in-situ synthesis of the nanocrystals within the ordered domains, as a route to incorporate the nanoparticles within the BCP, is a common strategy.[1-7] One drawback of this approach is that control of the size, shape and ordering of the nanoparticles is limited. An alternate approach is the so-called co-assembly strategy[8-11], wherein the nanocrystals are first synthesized, enabling control of their size and shape, and subsequently compatibilized with either of the constituent blocks. With this strategy, the nanocrystals are incorporated within one phase, for example spherical micelle cores. If the particles are to occupy the continuous phase, a new copolymer would have to be synthesized. Alternatively, the structure could be manipulated with the addition of homopolymer chains to promote a transition from one phase to an adjacent phase in the phase diagram. One strategy that does not involve changing the composition of the copolymer or the nanocomposite is to induce a morphological transition via thermal or solvent treatment. To our knowledge, the possibility of changing the location of nanoparticles through a temperature-induced or a selective solvent-induced phase transition has not been realized to date.

In this paper we demonstrate that it is possible to obtain a nanostructured BCP nanocomposite thin film with a switchable spatial distribution of embedded nanoparticles between the core and the corona. Specifically, PS-b-PFOMA copolymers form a micellar film when spin cast from a toluene/freon co-solvent onto a silicon nitride substrate. The

PFOMA component forms the cores and the PS chains (coronae) form the continuous phase of the film. PS-capped gold nanocrystals are incorporated only within the continuous phase when a solution containing the copolymer, gold nanocrystals, and the co-solvent is spin cast on the substrate. Upon annealing in supercritical carbon dioxide, ($scCO_2$), the structure inverts and the PS chains subsequently constitute the core, now containing the nanocrystals, with the PFOMA chains forming a continuous (corona) phase. This procedure allows us to template single dispersed micellar cores of the BCP film containing gold nanocrystal domains. Moreover, an analysis of the distribution of gold nanoparticles across the films sheds some light into the energetic interactions that control the formation of nanostructures within them. Thus, these findings highlight important issues pertinent to the fabrication of thin film composite materials with hierarchically ordered nanoparticle arrays.

5.2 EXPERIMENTAL

5.2.1 Sample Preparation

The block copolymer studied in this work is an asymmetric polystyrene-b-poly(1,1’,2,2’-tetrahydroperfluorooctyl methacrylate) (PS-b-PFOMA), with a M_{nPS}/M_{nPFOMA} = 27,000/127,000, as determined by H NMR. The details of the synthesis performed by Lim and coworkers have been reported elsewhere[12].

The PS-b-PFOMA diblock was dissolved in an 80:20wt% mixture of 1,1,2-trichlortrifluoroethane (Freon 113) (Aldrich) and toluene (Fisher Scientific) to yield clear solutions with a polymer concentration of 0.5-2wt%. Additional solutions containing pre-synthesized gold nanoparticles stabilized with thiol-terminated polystyrene ligands (PSSH) (M_N=1000g/mol from Polymer Source Inc) were prepared.

The Au nanocrystals were synthesized by a modification of the two-phase arrested precipitation method reported by Brust et al.[13] using a 1/5 PSSH/$HAuCl_4$ ratio. The Au cores exhibited a relatively narrow size distribution with an average diameter of 4.9 ± 0.5 nm, as determined by scanning transmission electron microscopy (STEM). The weight fraction of nanoparticles in the diblock copolymer ranged from 5-10w/w%.

Films with thicknesses between 20 and 250 nm were prepared by spin-coating both the composite, and the pure BCP solutions onto glass slides. After spin-coating, the films were floated on water and off the glass substrate and deposited onto transparent silicon nitride windows (SPI supplies) to achieve film uniformity. Once prepared, the films were evacuated for a period of 12 h to remove excess solvent.

Supercritical CO_2 annealing ($scCO_2$) was performed by loading the samples into a fixed volume cell, which was subsequently sealed and pressurized with carbon dioxide (Air Products, >99.999%) using a manual pressure generator (High-Pressure Equipment Co.) and heated to the desired temperature in a water bath. The pressure was controlled with a strain gauge pressure transducer (Sensotec) calibrated to within $\pm 7\times10^{-3}$MPa. We note that at the conditions studied, 75ºC and a pressure of 13.8 MPa, both of the blocks are in a plasticized state[14-16]. After a period of 72 h, the cell was cooled to room temperature and depressurized by venting CO_2 as a vapor from the top of the cell.

For cross-sectional imaging of as-cast and CO_2 annealed samples, the nanocomposite films were spin-coated directly on silicon substrates with a silicon nitride layer of 100 nm grown by LPCVD (WaferNet, Inc.). Separation of the film from the silicon nitride substrate was realized by exposing the sample to liquid nitrogen, having both interfaces protected by an evaporated carbon layer. The films were embedded in epoxy resin (Epon) and sections of approximately 100 nm in thickness were obtained by microtoming the resin at room temperature.

5.2.2 Sample Characterization

Characterization of the films was achieved by a combination of scanning force microscopy and scanning transmission electron microscopy. Ex situ images of the topography of the films were taken with Nanoscope IV and Nanoscope IIIa (Digital Instruments) Scanning Force Microscopes operating in tapping mode.

The morphology of the diblock copolymer films, as well as the distribution of the nanoparticles within them, were analyzed with a JEOL 2010F transmission electron microscope operating at an accelerating voltage 200kV in scanning mode (STEM) using a high angle annular dark field (HAADF) detector. HAADF imaging, also called Z-contrast imaging, allows observation of the species present based on differences in atomic number, density, and sample thickness. Thus, in our pure copolymer films, contrast in the image is given by the difference in densities of the two constituent blocks, having the denser PFOMA regions ($\rho_{(20°C)}$ =1.53g/mL) appear brighter than the PS domains ($\rho_{(20°C)}$ = 1.06g/mL). In some instances, samples were exposed to the vapor of an aqueous RuO_4 solution (SPI supplies) for 5 min to selectively stain the PS-rich domains. In this case, the selectively adsorbed ruthenium compound gives a higher intensity to the PS phase, since contrast in this technique is particularly sensitive to the atomic number of the species present.

Dynamic secondary ion mass spectrometry (DSIMS) was used to obtain the depth profile of Au within the block copolymer films. The films were spin-coated directly on the silicon nitride substrates described above. Prior to the analysis, the thickness of the films was measured using spectroscopic ellipsometry (J.A. Wollam Co., Inc.). SIMS was performed at UCSB with a Physical Electronics 6650 Quadropole secondary ion microscope. Sputtering was accomplished with the use of a cesium primary ion beam monitoring negative secondary ions. The negative carbon and silicon secondary ion currents were measured to monitor the stability of the profile, and to serve as indicators of the polymer-air and polymer-substrate interfaces. These profiles, along with the previously determined film thickness, allowed us to convert the sputtering time to a depth scale. Since in these studies we are not concerned about the absolute Au concentration, the Au^- signal was scaled to yield a maximum value of 1 and a minimum value of 0.

5.3 RESULTS AND DISCUSSION

This article is organized as follows. The micellar structure of the PS-b-PFOMA diblock copolymer spin-coated from a freon/toluene solution, as well as the phase inversion of the core-shell morphology induced by $scCO_2$ annealing, are first described. Results for the sequestering of gold particles within the PS phase are then examined, followed by a discussion of the structural inversion. Two related observations are discussed, (1) the shape of the micellar structures that develop in the films after $scCO_2$ processing, (2) the influence of the proximity of interfaces on the depth-distribution of nanoparticles within the film.

5.3.1 Micelle-like Aggregate Formation and Phase Inversion of Neat PS-b-PFOMA Diblock Copolymer

The structure of the as-cast PS-b-PFOMA copolymer films produced using a toluene/freon co-solvent solution is now described. The images in Figure 5.1 indicate that PS-b-PFOMA forms micellar aggregates after spin casting; PFOMA cores of roughly 50 nm in diameter are embedded in a continuous PS (corona) matrix (see diagram in figure 5.1a). The spherical topography is evident from the SFM image of a h=22 nm thick film, shown in figure 5.1b. The PS component of the film was selectively stained with ruthenium tetroxide (RuO_4) to yield greater contrast, and imaged using STEM to obtain the Z-contrast images shown in part c. The PS component is represented by the bright regions, while the circular PFOMA cores are represented by the darker regions. Z-contrast images of a thicker (h=72 nm) as-cast PS-b-PFOMA film demonstrate the appearance of overlapping circular features, which are an indicative of the presence of two layers of micellar aggregates across the film thickness (Fig. 1d). The formation of these PFOMA-core micelles, discussed in further detail in reference 12, occurs during the spin-coating process and is a consequence of the faster evaporation rates of freon 113 relative to toluene, in which the PS chains are more soluble. It is important to emphasize that the morphology observed in these films is not in equilibrium and will be subject to further structural evolution if given the opportunity through solvent or thermal annealing.

Upon annealing the diblock in $scCO_2$, which is highly selective towards the fluorinated block,[12] the structure inverts and the PS chains now constitute the core of the micelles. An SFM scan of a 240 nm thick PS-b-PFOMA film annealed at 75°C, and a CO_2 pressure of 13.8 MPa, reveals the presence of micelles, much like those observed for the as-cast films (Fig. 2a). The Z-contrast image of the stained film (Fig. 2b) indicates that the structure of the aggregates has completely inverted in the $scCO_2$ environment to form PS cores with a surrounding PFOMA shell, as depicted in the diagram of figure 5.2c. The image in figure 5.2b also shows the existence of several layers of micelles in this thick film; on the other hand, a single layer of aggregates comprise the thinner h=70 nm film of figure 5.2d. This phase transformation opens up the possibility of controlling micelle formation and morphology by adjusting the solvent quality through manipulation of pressure and/or temperature of the system. Indeed, detailed studies on this system demonstrate that it is also possible to tune micellar size through careful adjustments of the CO_2 density[12].

We note, for the moment, that confinement of these micellar aggregates to a thin film geometry is expected to have an influence on the shape of the aggregates. For example, it is evident that the core to film thickness ratio of the as-cast sample in figure 5.1b and 5.1c demonstrates that the aggregates in this film cannot be spherical in shape and are likely to develop an ellipsoidal shape. We will discuss in more detail the effects of interfaces and confinement on the structure of the aggregates with PS cores in section 5.3.

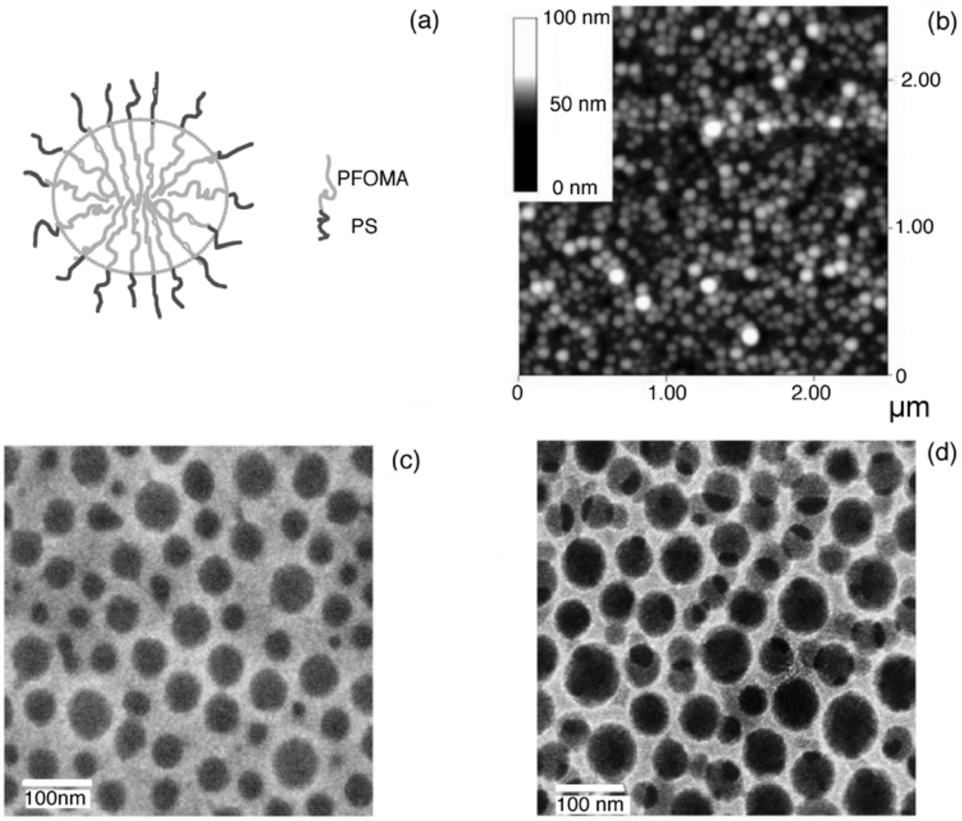

Figure 5.1 The morphology of an as-cast PS-b-PFOMA film on a silicon nitride substrate is shown here. **(a)** Schematic diagram of aggregate morphology **(b)** SFM image of the micellar aggregates in a 22 nm thick film; the average diameter of the micelles (core plus corona) is 80 nm **(c)** Corresponding Z-contrast image of the stained film with an average PFOMA core diameter of 50 nm **(d)** Z-contrast image of a stained 72nm film presenting two layers of micellar aggregates.

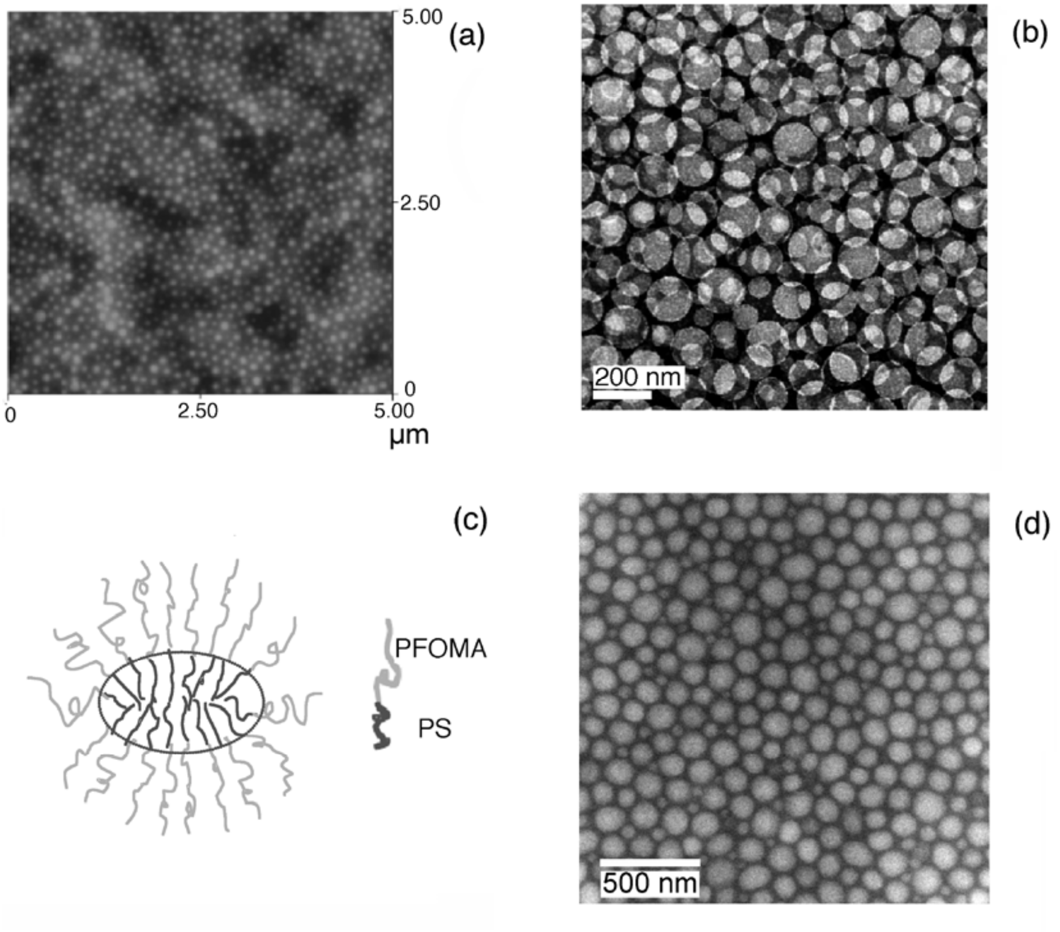

Figure 5.2 Morphology of a PS-b-PFOMA film after $scCO_2$ processing at 75°C and 13.8 MPa. (a) SFM image of a 240nm thick film annealed for a period of 72 h. **(b)** Z-contrast image of the same film stained with RuO_4, depicting the presence of several micellar layers. **(c)** Schematic drawing of the aggregate structure showing the inversion of the microdomains into PS cores. **(d)** Z-contrast image of an 70nm thick film stained with RuO_4 and presenting a single layer of micelles; the film was processed in $scCO_2$ for 10 days.

5.3.2 Phase Inversion of Sequestered Gold Nanocrystals.

The strategy for co-assembly of diblock copolymers and nanoparticles relies on tailoring the surface chemistry of the nanocrystal such that it exhibits a stronger affinity for one block[17]. In our case, we compatibilized Au nanoparticles with thiol-terminated, low molecular weight polystyrene, thereby rendering the nanocrystal-PS system to interact favorably with the PS domains. A Z-contrast image of an unstained, as-cast 70 nm thick film containing 10w/w% of Au-$PS_{10}SH$ reveals (Fig. 3a) that the nanoparticles are indeed preferentially located within the continuous PS phase. This film is sufficiently thick to be composed of two layers of micelles. However, we observe that without RuO_4 staining, the contrast between PS and PFOMA is only strong enough to show one layer of micellar aggregates. The staining of a similar film allows us to image micelles in different layers, as shown in figure 5.3b.

In figure 5.4 the morphology of a PS-b-PFOMA/Au-$PS_{10}SH$ nanocomposite film (5w/w%) annealed in CO_2, at 75ºC and 13.8 MPa is presented. From the Z-contrast image it is evident that the inversion of the as-cast morphology has been achieved and the nanocrystals are constrained to follow the morphological change; i.e.: they remain sequestered within the PS domains. The PS core domains in this 64 nm thick film have an average characteristic size of 97 nm with a broad distribution of sizes (ranging from 35 to 160 nm), and contain approximately 20 nanoparticles per aggregate.

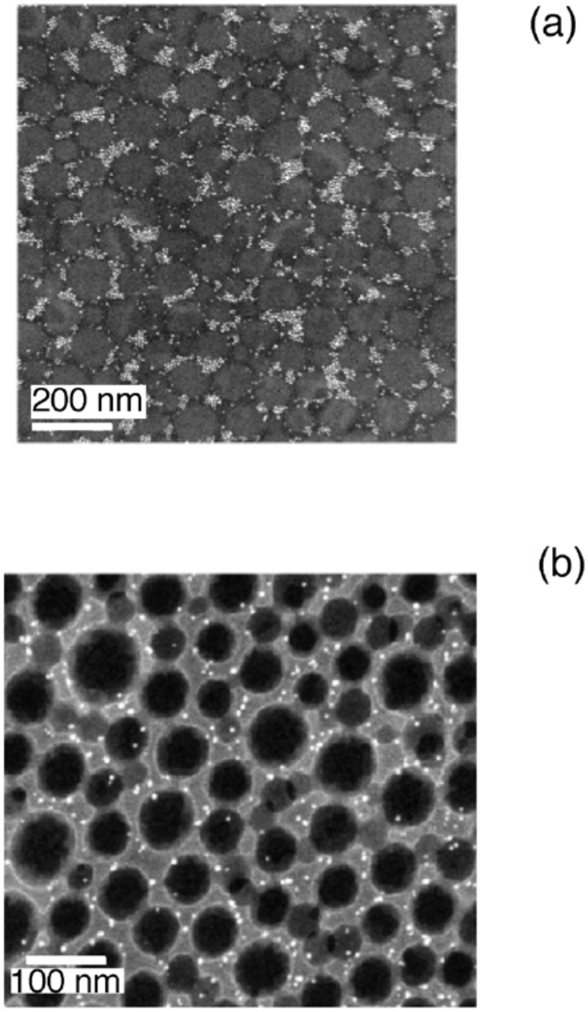

Figure 5.3 Internal structure of an as-cast PS-b-PFOMA film loaded with Au-PSSH nanoparticles. **(a)** Z-contrast image of a 70nm thick film showing the sequestering of the Au nanoparticles to the PS coronae (10w/w%). **(b)** Z-contrast image of a 60nm thick film stained with RuO_4 (5w/w%).

5.3.3 Shape of PS-b-PFOMA Micellar Aggregates Annealed in $scCO_2$

The feasibility of switching the location of nanocrystals in conjunction with the block copolymer template has been established, and we now direct our attention to the size and shape of the micellar structures, focusing on the CO_2 annealed films. A cross-sectional, Z-contrast image of a PS-PFOMA nanocomposite film containing 10 w/w% of Au-PS_{10}SH annealed in $scCO_2$ shows that aggregates closest to the free surface tend to adopt an ellipsoidal configuration (Fig. 5a), with the major axis lying parallel to substrate (B/A = 1.24, where B and A are the major and minor axis defined in the schematic representation of figure 5.5c). Eisenberg and coworkers[18] have estimated the size of a typical block copolymer micelle in solution from the degree of core-chain stretching, S_c, specified by $S_c = R/l_e$, where R is the radius of the micelle core and l_e is the end-to-end distance of the PS block in the unperturbed state ($l_{e\text{-}PS}$ = 10.5nm[18]). As mentioned in reference 12, values of S_c found in the literature range from 0.7-1.5. In our case R is equal to the minor axis, A, measured from the cross-section image of the nanocomposite film (<A> = 23.1 nm). The data shows that the degree of stretching of the core PS block is high in comparison to other systems reported in the literature (S_c = 2.2). The high degree of stretching may be explained by considering that the PS block can swell up to 22% with RuO_4, as measured by Sohn and coworkers[7] for a PS-PMMA diblock copolymer. Other factors that may help explain this discrepancy are the possible deformation of the aggregates during microtomy[19], as well as effect of confinement and interfacial interactions in the degree of stretching of the block copolymer chains[20, 21].

It is worth mentioning that the cross-sectional image of this film also reveals the fact that these ellipsoidal aggregates do not contain gold nanocrystals within them. We will return to this point later, when the data in figure 5.6, showing a depth profile of the nanoparticles, is discussed.

Up to now, we have examined the size and shape of the micelle-like aggregates near the free surface, but we have failed to mention that aggregates closest to the substrate seem to be forming spherical caps, with a base radius, L (see figure 5.5c), significantly larger than the major axis of the ellipsoidal aggregates above them (<L> = 76.2 nm, while <B> = 28.6 nm). These spherical-capped aggregates could be easily mistaken for surface micelles that have the core block directly adsorbed to the substrate[22, 23]. However, measurements of the average height of the aggregates, <h>, show that a PS core chain would have to be stretched nearly 6 times its unperturbed dimensions if indeed the height of the core was approximately the length of one PS block chain (<h> = 59.1nm). This leads us to believe that the height of the spherical-capped core is comprised of two PS block chains, as depicted in the schematic of figure 5.5c. The internal structure described above would allow for a more realistic degree of core chain stretching ($S_c = \langle h \rangle / 2l_e = 2.7$), especially if one considers that in this case the core is swollen not only by the staining agent, but also by the gold nanoparticles sequestered within it. Such a structure would also allow the adsorption of the PFOMA block onto the substrate, assuming there is a preferential affinity between the carbonyl groups in the PFOMA monomer and the polar silicon nitride substrate. However, this cannot be corroborated from the cross-sectional image since we cannot differentiate between the PFOMA block and the epoxy resin in which the BCP is embedded.

The distortion in the shape of the micelles is likely to be the result of the preferential interactions between the PFOMA block and the substrate. That is, the strong affinity between the PFOMA chains and the polar silicon nitride substrate may cause the PFOMA chains to be somewhat anchored on the substrate, leading to a deformation of the curvature of the micelles close to this interface. The chains located next to the substrate will therefore form a planar interface (brush), while an undulation will develop in the chains directly above them to match onto the ellipsoidal shape of the aggregates in the subsequent layer, and eventually form a bulk spherical phase when the film is thick enough.

It is important to mention that the existence of the two types of micellar aggregates shown in the cross-section of the BCP film, the spherical-capped aggregates and the ellipsoidal aggregates, each with a characteristic size, clarifies the broad distribution of sizes measured in the in-plane image of the film (Fig. 4).

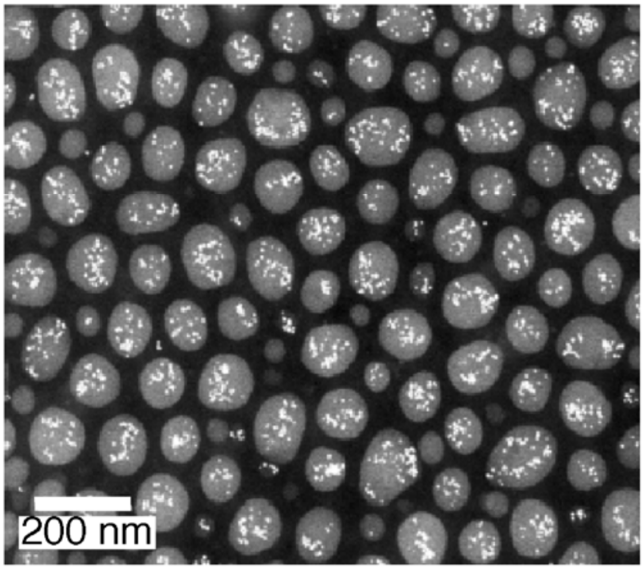

Figure 5.4 Z-contrast image of a single-layered, 64 nm PS-b-PFOMA film with 5w/w% nanoparticle loading; the film was processed for 15 days in $scCO_2$. (T=75°C and P=13.8 MPa). The image clearly shows that the Au nanoparticles are able to follow the morphological transition induced by $scCO_2$.

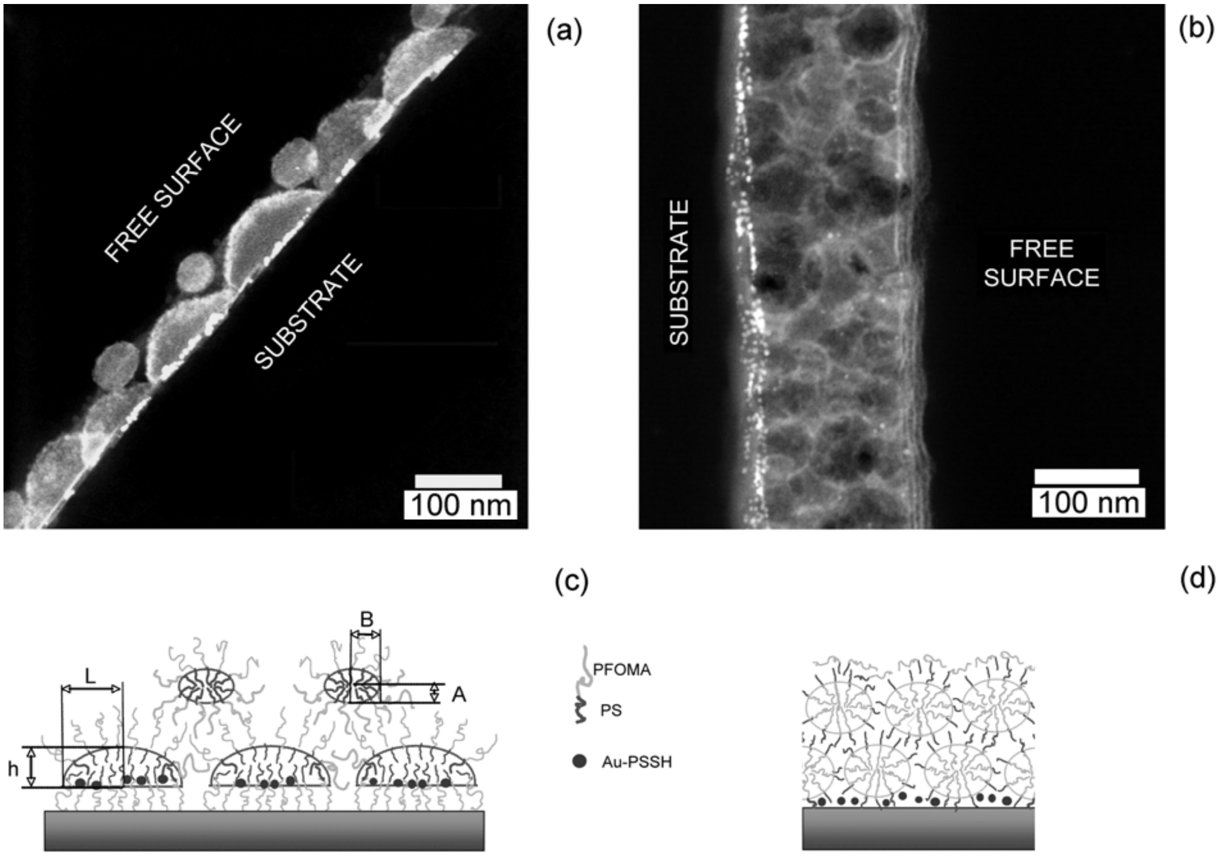

Figure 5.5 (a) Cross-sectional, Z-contrast image of a PS-b-PFOMA film with 5w/w% nanoparticle loading after scCO2 processing (T = 75°C, 13.8 MPa, and t = 15 days) (b) Cross-sectional, Z-contrast image of an as-cast PS-PFOMA film with Au-PSSH (5w/w%) (c) Schematic diagram of the internal structure of the film shown in part (a), depicting the formation of ellipsoidal aggregates close to the free surface and spherical-capped aggregates near the substrate, where the nanoparticles are selectively segregated (d) Schematic representation of the structure of the as-cast film shown in part (b) illustrating the preferential segregation of the Au-PSSH particles to the substrate. All of the samples in this figure were stained with RuO4 prior to imaging.

5.3.4 Depth Distribution of Gold Nanoparticles across PS-b-PFOMA films

Cross-sectional images of the as-cast, as well as the CO_2 annealed BCP/nanocomposite films, are shown in figure 5.5b and 5.5a, respectively. In both films, the gold nanoparticles seem to be segregated to the substrate. To obtain more information on the Au particle distribution across the films we monitored the secondary ion count rate of C, Si, and Au negative ions as a function of sputtering time using dynamic secondary ion mass spectroscopy (DSIMS). The Au signal from an as-cast, 160nm PS-b-PFOMA/Au-PSSH thick film (5 w/w%) was normalized to yield the relative concentration profile shown in figure 5.6a. The presence of a Gaussian peak near the silicon nitride substrate after normalization is evident. Thus, the SIMS analysis confirms that the gold particles are preferentially segregated to the substrate (Fig. 5d) spanning a region no thicker than 30nm, obtained from the full width at half maximum (FWHM). The depth profile of Au in a 108 nm thick PS-b-PFOMA film (5 w/w%) annealed in CO_2 was subsequently obtained (Fig. 6b), verifying that there is still considerable enrichment of Au near the substrate after CO_2 processing, for the thickness and concentration analyzed.

Computational studies on filled BCP systems confined between two identical surfaces have shown that the polymer melt can induce an entropic depletion attraction between the nanoparticles and walls, whereby a fraction of particles is driven to the interfaces to increase the conformational entropy of the BCP chains, [24] In our experiments, the interfacial interaction between the gold nanoparticles and the interfaces, free surface and substrate, should not be symmetric. Considering that both Au and silicon nitride are high-energy surfaces, it is likely that the PS brush covering the particles may not be sufficiently thick to adequately screen the attractive interactions between substrate and gold, and thus lead to preferential segregation of the gold nanoparticles to this interface.

We explored this possibility by estimating the non-retarded, long-range, van der Waals interactions between a sheathed sphere and a wall, following a microscopic approach for multilayer structures[25]. We considered that the intervening polymeric medium was composed of a 25:75 mixture of PS and PFOMA, respectively, while the adsorbed $PS_{10}SH$ layer was assumed to be an impenetrable PS layer of 2nm in thickness. The details of this calculation are included as supporting information. As expected, the effective interface potential between the sheathed Au particle and the silicon nitride substrate, depicted in figure 5.6c, shows a net attraction between the crystals and the macroscopic body. On the other hand, a repulsive force between these particles and the free surface is obtained when substituting the silicon nitride wall for air. Qualitatively, the same result is obtained when the interfacial energy calculation accounts for the presence of CO_2, both as a pure phase, as well as adsorbed within the polymer film and in the ligand (Fig. 6c). Therefore, the rough interaction energy calculations are consistent with our experimental observations of preferential segregation of gold towards the substrate.

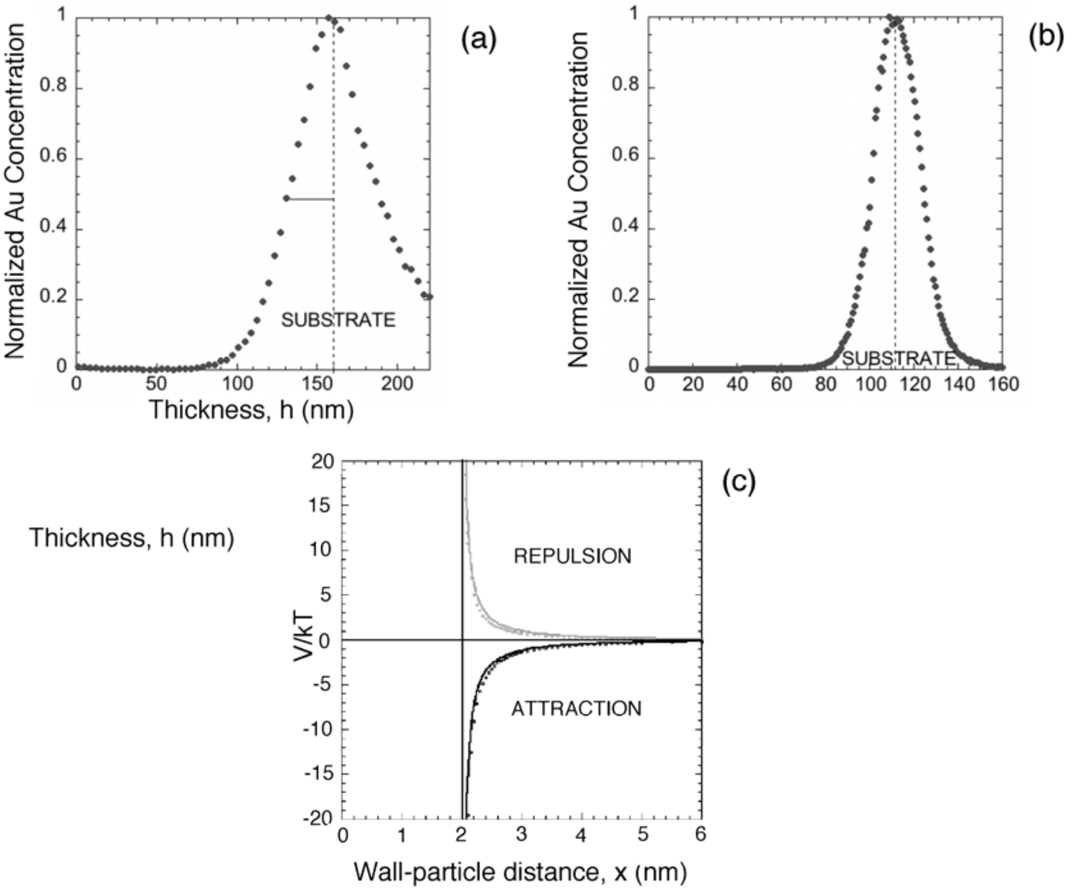

Figure 5.6 (a) DSIMS concentration profile showing enrichment of Au near the substrate for an as-cast, 160nm thick film containing 5w/w% of nanoparticles. **(b)** DSIMS Au concentration profile of a 108nm thick film (5w/w%) annealed in $scCO_2$ at 75°C and 13.8MPa, demonstrating that preferential segregation of Au to the substrate is still prevalent **(c)** Calculated van der Waals interaction between a sheathed Au sphere and a wall; the gray curves show a net repulsion between the particles and the free surface, while the black curves show a net attraction between the Au cores and the silicon nitride substrate. Circles (•) correspond to $scCO_2$ environments and solid lines represent the same calculation under air.

It is important to emphasize that the proposed internal morphology of the $scCO_2$ annealed film implies that the gold nanoparticles are actually located at the interface between the PS and the PFOMA block in the spherical-capped aggregates, as illustrated in figure 5.5c. This result is unexpected, considering that the size of the gold nanoparticles is comparable to the radius of gyration of the BCP chain ($D \approx Rg_{PS\text{-}PFOMA}$, where D is the diameter of the nanoparticle considering a brush thickness of approximately 1.9 nm). Theoretical and experimental studies would then suggest that these relatively large particles should be segregated to the center of the PS microdomains,[26, 27] where the loss in conformational entropy of the chains is minimized. Our results suggest that the chain entropy loss incurred by allocating the particles at the block interface is overcome by the enthalpic gain of bringing them closer to the substrate. An additional factor that may need to be evaluated when considering the location of the nanoparticle is the width of the interface between the neighboring blocks[28].

5.4 CONCLUSIONS

Our findings demonstrate the feasibility of using $scCO_2$ annealing as a means of controlling composite nanostructure in a dynamic fashion. It is clearly illustrated that manipulation of energetic interactions, such as polymer-solvent, nanoparticle-polymer and particle-interface interactions, is not only desirable but crucial for precise control of morphology in thin film composite nanostructures.

5.5 REFERENCES

1. Abes, S. I.; Cohen, R. E.; Ross, C. A. *Chemistry of Materials* 2003, 15, 1125-1131.
2. Brown, G. D.; Watkins, J. J. *Polymeric Materials Science and Engineering* 2001, 84, 130.
3. Sohn, B. H.; Seo, B. H. *Chemistry of Materials* 2001, 13, 1752-1757.
4. Sohn, B. H.; Yoo, S. I.; Seo, B. W.; Yun, S. H.; Park, S. M. *Journal of the American Chemical Society* 2001, 123, 12734-12735.
5. Mayer, A. B. R.; Mark, J. E. *Colloid and Polymer Science* 1997, 275, 333.
6. Sohn, B. H.; Cohen, R. E. *Chemistry of Materials* 1997, 9, 264.
7. Park, S. M.; Yun, S. H.; Sohn, B. H. *Macromolecular Chemistry and Physics* 2002, 203, (14), 2069-2074.
8. Bockstaller, M. E.; Kolb, R.; Thomas, E. L. *Advanced Materials* 2001, 13, (23), 1783-1786.
9. Kim, B. J.; Chiu, J. J.; Yi, G. R.; Pine, D. J.; Kramer, E. J. *Advanced Materials* 2005, 17, 2618.
10. Lauter-Pasyuk, V.; Lauter, H. J.; Ausserre, D.; Gallot, Y.; Cabuil, V.; Kornilov, E. I.; Hamdoun, B. *Physica B* 1998, 241-243, 1092-1094.
11. Schmaltz, B.; Brinkmann, M.; Mathis, C. *Macromolecules* 2004, 37, 9056-9063.
12. Li, Y.; Meli, L.; Lim, K. T.; Johnston, K. P.; Green, P. F. *Macromolecules* 2006, 39, 7044-7054.
13. Brust, M.; Walker, M.; Bethell, D.; Schiffrin, D. J.; Whyman, R. *Journal of the Chemical Society. Chemical Communications* 1994, 801.
14. Condo, P. D.; Paul, D. R.; Johnston, K. P. *Macromolecules* 1994, 27, (2), 365-371.
15. Wissinger, R. G.; Paulaitis, M. E. *Journal of Polymer Science: Part B: Polymer Physics* 1991, 29, (5), 631-633.

16. Arnold, M. E.; Nagal, K.; Freeman, B. D.; Spontak, R. J.; Betts, D. E.; DeSImone, J. M. *Macromolecules* 2001, 34, (16), 5611-5619.

17. Bockstaller, M. R.; Mickiewicz, R. A.; Thomas, E. L. *Advanced Materials* 2005, 17, 1331-1349.

18. Zhang, L. F.; Eisenberg, A. *Journal of the American Chemical Society* 1996, 118, (13), 3168-3181.

19. Cameron, N. S.; Corbierre, M. K.; Eisenberg, A. *Canadian Journal of Chemistry* 1999, 77, 1311-1326.

20. Milner, S. T.; Witten, T. A.; Cates, M. E. *Macromolecules* 1988, 21, (8), 2610-2619.

21. Milner, S. T. *Europhysics Letters* 1988, 7, (8), 695-699.

22. Shull, K. R. *Macromolecules* 1993, 26, (9), 2346-2360.

23. Ligoure, C. *Macromolecules* 1991, 24, (10), 2968-2972.

24. Lee, J. Y.; Thompson, R. B.; Jasnow, D.; Balazs, A. C. *Macromolecules* 2002, 35, 4855-4858.

25. Nir, S. *Progress in Surface Science* 1976, 8, (1), 1-58.

26. Kim, J. U.; O'Shaughnessy, B. *Macromolecules* 2006, 39, (1), 413-425.

27. Thompson, R. B.; Ginzburg, V. V.; Matsen, M. W.; Balazs, A. C. *Science* 2001, 292, (5526), 2469-2472.

28. Haryono, A.; Binder, W. H. *Small* 2006, 2, (5), 600-611.

29. Meli, L.; Pham, J. Q.; Johnston, K. P.; Green, P. F. *Physical Review E* 2004, 69, 051601-1 - 051601-8.

30. Ackler, H. D.; French, R. H.; Chiang, Y. T. *Journal of Colloid and Interface Science* 1996, 179, 460-469.

31. Israelachvili, J. N., *Intermolecular and Surface Forces*. 2nd ed.; Academic Press: Suffolk, 1992; p 450.

32. Arnold, M. E.; Nagai, K.; Spontak, R. J.; Freeman, B. D.; Leroux, D.; Betts, D. E.; DeSimone, J. M.; DiGiano, F. A.; Stebbins, C. K.; Linton, R. W. *Macromolecules* 2002, 35, 3697-3707.

33. Lewis, J. E.; Biswas, R.; Robinson, A. G.; Maroncelli, M. *Journal of Physical Chemistry B* 2001, 105, (16), 3306-3318.

Chapter 6: Conclusions and Recommendations for Future Work

In this dissertation we examined the nature of the interactions that control the microstructure of thin film nanocomposite. Processing strategies that could help tailor and maintain a given structure were also investigated. This closing Chapter contains a summary of the key findings of our research as well as recommendations for future work.

6.1 CONCLUSIONS

6.1.1 Morphology of Homopolymer and Nanocomposite Thin Films Processed under Compressed CO_2 Environments

As a first step, we studied the use of compressed CO_2 for the low temperature processing of pure polystyrene (PS) thin films. Specifically, we considered the influence that temperature, and the associated volume fraction of CO_2 absorbed within the film, had on the development of structural instabilities and on the rates of destabilization of the polymer. The PS films, which are plasticized in this temperature range, were found to be metastable, wherein holes nucleated and increased in size. Calculations of the effective interface potential for the system suggest that the barrier to nucleation is higher in CO_2 than in air, and in the limit of vanishingly low PS volume fraction the films should be stable. Furthermore, the kinetics of destabilization are shown to be controlled by three factors: film thickness, temperature, and CO_2 volume fraction.

We then studied the effects that different processing schemes have on the coarsening of sterically-stabilized nanoparticles in homopolymer thin films. Particularly, we performed a comparative study of the size evolution of the nanoparticles in a poly(methyl methacrylate) (PMMA) film under vacuum and supercritical carbon dioxide ($scCO_2$) environments. In vacuum, the coarsening dynamics are characterized by two distinct growth stages: during the initial stages coarsening occurs via simultaneous Ostwald ripening and coalescence, and in the second stage the dominant coarsening mechanism is coalescence. Annealing in $scCO_2$ environments, above the T_g of the CO_2 plasticized PMMA film, prevents coarsening of the nanoparticles in the composite film due to greater stability of the ligands that passivate the gold cores.

6.1.2 Control of the Spatial Distribution of Nanofillers in Homopolymer and Block Copolymer Thin Films

We started by examining the nature of the interactions that control the spatial organization of PS-coated gold nanoparticles embedded in PS thin films. By studying an athermal nanoparticle/polymer mixture, we were able to understand in greater detail the role that different entropic interactions have on nanoparticle dispersion. Careful control of nanoparticle size, molecular weight of grafted and free polymer chains, and grafting density, allowed us to better isolate the entropic effects that lead to a given spatial distribution. We propose that the depth distribution of nanoparticles within the non-adsorbing polymer matrix is the result of three main contributions: (1) an entropic depletion attraction between nanoparticles and interfaces due to the reduced conformational entropy of the matrix chains near a large particle, (2) the interfacial energy between the polymer host and the grafted brush, and (3) the translational entropy of the nanoparticles which promotes their dispersion within the film. By coupling our experiments with theoretical phase diagrams for the brush structure and wetting characteristics[1, 2], we were able to qualitatively assess the importance of each of these three contributions in the spatial distribution of the nanoparticles across the film.

Finally, further control of nanocomposite structure was gained by using a fluorinated diblock copolymer, polystyrene-b-(1,1',2,2'-tetrahydroperfluorooctyl methacrylate) (PS-b-PFOMA), as template to direct the spatial distribution of nanoparticles within a film. We showed that functionalized gold nanocrystals sequestered within the microdomains of self-assembled aggregates of PS-PFOMA thin films are capable of following the structure-guiding matrix in a morphological transition from spherical PFOMA aggregates in a PS matrix, to the inverse morphology upon $scCO_2$ sorption. An analysis of the distribution of gold nanoparticles across the films sheds some light into the energetic interactions that control the formation of nanostructures within them.

6.2 RECOMMENDATIONS FOR FUTURE WORK

6.2.1 Homopolymer Nanocomposites

Chapter 3 investigated the depth distribution of PS-coated gold nanoparticles in a PS melt, as function of grafting density, σ, effective nanoparticle size, R_e, and molecular weight of the matrix and grafted chains, P and N, respectively. Most of our samples, however, had densely grafted brushes ($\sigma N^{1/2}>1$) and long melt chains ($P>N$) that form dry brushes with positive spreading coefficients. It would be desirable to expand the parameter space studied to include samples where the nanoparticles have wet brushes that share repulsive interactions with the melts. These experiments could be coupled with experiments that study the wetting of the Au-PSSH surface by the PS matrices. Wetting experiments with bilayers of Au-PSSH and PS could help us determine wetting transitions, as well as the magnitude of repulsive interactions between brush and melt (monitoring contact angle changes in dewetting melts). The results could be compared with previous wetting experiments on planar brushes[3], to analyze the effect of brush curvature on wetting.

In Chapter 4, we studied the coarsening of sterically-stabilized nanoparticles in a polymer thin film matrix, where both enthalpic and entropic interactions were present. It is important to mention that the favorable enthalpic interactions between grafted ligands and the free surface in this system lead to complete segregation of the nanoparticles to the free surface. Thus, we effectively studied coarsening of the fillers in a two-dimensional diffusion field (some penetration of the nanoparticles might have occurred at long times, when the ligands were thermally desorbed). Perhaps a deeper understanding of the mechanisms that engender coarsening could be gained by considering the size evolution of nanoparticles in an athermal mixture, as the one studied in Chapter 3. Theoretical and experimental works have studied the interaction between brushes immersed in a chemically identical polymer melt (albeit for flat brushes) as a function of σ, N, and P. Knowledge of this interaction could then give us more information about the collision rate, collision efficiency, and reversibility of the nanoparticle aggregation process. Indeed, precise control of this interaction could be attainable by modifying simple experimental parameters. Moreover, control of the depth distribution of nanoparticles in the non-adsorbing melt could be utilized to perform a comparative study of coarsening of nanoparticles in two- and three-dimensional diffusion fields.

It would then be desirable to study the effect of enthalpic interactions in the coarsening of the nanoparticles by systematically changing the chemistry of ligands that passivate the nanoparticle surface, or the chemical nature of the polymer melt.

6.2.2 Block Copolymer Nanocomposites

In the past decade, researchers have devoted a considerable amount of effort in studying the self-assembly of nanoparticles in diblock copolymer scalffolds[4-9]. A general understanding of the energetic interactions that can help us control the nanostructure of a bulk block copolymer nanocomposite has now been developed. However, there are few systematic studies on the structure-property relations of these novel materials. Noted exceptions are, for example, the reports on optical property measurements in ordered structures obtained by self-assembly of block copolymer/nanoparticle mixtures[4, 10]. Therefore, the next logical step is to develop matrices with optimized properties for specific applications. For example, such matrices could be exploited as catalytically active materials in which there is precise control of nanoparticle chemistry, location, size, shape and metal structure, as well as control of support morphology and chemistry. The isolation of these parameters yields a unique opportunity to study the mechanisms that affect catalyst performance. Recent developments in techniques that measure local properties, such as CAFM, MFM, EFM, etc., are expected to provide invaluable information on the physical phenomena that occur at the interface between polymers and nanoparticles.

6.3 REFERENCES

1. de Gennes, P. G. Macromolecules **1980,** 13, (5), 1069-1075.
2. Gay, C. Macromolecules **1997,** 30, (19), 5939-5943.
3. Maas, J. H.; Fleer, G. J.; Leermakers, F. A. M.; Stuart, M. A. C. Langmuir **2002,** 18, (23), 8871-8880.
4. Bockstaller, M. R.; Mickiewicz, R. A.; Thomas, E. L. Advanced Materials **2005,** 17, 1331-1349.
5. Chiu, J. J.; Kim, B. J.; Kramer, E. J.; Pine, D. J. Journal of the American Chemical Society **2005,** 127, (14), 5036-5037.
6. Haryono, A.; Binder, W. H. Small **2006,** 2, (5), 600-611.
7. Lauter-Pasyuk, V.; Lauter, H. J.; Ausserre, D.; Gallot, Y.; Cabuil, V.; Kornilov, E. I.; Hamdoun, B. Physica B **1998,** 241-243, 1092-1094.
8. Lee, J. Y.; Shou, Z. Y.; Balazs, A. C. Macromolecules **2003,** 36, (20), 7730-7739.
9. Lee, J. Y.; Thompson, R. B.; Jasnow, D.; Balazs, A. C. Macromolecules **2002,** 35, 4855-4858.
10. Bockstaller, M. E.; Kolb, R.; Thomas, E. L. Advanced Materials **2001,** 13, (23), 1783-1786.

Appendices

APPENDIX A. NANOPARTICLE BILAYERS

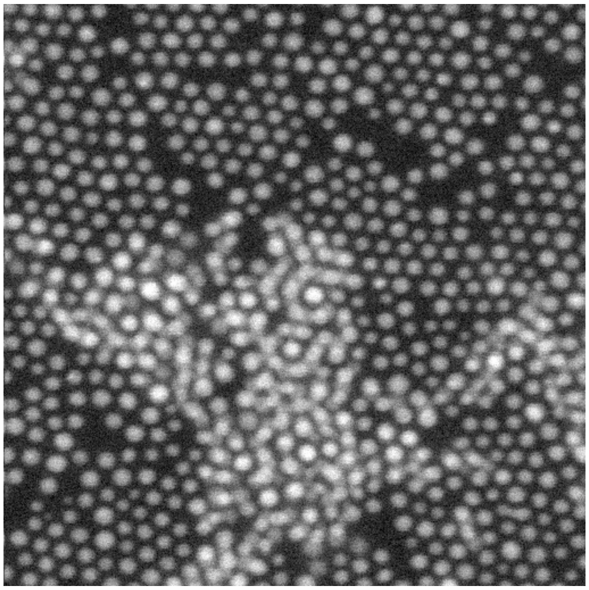

Figure S1. HAADF image of the nanoparticle network formed within the as-cast PMMA films, illustrating that brighter regions in the image correspond to nanoparticle bilayer domains.

APPENDIX B. INTERFACIAL SEGREGATION OF NANOPARTICLES.

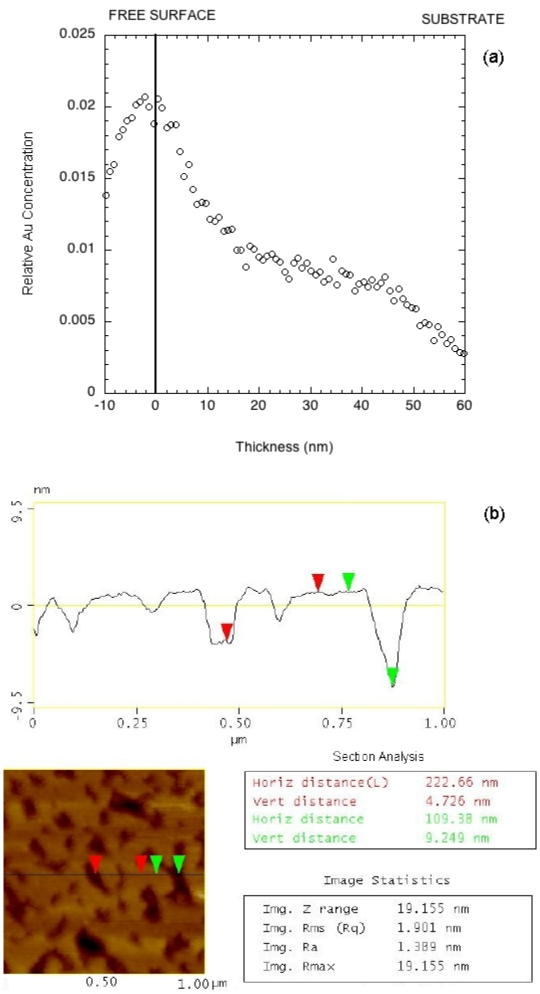

Section Analysis

```
Horiz distance(L)      222.66 nm
Vert distance          4.726 nm
Horiz distance         109.38 nm
Vert distance          9.249 nm
```

Image Statistics

```
Img. Z range        19.155 nm
Img. Rms (Rq)       1.901 nm
Img. Ra             1.389 nm
Img. Rmax           19.155 nm
```

Figure S2. Interfacial segregation of nanoparticles within the PMMA films. (a) DSIMS concentration profile shows enrichment of Au near the free surface of an as-cast, 60 nm thick film. (b) SFM image of the as-cast films demonstrating that the surface of the films presents nanometer deep features and a large RMS roughness.

APPENDIX C. CO_2 INDUCED T_G SUPPRESSION IN POLYSTYRENE

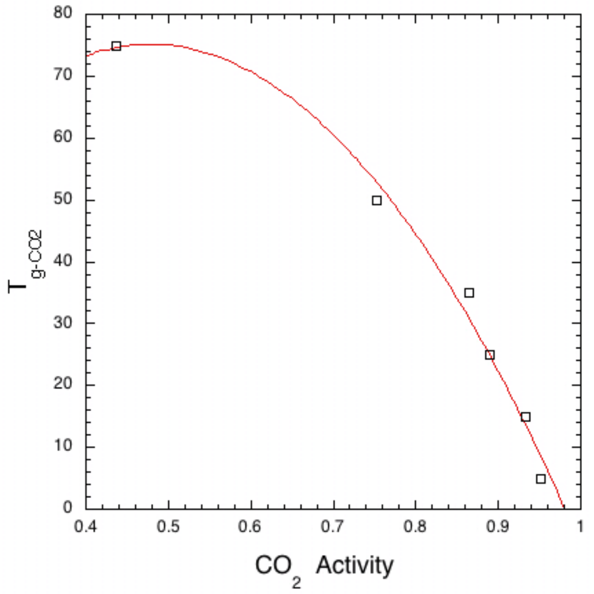

Figure S3. The depression of the glass transition temperature as a function of CO_2 activity extracted from data of Condo and coworkers [1, 2]

1. Condo, P. D.; Johnston, K. P. *Macromolecules* **1992,** 25, (24), 6730-6732.

2. Condo, P. D.; Paul, D. R.; Johnston, K. P. *Macromolecules* **1994,** 27, (2), 365-371.

APPENDIX D. INTERACTION POTENTIAL BETWEEN SPHERICAL PARTICLE AND FLAT WALL.

The interaction potential between the particle and the substrate is given by the following equation:

$$V_{vdW} = -\frac{1}{12}\left[\left(A_{PS-POL-Si_3N_4}\right)H(x_{1,1}) + (A_{Au-POL-Si_3N_4} - A_{PS-POL-Si_3N_4})H(x_{1,2})\right], \quad (1)$$

$$H(x_{i,j}) = \frac{1}{x_{ij}} + \frac{1}{x_{ij}+1} + 2\ln\frac{x_{ij}}{x_{ij}+1}, \quad (2)$$

$$x_{11} = \frac{d}{2R}; x_{12} = \frac{d + l_{PSSH}}{2R} \quad (3).$$

Parameters d, l, and R are defined in the schematic presented in figure S4, and the Hamaker constant for the compound media, A_{123}, were estimated from the pure component Hamaker constants,

$$A_{123} \approx (A_{11} - A_{22})(A_{33} - A_{22}). \quad (4)$$

The pure component constants can be calculated from dielectric properties of the materials[29, 30] and the approximation given below[31]:

$$A_{11} = (3/4)kT\left(\frac{\varepsilon_1 - 1}{\varepsilon_1 + 1}\right)^2 + \frac{3h\nu_e}{16\sqrt{2}}\frac{(n_1^2 - 1)}{(n_1^2 + 1)^{3/2}} \quad (5)$$

where k is the Boltzmann constant, T is the absolute temperature, ε is the static dielectric constant, n the refractive index, and ν_e is the first resonant frequency, which is typically around $3\text{x}10^{15}$ Hz. This dispersion formula cannot be used for interactions involving conducting media since their static dielectric constant is infinite. Thus, the Hamaker constant for Au was obtained from the literature[31]. Finally, the Hamaker constant for PFOMA was roughly estimated from its surface energy with A ≈ $2.1\mathrm{x}10^{-21}\gamma$[32], and the constant of the polymer medium (PS/PFOMA) was obtained from the known block volume fraction,φ_{ps} :

$$A_{POl-POl} = \left[\varphi_{PS}\sqrt{A_{PS-PS}} + (1-\varphi_{PS})\sqrt{A_{PFOMA-PFOMA}}\right] \tag{6}$$

For simplicity, a hard-shell repulsion model was used to illustrate the short-range interactions:

$$\begin{aligned} V_{steric} &= \infty \rightarrow x \le l_{PS} \\ V_{steric} &= 0 \rightarrow x > 0 \end{aligned} \tag{7}$$

We repeated this calculation accounting for the presence of CO_2, both as an environment, as well as adsorbed within the polymer film and in the ligand. In these potential curves, the Hamaker constant of CO_2 was calculated with equation 5, and experimental correlations of the dielectric properties of CO_2 with respect to the reduced density[33]. The swollen polymer and ligand Hamaker constants were estimated with equation 6, and the volume fraction of CO_2 obtained from swelling experiments.

APPENDIX E. SCHEMATIC FOR INTERACTION POTENTIAL CALCULATION

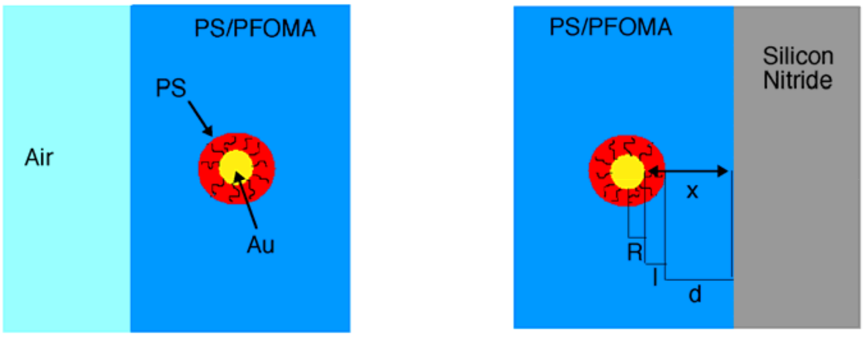

Figure S4 Diagram depicting geometric model employed in the calculation of the long-range van der Waals interaction between a sheathed sphere and a wall.

References

1. Abes, S. I.; Cohen, R. E.; Ross, C. A. *Chemistry of Materials* **2003,** 15, 1125-1131.

2. Ackler, H. D.; French, R. H.; Chiang, Y.-T. *Journal of Colloid and Interface Science* **1996,** 179, 460.

3. Alavastos, A. P. *Science* **1996,** 933.

4. Alexander, S. *Journal De Physique* **1977,** 38, (8), 983-987.

5. Alexandris, P.; Lindman, B., *Amphiphilic Block Copolymers. Self-Assembly and Applications.* 1st ed.; Elsevier: Amsterdam, 2000; p 435.

6. Alyabeva, A. V.; Buyevich, Y. A.; Mansurov, V. V. *Journal De Physique Ii* **1994,** 4, (6), 951-957.

7. Arceo, A.; Green, P. F. *Journal of Physical Chemistry B* **2005,** 109, (15), 6958-6962.

8. Ardell, A. J. *Journal of the European Ceramic Society* **1999,** 19, (13-14), 2217-2231.

9. Ardell, A. J. *Materials Science and Engineering a-Structural Materials Properties Microstructure and Processing* **1997,** 238, (1), 108-120.

10. Arnold, M. E.; Nagai, K.; Spontak, R. J.; Freeman, B. D.; Leroux, D.; Betts, D. E.; DeSimone, J. M.; DiGiano, F. A.; Stebbins, C. K.; Linton, R. W. *Macromolecules* **2002,** 35, 3697-3707.

11. Arnold, M. E.; Nagal, K.; Freeman, B. D.; Spontak, R. J.; Betts, D. E.; DeSImone, J. M. *Macromolecules* **2001,** 34, (16), 5611-5619.

12. Bansal, A.; Yang, H. C.; Li, C. Z.; Benicewicz, R. C.; Kumar, S. K.; Schadler, L. S. *Journal of Polymer Science Part B-Polymer Physics* **2006,** 44, (20), 2944-2950.

13. Barel, R.; Mai, Y.; Carlow, G. R.; ZinkeAllmang, M. *Applied Surface Science* **1996,** 104, 669-678.

14. Barnes, K. A.; Douglas, J. F.; Liu, D. W.; Karim, A. *Advances in Colloid and Interface Science* **2001,** 94, (1-3), 83-104.

15. Benaissa, M.; Gonsalves, K. E. *Applied Physics Leters* **1997,** 71, 3685.

16. Bigioni, T. P.; Lin, X. M.; Nguyen, T. T.; Corwin, E. I.; Witten, T. A.; Jaeger, H. M. *Nature Materials* **2006,** 5, (4), 265-270.

17. Bliznyuk, V.; Ruhstaller, B.; Brock, P. J.; Scherf, U.; Carter, S. A. *Advanced Materials* **1999,** 11, (15), 1257-+.

18. Bockstaller, M. E.; Kolb, R.; Thomas, E. L. *Advanced Materials* **2001,** 13, (23), 1783-1786.

19. Bockstaller, M. R.; Mickiewicz, R. A.; Thomas, E. L. *Advanced Materials* **2005,** 17, 1331-1349.

20. Borelli, N. F.; Hall, D. W.; Holland, H. J.; Smith, D. W. *Journal of Applied Physics* **1987,** 61, 5399.

21. Borukhov, I.; Leibler, L. *Macromolecules* **2002,** 35, (13), 5171-5182.

22. Botet, R.; Jullien, R. *Journal of Physics a-Mathematical and General* **1984,** 17, (12), 2517-2530.

23. Brochard-Wyart, F.; Daillant, J. *Canadian Journal of Physics* **1990,** 68, 1084.

24. Brochard-Wyart, F.; Meglio, J.-M. d.; Quere, D.; Gennes, P.-G. d. *Langmuir* **1990,** 7, 335.

25. Brown, G. D.; Watkins, J. J. *Polymeric Materials Science and Engineering* **2001,** 84, 130.

26. Brust, M.; Fink, J.; Bethell, D.; Schiffrin, D. J.; Kiely, C. *Journal of the American Chemical Society* **1995,** Communications, 1655.

27. Brust, M.; Walker, M.; Bethell, D.; Schiffrin, D. J.; Whyman, R. *Journal of the Chemical Society-Chemical Communications* **1994**, (7), 801-802.

28. Buxton, G. A.; Lee, J. Y.; Balazs, A. C. *Macromolecules* **2003,** 36, (25), 9631-9637.

29. Cameron, N. S.; Corbierre, M. K.; Eisenberg, A. *Canadian Journal of Chemistry* **1999,** 77, 1311-1326.

30. Carlow, G. R. *Physica A* **1997,** 239, (1-3), 65-77.

31. Cheng, J. Y.; Ross, C. A.; Smith, H. I.; Thomas, E. L. *Advanced Materials* **2006,** 18, (19), 2505-2521.

32. Chiu, J. J.; Kim, B. J.; Kramer, E. J.; Pine, D. J. *Journal of the American Chemical Society* **2005,** 127, (14), 5036-5037.

33. Chow, T. S. *Macromolecules* **1980,** 13, 362.

34. Coleman, J. N.; Khan, U.; Gun'ko, Y. K. *Advanced Materials* **2006,** 18, (6), 689-706.

35. Condo, P. D.; Johnston, K. P. *Macromolecules* **1992,** 25, (24), 6730-6732.

36. Condo, P. D.; Paul, D. R.; Johnston, K. P. *Macromolecules* **1994,** 27, (2), 365-371.

37. Condo, P. D.; Sanchez, I. C.; K.P.Johnston. *Macromolecules* **1992,** 25, (23), 6128.

38. de Gennes, P. G. *Rev. Mod. Phys.* **1985,** 57, 827.

39. de Gennes, P. G. *Macromolecules* **1980,** 13, (5), 1069-1075.

40. Dickson, J. L.; Binks, B. P.; Johnston, K. P. *Langmuir* **2004,** 20, (19), 7976-7983.

41. Dresselhaus, G.; Dresselhaus, M. S. *Physical Review Letters* **1967,** 160, 649.

42. Family, F.; Meakin, P. *Physical Review Letters* **1988,** 61, (4), 428-431.

43. Fernandez-Nieves, A.; Fernandez-Barbero, A.; Vincent, B.; de las Nieves, F. J. *Langmuir* **2001,** 17, (6), 1841-1846.

44. Ferreira, P. G.; Ajdari, A.; Leibler, L. *Macromolecules* **1998,** 31, (12), 3994-4003.

45. Floro, J. A.; Sinclair, M. B.; Chason, E.; Freund, L. B.; Twesten, R. D.; Hwang, R. Q.; Lucadamo, G. A. *Physical Review Letters* **2000,** 84, (4), 701-704.

46. Forrest, J. A. *The European Physical Journal E* **2002**.

47. Ganesan, V.; Pryamitsyn, V.; Surve, M.; Narayanan, B. *Journal of Chemical Physics* **2006,** 124, (22), -.

48. Gast, A. P.; Leibler, L. *Macromolecules* **1986,** 19, (3), 686-691.

49. Gay, C. *Macromolecules* **1997,** 30, (19), 5939-5943.

50. Gilbert, B.; Zhang, H. Z.; Huang, F.; Finnegan, M. P.; Waychunas, G. A.; Banfield, J. F. *Geochemical Transactions* **2003,** 4, 20-27.

51. Goel, S. K.; Beckman, E. J. *AIChE Journal* **1995,** 41, 357.

52. Goldfarb, D. L.; Pablo, J. J. d.; Nealy, P. F.; Simons, J. P.; Moreau, W. M. *Vac. Sci. Technology B* **2000,** 18, (3313).

53. Goodisman, J.; Chaiken, J. *Journal of Chemical Physics* **2006,** 125, (7), -.

54. Guo, Q.; Sun, X.; Palmer, R. E. *Physical Review B* **2005,** 71, (3), -.

55. Gupta, R. R.; Lavery, K. A.; Francis, T. J.; Webster, J. R. P.; Smith, G. S.; Russell, T. R.; Watkins, J. *Macromolecules* **2003,** 36, 346.

56. Gupta, S.; Zhang, Q. L.; Emrick, T.; Balazs, A. C.; Russell, T. P. *Nature Materials* **2006,** 5, (3), 229-233.

57. Hall, J. J.; Walsh, C. A.; Greenham, N. C.; Marseglia, E. A.; Friend, R. H.; Morati, S. C.; Morati, A. B. *Nature* **1995,** 376, 498.

58. Hamdoun, B. *European Polymer Journal* **2004,** 40, (7), 1559-1564.

59. Hamley, I. W., *The physics of block copolymers*. Oxford University Press: Oxford, 1998.

60. Hanley, K. J.; Lodge, T. P.; Huang, C. I. *Macromolecules* **2000,** 33, (16), 5918-5931.

61. Haryono, A.; Binder, W. H. *Small* **2006,** 2, (5), 600-611.

62. Henni, A.; Jaffer, S.; Mather, A. E. *Canadian Journal of Chemical Engineering* **1996,** 74, (4), 554-557.

63. Hooper, J. B.; Schweizer, K. S. *Macromolecules* **2005,** 38, (21), 8858-8869.

64. Hooper, J. B.; Schweizer, K. S. *Macromolecules* **2006,** 39, (15), 5133-5142.

65. Hooper, J. B.; Schweizer, K. S.; Desai, T. G.; Koshy, R.; Keblinski, P. *Journal of Chemical Physics* **2004,** 121, (14), 6986-6997.

66. Hough, D. B.; White, L. R. *Advances in Colloid and Interface Science* **1980,** 14, 3.

67. Hourri, M.; St-Arnaud, J. M.; Boser, T. K. *Journal of Chemical Physics* **1997,** 106, (5), 1780.

68. Huang, F.; Zhang, H. Z.; Banfield, J. F. *Journal of Physical Chemistry B* **2003,** 107, (38), 10470-10475.

69. Huh, J.; Ginzburg, V. V.; Balazs, A. C. *Macromolecules* **2000,** 33, (21), 8085-8096.

70. Hunter, R. J., *Foundation of Colloid Science*. 2nd ed.; Oxford University Press: New York, 2001.

71. Hunter, R. J., *Foundations of Colloid Science*. 1 ed.; Oxford, University Press: New York, 2001.

72. Israelachvili, J. N., *Intermolecular and Surface Forces*. 2nd ed.; Academic Press: 1992; p 450.

73. Israelachvili, J. N., *Intermolecular and surface forces*. 2nd ed.; Academic Press: Suffolk, 1992.

74. Jacobs, K.; Herminghaus, S. *Langmuir* **1998,** 14, 965.

75. Janssen, R. A. J.; Hummelen, J. C.; Saricifti, N. S. *Mrs Bulletin* **2005,** 30, (1), 33-36.

76. Jeffrey, C. A.; Conrad, E. H.; Feng, R.; Hupalo, M.; Kim, C.; Ryan, P. J.; Miceli, P. F.; Tringides, M. C. *Physical Review Letters* **2006,** 96, (10), -.

77. Jeong, J. I.; Choi, M. *Journal of Colloid and Interface Science* **2005,** 281, (2), 351-359.

78. Jesson, D. E.; Munt, T. P.; Shchukin, V. A.; Bimberg, D. *Physical Review B* **2004,** 69, (4), -.

79. Jullien, R. *New Journal of Chemistry* **1990,** 14, (3), 239-253.

80. Jullien, R.; Kolb, M.; Botet, R. In *Scaling Properties of Growth by Kinetic Clustering of Clusters*, International Topical Conference on Kinetics of Aggregation and Gelation, Athens, Georgia, 1984; Family, F.; Landau, D. P., Eds. North-Holland: Athens, Georgia, 1984; pp 101-109.

81. Kaganer, V. M.; Ploog, K. H.; Sabelfeld, K. K. *Physical Review B* **2006,** 73, (11), -.

82. Kagrupta, K.; Sharma, A. *Journal of Colloid and Interface Science* **2002,** 245, 99.

83. Kang, K.; Redner, S.; Meakin, P.; Leyvraz, F. *Physical Review A* **1986,** 33, (2), 1171-1182.

84. Kargupta, K.; Konnur, R.; Sharma, A. *Langmuir* **2000,** 16, 10243.

85. Kargupta, K.; Sharma, A. *Physical Review Letters* **2001,** 86, 4536.

86. Kato, S.; Tsujita, Y.; Yoshimizu, H.; Kinoshita, T.; Higgins, J. S. *Polymer* **1997,** 38, (11), 2807.

87. Kaya, I. *Polymer-Plastics Technology and Engineering* **1999,** 38, (2), 385-396.

88. Kazarian, S. G. *Polymer Science* **2000,** 41, (1), 78.

89. Keddie, J. L.; Jones, R. A.; Cory, R. A. *Europhysics Letters* **1994,** 27, 59.

90. Khanna, R.; Jameel, A. T.; Sharma, A. *Industry and Engineering Chemistry Resources* **1996,** 35, 3081.

91. Kim, B. J.; Chiu, J. J.; Yi, G. R.; Pine, D. J.; Kramer, E. J. *Advanced Materials* **2005,** 17, 2618.

92. Kim, J. U.; O'Shaughnessy, B. *Physical Review Letters* **2002,** 89, (23), -.

93. Kim, J. U.; O'Shaughnessy, B. *Macromolecules* **2006,** 39, (1), 413-425.

94. Kobayashi, M.; Otake, K.; Yoda, S.; Takebayashi, Y.; Sugeta, T.; Nakazawa, N.; Sakai, H.; Abe, M. *Proceedings from the 6th International Symposium on Supercritical Fluids* **2003**.

95. Koga, T.; Seo, Y.-S.; Hu, X.; Zhang, Y.; Rafailovich, M. H.; Sokolov, J. C.; Chu, B.; Satija, S. K. *Europhysics Letters* **2002,** 60, 559.

96. Konnur, R.; Kagrupta, K.; Sharma, A. *Physical Review Letters* **2000,** 84, (5), 931.

97. Korgel, B. A.; Fullam, S.; Connolly, S.; Fitzmaurice, D. *Journal of Physical Chemistry B* **1998,** 102, (43), 8379-8388.

98. Kralchevsky, P. A.; Nagayama, K. *Langmuir* **1994,** 10, (1), 23-36.

99. Krishnamoorti, R.; Yurekli, K. *Current Opinion in Colloid & Interface Science* **2001,** 6, (5-6), 464-470.

100. Krishnan, R. S.; Mackay, M. E.; Hawker, C. J.; Van Horn, B. *Langmuir* **2005,** 21, (13), 5770-5776.

101. Kwag, C.; Manke, C. W.; Gulari, E. *Industrial & Engineering Chemistry Research* **2001,** 40, (14), 3048-3052.

102. Kwag, C.; Manke, C. W.; Gulari, E. *Journal of Polymer Science Part B-Polymer Physics* **1999,** 37, (19), 2771-2781.

103. Lauter-Pasyuk, V.; Lauter, H. J.; Ausserre, D.; Gallot, Y.; Cabuil, V.; Kornilov, E. I.; Hamdoun, B. *Physica B* **1998,** 241-243, 1092-1094.

104. Lee, J. Y.; Buxton, G. A.; Balazs, A. C. *Journal of Chemical Physics* **2004,** 121, (11), 5531-5540.

105. Lee, J. Y.; Shou, Z. Y.; Balazs, A. C. *Macromolecules* **2003,** 36, (20), 7730-7739.

106. Lee, J. Y.; Thompson, R. B.; Jasnow, D.; Balazs, A. C. *Macromolecules* **2002,** 35, 4855-4858.

107. Lee, K.; Sanchez, I. C. *Private Communication*.

108. Lee, M.; Park, C. B.; Tzoganakis, C. *Polymer Engineering and Science* **1999,** 39, (1), 99-109.

109. Lewis, J. E.; Biswas, R.; Robinson, A. G.; Maroncelli, M. *Journal of Physical Chemistry B* **2001,** 105, (16), 3306-3318.

110. Leyvraz, F.; Redner, S. *Physical Review Letters* **2002,** 88, (6), 16830-1-4.

111. Li, C. X.; Wu, J. T.; Zhao, J.; Zhao, D. L.; Fan, Q. R. *European Polymer Journal* **2004,** 40, (8), 1807-1814.

112. Li, Y.; Meli, L.; Lim, K. T.; Johnston, K. P.; Green, P. F. *Macromolecules* **2006,** 39, 7044-7054.

113. Lifshitz, I. M.; Slyozov, V. V. *Journal of Physics and Chemistry of Solids* **1961,** 19, (1-2), 35-50.

114. Ligoure, C. *Macromolecules* **1991,** 24, (10), 2968-2972.

115. Limary, R.; Green, P. F. *Langmuir* **2003,** 19, (6), 2419-2424.

116. Limary, R.; Green, P. F. *Macromolecules* **1999,** 32, (24), 8167.

117. Limary, R.; Green, P. F. *Physical Review E* **2002,** 66, (2), -.

118. Limary, R.; Green, P. F.; Shull, K. R. *European Physical Journal E* **2002,** 8, (2), 103.

119. Limary, R.; P.F.Green. *Langmuir* **1999,** 15, 5617.

120. Lin, M. Y.; Lindsay, H. M.; Weitz, D. A.; Ball, R. C.; Klein, R.; Meakin, P. *Physical Review A* **1990,** 41, (4), 2005-2020.

121. Lin, X. M.; Jaeger, H. M.; Sorensen, C. M.; Klabunde, K. J. *Journal of Physical Chemistry B* **2001,** 105, (17), 3353-3357.

122. Lin, Y.; Boker, A.; He, J. B.; Sill, K.; Xiang, H. Q.; Abetz, C.; Li, X. F.; Wang, J.; Emrick, T.; Long, S.; Wang, Q.; Balazs, A.; Russell, T. P. *Nature* **2005,** 434, (7029), 55-59.

123. Liu, H.; Yates, M. Z. *Langmuir* **2002,** 18, 6066.

124. Liu, J. Y. *Journal of Electron Microscopy* **2005,** 54, (3), 251-278.

125. Lo, A.; Skodje, R. T. *Journal of Chemical Physics* **2000,** 112, (4), 1966-1974.

126. Mackay, M. E.; Dao, T. T.; Tuteja, A.; Ho, D. L.; Van Horn, B.; Kim, H. C.; Hawker, C. J. *Nature Materials* **2003,** 2, (11), 762-766.

127. Madras, G.; McCoy, B. J. *Journal of Colloid and Interface Science* **2003,** 261, (2), 423-433.

128. Madras, G.; McCoy, B. J. *Journal of Chemical Physics* **2002,** 117, (17), 8042-8049.

129. Madras, G.; McCoy, B. J. *Journal of Chemical Physics* **2003,** 119, (3), 1683-1693.

130. Madras, G.; McCoy, B. J. *Acta Materialia* **2003,** 51, (7), 2031-2040.

131. Madras, G.; McCoy, B. J. *Chemical Engineering Science* **2002,** 57, (18), 3809-3818.

132. Martula, D. S.; Hasegawa, T.; Lloyd, D. R.; Bonnecaze, R. T. *Journal of Colloid and Interface Science* **2000,** 232, (2), 241-253.

133. Masson, J. L.; Olufokunbi, O.; Green, P. F. *Macromolecules* **2002,** 35, (18), 6992.

134. Meakin, P. *Physica A* **1990,** 165, (1), 1-18.

135. Meli, L.; Pham, J. Q.; Johnston, K. P.; Green, P. F. *Physical Review E* **2004,** 69, 051601-1 - 051601-8.

136. Meredith, J. C.; K.P.Johnston. *Langmuir* **1999,** 15, 8037.

137. Michels, A.; J.Hamers. *Physica* **1937,** IV, (10), 995.

138. Midgley, P. A.; Weyland, M. *Ultramicroscopy* **2003,** 96, (3-4), 413-431.

139. Milner, S. T. *Europhysics Letters* **1988,** 7, (8), 695-699.

140. Milner, S. T.; Witten, T. A.; Cates, M. E. *Macromolecules* **1988,** 21, (8), 2610-2619.

141. Mukherjee, D.; Sonwane, C. G.; Zachariah, M. R. *Journal of Chemical Physics* **2003,** 119, (6), 3391-3404.

142. Muller-Buschbaum, P.; Vanhoorne, P.; Scheumann, V.; M.Stamm. *Europhys.Lett* **1997,** 40, 665.

143. Namatsu, H. *Journal of Vacuum Science and Technology B* **2001,** 19, (6), 2709.

144. Newkome, G. R.; Mishra, A.; Moorefield, C. N. *Abstracts of Papers of the American Chemical Society* **2001,** 221, U358-U358.

145. Ninham, B. W.; Parsegian, V. A.; Weiss, G. *Journal of Statistical Physics.* **1970,** 2, 323.

146. Nir, S. *Progress in Surface Science* **1976,** 8, (1), 1-58.

147. Nir, S. *Progress in Surface Science* **1976,** 8, (1), 1.

148. Novick, B. J.; Carbonell, R. G.; DeSimone, J. M. *Polymeric Material Science and Engineering* **2001,** 84, 51.

149. Odriozola, G.; Schmitt, A.; Callejas-Fernandez, J.; Martinez-Garcia, R.; Leone, R.; Hidalgo-Alvarez, R. *Journal of Physical Chemistry B* **2003,** 107, (10), 2180-2188.

150. Odriozola, G.; Schmitt, A.; Moncho-Jorda, A.; Callejas-Fernandez, J.; Martinez-Garcia, R.; Leone, R.; Hidalgo-Alvarez, R. *Physical Review E* **2002,** 65, (3), -.

151. Oskam, G.; Hu, Z. S.; Penn, R. L.; Pesika, N.; Searson, P. C. *Physical Review E* **2002,** 66, (1), -.

152. Otake, K.; Kobayashi, M.; Ozaki, Y.; Yoda, S.; Takebayashi, Y.; Sugeta, T.; Nakazawa, N.; Sakai, H.; Abe, M. *Langmuir* **2004,** 20, (15), 6182-6186.

153. Ouyang, J. Y.; Chu, C. W.; Szmanda, C. R.; Ma, L. P.; Yang, Y. *Nature Materials* **2004,** 3, (12), 918-922.

154. Pai, R. A.; Humayun, R.; Schulberg, M. T.; Sengupta, A.; Sun, J. N.; Watkins, J. J. *Science* **2004,** 303, (5657), 507-510.

155. Papakonstantopoulos, G. J.; Yoshimoto, K.; Doxastakis, M.; Nealey, P. F.; de Pablo, J. J. *Physical Review E* **2005,** 72, (3), -.

156. Park, S. M.; Yun, S. H.; Sohn, B. H. *Macromolecular Chemistry and Physics* **2002,** 203, (14), 2069-2074.

157. Pham, J.; Green, P. F. *To be published.*

158. Pham, J. Q.; Green, P. F. *Macromolecules* **2003,** 36, (5), 1665.

159. Pham, J. Q.; Green, P. F. *Journal of Chemical Physics* **2002,** 116, 5801.

160. Pham, J. Q.; Johnston, K. P.; Green, P. F. *Journal of Physical Chemistry B* **2004,** 108, (11), 3457-3461.

161. Pham, J. Q.; Sirard, S. M.; Johnston, K. P.; Green, P. F. *Physical Review Letters* **2003,** 91, 175503/1.

162. Pham, J. Q.; Sirard, S. M.; Johnston, K. P.; Green, P. F. *Physical Review Letters* **2003,** 91, (17), -.

163. Pich, J.; Friedlander, S. K.; Lai, F. S. *Aerosol Science* **1970,** 1, 115-126.

164. Pileni, M. P. *Journal of Physical Chemistry B* **2001,** 105, (17), 3358-3371.

165. Pohl, K.; Bartelt, M. C.; de la Figuera, J.; Bartelt, N. C.; Hrbek, J.; Hwang, R. Q. *Nature* **1999,** 397, (6716), 238-241.

166. Potschke, P.; Dudkin, S. M.; Alig, I. *Polymer* **2003,** 44, (17), 5023-5030.

167. Prasher, R.; Phelan, P. E.; Bhattacharya, P. *Nano Letters* **2006,** 6, (7), 1529-1534.

168. Pratsinis, S. E. *Journal of Colloid and Interface Science* **1988,** 124, (2), 416-427.

169. Pryamitsyn, V.; Ganesan, V. *Macromolecules* **2006,** 39, (24), 8499-8510.

170. RamachandraRao, V. S.; Watkins, J. J. *Macromolecules* **2000,** 33, (14), 5143-5152.

171. RamachandraRao, V. S.; Watkins, J. J. *Macromolecules* **2000,** 33, 5143.

172. Ratke, L.; Voorhees, P. W., *Growth and Coarsening: Ripeningin Material Processing*. Springer: Berlin, 2002.

173. Raudino, A.; Celso, F. L.; Triolo, A.; Triolo, R. *Journal of Chemical Physics* **2004,** 120, (7), 3489-3498.

174. Reiter, G. *Physical Review Letters* **1992,** 81, 75.

175. Reiter, G. *Physical Review Letters* **1991,** 68, (1), 75.

176. Reiter, G.; Sharma, A.; Casoli, A.; David, M. O.; Khanna, R.; Auroy, P. *Langmuir* **1999,** 15, 2551.

177. Reiter, G.; Sharma, A.; Casoli, A.; David, M.-O.; Khanna, R.; Auroy, P. *Europhys.Lett* **1999,** 46, (4), 512.

178. Rohrer, G. S. *Annual Review of Materials Research* **2005,** 35, 99-126.

179. Romero-Cano, M. S.; Puertas, A. M.; de las Nieves, F. J. *Journal of Chemical Physics* **2000,** 112, (19), 8654-8659.

180. Royer, J. R.; DeSimone, J. M.; Khan, S. A. *Journal of Polymer Science Part B-Polymer Physics* **2001,** 39, (23), 3055-3066.

181. Royer, J. R.; Gay, Y. J.; Desimone, J. M.; Khan, S. A. *Journal of Polymer Science Part B-Polymer Physics* **2000,** 38, (23), 3168-3180.

182. Runkana, V.; Somasundaran, P.; Kapur, P. C. *Aiche Journal* **2005,** 51, (4), 1233-1245.

183. Sabisky, E. S.; Anderson, C. H. *Physical Review Letters: A* **1973,** 7, (2), 790.

184. Sandkuhler, P.; Sefcik, J.; Lattuada, M.; Wu, H.; Morbidelli, M. *Aiche Journal* **2003,** 49, (6), 1542-1555.

185. Saunders, A. E.; Sigman, M. B.; Korgel, B. A. *Journal of Physical Chemistry B* **2004,** 108, (1), 193-199.

186. Schmaltz, B.; Brinkmann, M.; Mathis, C. *Macromolecules* **2004,** 37, 9056-9063.

187. Schmidt, G.; Malwitz, M. M. *Current Opinion in Colloid & Interface Science* **2003,** 8, (1), 103-108.

188. Schultz, A. J.; Hall, C. K.; Genzer, J. *Macromolecules* **2005,** 38, (7), 3007-3016.

189. Seeman, R.; Herminghaus, S.; Jacobs, K. *Physical Review Letters* **2001,** 86, (24), 5534.

190. Seeman, R.; Herminghaus, S.; Jacobs, K. *Journal of Physics: Condensed Matter* **2001,** 13, 4925.

191. Segalman, R.; Green, P. F. *Macromolecules* **1999,** 32, (3), 801.

192. Semin, D. J.; Lo, A.; Roark, S. E.; Skodje, R. T.; Rowlen, K. L. *Journal of Chemical Physics* **1996,** 105, (13), 5542-5551.

193. Shah, M.; Pryamitsyn, V.; Ganesan, V. *Journal of Physical Chemistry B* **2007,** 111, (2), 402-407.

194. Shah, P. S.; Husain, S.; Johnston, K. P.; Korgel, B. A. *Journal of Physical Chemistry B* **2001,** 105, (39), 9433-9440.

195. Shah, P. S.; Husain, S.; Johnston, K. P.; Korgel, B. A. *Journal of Physical Chemistry B* **2002,** 106, (47), 12178-12185.

196. Shah, P. S.; Novick, B. J.; Hwang, H. S.; Lim, K. T.; Carbonell, R. G.; Johnston, K. P.; Korgel, B. A. *Nano Letters* **2003,** 3, (12), 1671-1675.

197. Sharma, A. *Langmuir* **1998,** 14, 4915.

198. Sharma, A. *Langmuir* **1993,** 9, 3580.

199. Sharma, A. *Langmuir* **1993,** 9, 861.

200. Sharma, A.; Reiter, G. *Journal of Colloid and Interface Science* **1996,** 178, 383.

201. Sholl, D. S.; Skodje, R. T. *Physica A* **1996,** 231, (4), 631-647.

202. Shorlin, K.; Krylov, S.; Zinke-Allmang, M. *Physica A* **1998,** 261, 248-265.

203. Shull, K. R. *Macromolecules* **1996,** 29, (7), 2659-2666.

204. Shull, K. R. *Macromolecules* **1993,** 26, (9), 2346-2360.

205. Shull, K. R.; Winey, K. I.; Thomas, E. L.; Kramer, E. J. *Macromolecules* **1991,** 24, (10), 2748-2751.

206. Siggia, E. D. *Physical Review A* **1979,** 20, (2), 595-605.

207. Sirard, S. M.; Green, P. F.; Johnston, K. P. *Journal of Physical Chemistry B* **2001,** 105, (4), 766-772.

208. Sirard, S. M.; Gupta, R. R.; Russell, T. P.; Watkins, J. J.; Green, P. F.; Johnston, K. P. *Macromolecules* **2003,** 36, (9), 3365-3373.

209. Sirard, S. M.; Ziegler, K. J.; Sanchez, I. C.; Green, P. F.; Johnston, K. P. *Macromolecules* **2002,** 35, (5), 1928-1935.

210. Smitham, J. B.; Napper, D. H. *Journal of Colloid and Interface Science* **1976,** 54, (3), 467-470.

211. Smitham, J. B.; Napper, D. H. *Journal of the Chemical Society-Faraday Transactions I* **1976,** 72, 2425-2428.

212. Sohn, B. H.; Seo, B. H. *Chemistry of Materials* **2001,** 13, 1752-1757.

213. Sohn, B. H.; Yoo, S. I.; Seo, B. W.; Yun, S. H.; Park, S. M. *Journal of the American Chemical Society* **2001,** 123, 12734-12735.

214. Stafford, C. M.; T.P. Russell; McCarthy, T. J. *Macromolecules* **1999,** 32, 7610.

215. Starr, F. W.; Schroder, T. B.; Glotzer, S. C. *Physical Review E* **2001,** 6402, (2), -.

216. Starr, F. W.; Schroder, T. B.; Glotzer, S. C. *Macromolecules* **2002,** 35, (11), 4481-4492.

217. Stechemesser, H.; Dobias, B., *Coagulation and Floculation*. 2nd ed.; CRC: Boca Raton, 2005; Vol. 126.

218. Sternstein, S. S.; Zhu, A. J. *Macromolecules* **2002,** 35, (19), 7262-7273.

219. Striolo, A.; Egorov, S. A. *Journal of Chemical Physics* **2007,** 126, (1), -.

220. Tang, J.; Ge, G. L.; Brus, L. E. *Journal of Physical Chemistry B* **2002,** 106, (22), 5653-5658.

221. Tessler, N.; Medvedev, V.; Kazes, M.; Kan, S.; Bani, U. *Science* **2002,** 295, 5559.

222. Thompson, R. B.; Ginzburg, V. V.; Matsen, M. W.; Balazs, A. C. *Science* **2001,** 292, (5526), 2469-2472.

223. Tripp, C. P.; Combes, J. R. *Langmuir* **1998,** 14, 7348.

224. Usuki, A.; Hasegawa, N.; Kato, M. *Inorganic Polymeric Nanocomposites and Membranes* **2005,** 179, 135-195.

225. Vacatello, M. *Macromolecules* **2001,** 34, (6), 1946-1952.

226. Valignat, M. P.; Bardon, S.; Villete, S.; Cazabat, A. M. *Fluid Phase Equilibria* **1998,** 150-151, 615.

227. Van Hyning, D. L.; Klemperer, W. G.; Zukoski, C. F. *Langmuir* **2001,** 17, (11), 3128-3135.

228. Villarica, M.; Casey, M. J.; Goodisman, J.; Chaiken, J. *Journal of Chemical Physics* **1993,** 98, (6), 4610-4625.

229. Vincent, B.; Edwards, J.; Emmett, S.; Jones, A. *Colloids and Surfaces* **1986,** 18, (2-4), 261-281.

230. Vincent, B.; Luckham, P. F.; Waite, F. A. *Journal of Colloid and Interface Science* **1980,** 73, (2), 508-521.

231. Visser, J. *Advances in Colloid and Interface Science* **1972,** 3, 331.

232. Vitt, E.; Shull, K. R. *Macromolecules* **1995,** 28, 6349.

233. Vogt, B. D.; Brown, G. D.; RamachandraRao, V. S.; Watkins, J. J. *Macromolecules* **1999,** 32, 7907.

234. Von Smoluchowski, M. *Zeitschrift fur Physik* **1916,** 17, 585.

235. Wagner, C. *Zeitschrift fuer Elektrochemie und Angewandte Physikalische Chemie* **1961,** 65, 581-591.

236. Wang, Q.; Nealey, P. F.; de Pablo, J. J. *Journal of Chemical Physics* **2003,** 118, (24), 11278-11285.

237. Weibel, G. L.; Ober, C. K. *Microelectronic Engineering* **2003,** 65, 145.

238. Wijmans, C. M.; Leermakers, F. A. M.; Fleer, G. J. *Langmuir* **1994,** 10, (5), 1331-1333.

239. Wijmans, C. M.; Zhulina, E. B.; Fleer, G. J. *Macromolecules* **1994,** 27, (12), 3238-3248.

240. Wissinger, R. G.; M.E.Paulaitis. *Journal Of Polymer Science: Part B: Polymer Physics* **1987,** 25, 2497.

241. Wissinger, R. G.; Paulaitis, M. E. *Journal of Polymer Science: Part B: Polymer Physics* **1991,** 29, (5), 631-633.

242. Witten, T. A.; Pincus, P. A. *Macromolecules* **1986,** 19, (10), 2509-2513.

243. Xie, R.; Karim, A.; Douglas, J. F.; Han, C. C.; Weiss, R. A. *Physical Review Letters* **1998,** 81, (6), 1251.

244. Yeh, S. w.; Wei, K. H.; Sun, Y. S.; Jeng, U. S.; Liang, K. S. *Macromolecules* **2005,** 38, 6559-6565.

245. Yezek, L.; Schartl, W.; Chen, Y. M.; Gohr, K.; Schmidt, M. *Macromolecules* **2003,** 36, (11), 4226-4235.

246. Zamborini, F. P.; Leopold, M. C.; Hicks, J. F.; Kulesza, P. J.; Malik, M. A.; Murray, R. W. *Journal of the American Chemical Society* **2002,** 124, (30), 8958-8964.

247. Zhang, H. Z.; Banfield, J. F. *Nano Letters* **2004,** 4, (4), 713-718.

248. Zhang, L. F.; Eisenberg, A. *Journal of the American Chemical Society* **1996,** 118, (13), 3168-3181.

249. Zhang, Q.; Archer, L. A. *Macromolecules* **2004,** 37, (5), 1928-1936.

250. Zhang, X.; Pham, J. Q.; Martinez, H. J.; Wolf, J.; P.F.Green; K.P.Johnston. *Journal of Vacuum Science and Technology B* **Submitted 2003**.

251. Zhulina, E. B.; Borisov, O. V.; Brombacher, L. *Macromolecules* **1991,** 24, (16), 4679-4690.

252. Zinke-Allmang, M. *Thin Solid Films* **1999,** 346, (1-2), 1-68.

Vita

Luciana Meli was born on May 26th, 1977 in Mexico City, Mexico, the daughter of Roberto Meli Piralla and Guillermina Thompson Palomino. Upon graduating from Alexander Bain High School, she was admitted in the Chemical Engineering Department at Universidad Nacional Autónoma de México, where she graduated with top honors. In Fall of the year 2001 she began her graduate studies in the Chemical Engineering Department of the University of Texas at Austin.

Permanent address: 197 Serrania St., Mexico City, D.F. 04500
This dissertation was typed by the author.